Monitoring defect-induced perturbations of the ideal crystal structure of ZnO and Cu$_2$O by Raman spectroscopy

DISSERTATION

zur Erlangung des Doktorgrades
der Naturwissenschaften
(Dr. rer. nat.)

vorgelegt von

THOMAS SANDER

betreut von

Prof. Dr. Peter J. Klar
I. Physikalisches Institut
Justus-Liebig-Universität Gießen

JUSTUS-LIEBIG-
UNIVERSITÄT
GIESSEN

– anno 2015 –

Zusammenfassung

Diese Dissertation widmet sich experimentellen Untersuchungen der Gitterdynamik in den oxidischen Halbleitern Kupfer(I)-oxid (Cu_2O) und Zinkoxid (ZnO) mittels der Raman-Spektroskopie. Insbesondere wird der Einfluss von strukturellen Defekten auf die phononische Struktur idealer Kristalle und der Einfluss von Dotierung am Beispiel von Stickstoff dotiertem Zinkoxid (ZnO:N) vorgestellt.

Der Raman-Effekt bezeichnet die inelastische Streuung an quantisierten Eigenzuständen der Gitterschwingungen (Phononen) mit elektromagnetischer Strahlung [1, 2]. Dabei bestimmen Impuls- und Energieerhaltung sowie Symmetrie-Auswahlregeln, welche Gitterschwingung im Experiment detektiert werden kann. Defekte brechen die perfekte Translationssymmetrie des Kristallgitters und weichen somit die Erhaltungssätze und Auswahlregeln auf. Dadurch kann sowohl die Streuung an Phononen an einem beliebigen Punkt der Brillouin-Zone als auch die Streuung an Raman- und Symmetrie-verbotenen Moden zu experimentellen Signalen beitragen [3, 4]. Außerdem können Defekte zu lokalen Schwingungen angeregt werden, die zusätzliche Signale in Raman-Spektren verursachen können [5].

Als erstes Beispiel für ideale Systeme werden Raman-Messungen an kristallinen ZnO Proben vorgestellt. Die Beobachtungen können mit Hilfe der Auswahlregeln für einen idealen Kristall beschrieben werden, obwohl die vorliegenden Proben, wie alle Materialien nicht frei von Defekten sind, da die Entropie immer zur Bildung von Gitterdefekten führt [6]. So ist zum Beispiel bekannt, dass nominell undotiertes ZnO auf Grund von intrinsischen Defekten und extrinsischen Verunreinigungen n-leitend ist [7–10]. Die Raman-Spektroskopie ist also typischen Konzentrationen solcher Defekte in den untersuchten Proben gegenüber unempfindlich.

Anders stellt sich die Situation für die Dotierung von ZnO mit Stickstoff dar. Hier treten schon ab einer Defektkonzentration von ungefähr 10^{18} N Atomen/cm^3 fünf zusätzliche Signale in den Raman-Spektren auf [11]. Dieses Ergebnis ist unabhängig von der verwendeten Wachstumsmethode der Proben. Die Ursache für das Auftreten dieser Moden wurde in den letzten Jahren kontrovers diskutiert [11–19]. In dieser Arbeit werden sowohl die Raman-aktiven ZnO Gitterschwingungen und die dem Stickstoff zugeordneten Moden systematisch in Abhängigkeit der N-Konzentration analysiert. Neben der Polarisationsabhängigkeit, d.h. der Orientierung der Kristallstruktur relativ zur Polarisation des anregenden Lasers, wird auch das Verhalten unter hydrostatischem Druck untersucht. Die experimentellen Beobachtungen gehen über die bisherigen Stu-

dien hinaus und können nicht schlüssig von den bisher diskutierten Modellen wiedergegeben werden. Stattdessen liefern sie Hinweise, dass die zusätzlichen Raman-Moden von Einschlüssen, aufgebaut aus N-Atomen, verursacht werden. Basierend auf diesen Ergebnissen wird ein Modell für Zn_3N_2 Einschlüsse vorgestellt, die sich bilden könnten, sobald die Löslichkeitsgrenze von N-Atomen auf Sauerstoff-Gitterplätzen überschritten wird.

Der letzte Abschnitt dieser Arbeit behandelt die Gitterdynamik von Cu_2O. Raman-Spektren von kristallinen Cu_2O Proben zeigen eine ausgeprägte Struktur [4]. Sie werden typischerweise von infrarot-aktiven und stillen Moden dominiert, obwohl nur eine Raman-aktive Mode für ein ideales kubisches Kristallgitter erwartet wird. Die Auswahlregeln für Raman-Streuung eines perfekten Kristalls sind in diesem Fall nicht gültig. Es wird gezeigt, dass intrinsische Defekte die Symmetrie des idealen Kristallgitters erniedrigen und dadurch die Raman-Aktivitäts- und Symmetrie-Auswahlregeln modifiziert werden. Kupfer-Fehlstellen, bei denen das benachbarte Kupferatom auf einen Zwischengitterplatz verschoben ist, führen sogar dazu, dass alle Raman-verbotenen Moden Raman-aktiv werden. Die Erniedrigung der Kristallsymmetrie durch diesen besonderen Defekt ist also eine mögliche Erklärung für die ungewöhnlichen Raman-Spektren. Theoretische Berechnungen für die von diesem Defekt verursachte Störung des Kristallgitters untermauern dieses Model. Als alternative Ursache für die Aufhebung der Auswahlregeln wird der Einfluss von resonanten Raman-Streumechanismen und der Aufhebung des Wellenzahlerhaltungsatzes diskutiert.

Contents

Introduction

Deviations from an ideal crystal structure, like point and line defects or complexes, play an important role in semiconductor physics. The intentional use of defects is a tool to tune the building blocks of modern electronics. Various material properties are determined by defects depending on the type, their arrangement, and their concentration. For example, selective doping with impurities may give rise to electronic states in the band gap defining the type of majority carriers, electrical conductivity, free-carrier concentration and mobility as well as optical absorption and emission, among others [20–24]. These characteristics need to be customized for the development of electronic and optoelectronic device applications like n- and p-type layers for light-emitting diodes (LEDs). This example shows that the study of defects and their characteristics is necessary as well as that defects make semiconductor physics interesting.

In general, defects in semiconductors, especially dopants, are investigated by Hall effect experiments, deep-level transient spectroscopy (DLTS), and optical methods such as absorption or luminescence spectroscopy (e.g., see references 22, 25, and 26). In addition, a variety of microscopy and particle beam methods are employed to characterize deviations from an ideal crystal structure. Raman spectroscopy is commonly used to analyze only the chemical composition of the material under study and not defects. However, Raman spectroscopy may also give insight into defects in semiconductors, as demonstrated within the framework of this thesis.

Defects may modify the dynamics of a crystalline lattice which affects material characteristics like the specific heat, thermal expansion, or thermal conductivity. The Raman effect is an inelastic scattering process making the study of phonons, quanta of lattice vibrations, at the center of the Brillouin zone possible and revealing the chemical composition, crystal class, and orientation among other properties of the material under study. The lattice vibrations detectable by vibrational spectroscopy are restricted by the laws of energy and momentum conservation as well as by symmetry selection-rules. Non-stoichiometry due to the formation of defects may lift these restrictions in crystalline materials: on the one hand, the perfect translational symmetry is broken leading to the relaxation of the wave-vector-conservation selection-rule [3, 27]. Consequently, phonon states with momenta out of the whole Brillouin zone will contribute to the Raman signals, which may result in shifts in vibrational frequency, line broadening, and line shape variations in the Raman spectra. Furthermore, the Raman activity and symmetry selection-rules no longer hold strictly, e.g., defects reduce the local symmetry such that the assignment to Raman-active or

Raman-forbidden lattice vibrations may be modified [4, 28]. On the other hand, depending on the type of defect, its compatibility with the lattice, and the resulting scattering probability, additional modes may be introduced, such as local impurity vibrations or a series of modes arising from complex structures [5, 29]. Chapter 1.3 of this thesis focuses on the impact of defects on Raman scattering and how in turn Raman spectra can be used to gain insight into defects in semiconductors. The theoretical discussion raises the questions when which effect will occur and when its perturbation is large a enough to be detectable in experimental Raman spectra.

The oxide semiconductors cuprous oxide (Cu_2O) and zinc oxide (ZnO) as well as nitrogen doped zinc oxide (ZnO:N) are typical examples of materials whose properties are controlled by defects providing a huge variety of interesting physics. Nominally undoped ZnO is often intrinsically n-type conducting due to intrinsic defects and/or, more likely, due to the incorporation of extrinsic impurities during the growth process such as hydrogen [7–10]. In chapter 3, the lattice dynamics of ZnO are investigated, in particular the correlation between its crystal structure, phonon symmetry characters, and scattered Raman intensities. All experimental findings using Raman spectroscopy are consistent with the laws of conservation as well as the Raman activity and the symmetry selection-rules established for an ideal crystal structure. Essentially, the Raman spectra of nominally undoped ZnO samples analyzed do not exhibit any impact of defects. In general, this holds true for most crystalline materials.

Nitrogen was naturally believed to be the best candidate for a shallow acceptor dopant in ZnO since it possesses a similar ionic radius as oxygen and since it was successfully used to p-type dope ZnS and ZnSe [30–32]. Nevertheless, none of the approaches using nitrogen achieved stable, reproducible, and homogenous p-type conductivity yet, overcoming the doping asymmetry in ZnO. In chapter 4, the appearance of additional Raman modes related to the nitrogen impurity in ZnO are addressed. The unusually high number of five defect-related modes appears independent of the growth technique. The defect-related modes scale in intensity with the N content while at the same time the ZnO host phonons remain unaltered. The characteristics of the nitrogen-related modes are analyzed indicating that these modes might originate either from Raman-forbidden ZnO phonons or from clusters containing N atoms/ions embedded in ZnO. Chapter 4 closes with a discussion of the possible formation of Zn_3N_2-like clusters or nanoinclusions as a likely cause of nitrogen-related modes, and their relevance for doping, since such inclusions would limit the solubility of nitrogen in ZnO.

Currently, the copper-oxygen compound system, consisting of the phases CuO, Cu_2O, and Cu_4O_3, is receiving renewed interest for solar-cell applications due to the suitability of its band gaps for achieving high efficiencies as well as consisting of sustainable elements [33]. Cuprous oxide is a natural p-type semiconductor, whose conductivity is controlled by the cation deficiency (non-stoichiometry), i.e., by intrinsic point defects like oxygen interstitials or copper vacancies [34].

In chapter 5, the lattice dynamics of Cu_2O are investigated, in particular its unusual Raman spectra. The dominant signals observed in Raman spectra of Cu_2O are actually due to infrared active, silent, and defect modes rather than due to the single Raman-active mode, independent of the method and conditions of the synthesis. These findings are in contrast to the Raman spectra of pure ZnO. In general, perturbations by point defects are insignificant when studying crystalline materials by Raman spectroscopy; however, it will be demonstrated by a group theoretical analysis that the copper vacancy in the so-called split configuration introduces an unusually strong perturbation leading to Raman activity of all Cu_2O extended phonon modes observed in experiment. Resonant Raman scattering mechanisms or the relaxation of the wave-vector-conservation selection-rule may also account for the observation of normally Raman-forbidden phonons, but only the changes introduced by defect-induced Raman activity seem to be consistent with the symmetry characteristics of the phonons observed in experiment.

This thesis is structured as follows: the first two chapters serve as brief introductions to lattice dynamics of crystals, classifications of phonons, inelastic light scattering, and the impacts of defects on Raman scattering. Chapter 2 provides information about the experimental setup used. In the next three chapters, the experimental results are presented as indicated above. At the end, the findings are summarized and an outlook for further research is given.

The results presented in this thesis, in particular in chapters 3 and 5, have been previously published and may be found in references 33, 35, 36, 37, and 38.

1 Theoretical background – Correlations between crystal symmetries, lattice vibrations, defects, and Raman spectroscopy

All semiconductor materials reveal unique Raman spectra due to the chemical elements of which they are composed. Nevertheless, different Raman spectra of one kind of material might deviate from each other depending on the phase the semiconductor crystallizes in, the crystal quality, and the orientation of the semiconductor's crystal axes with respect to the propagation directions of the incident and scattered radiation as well as the orientations of the corresponding polarization vectors in experiment. For instance, one may observe different Raman signals when analyzing the scattered radiation parallel or perpendicular to the propagation direction of the incident radiation. The crystal structure of the semiconductor and its symmetry characteristics are the physical origin of the diversity in experimental spectra and dependences on orientation. An analysis by means of group theoretical methods only based on the crystal lattice structure of the material already yields, in principle, the properties of the lattice dynamics of the crystal and allows one to determine which lattice vibrations couple to incident electromagnetic radiation via inelastic light scattering. The following chapter briefly describes why and how lattice vibrations are classified by irreducible representations of the crystallographic point groups giving their symmetry characteristics. The Raman effect will be introduced within a semiclassical approach and use will be made of the symmetry characteristics of the lattice vibrations to determine selection rules for their Raman activity in an ideal crystal structure. The last part of this chapter focuses on perturbations of the lattice dynamics caused by defects. In particular, localized vibrational modes of defects will be addressed, as well as the lifting or breaking of the selection rules due to lowering of the symmetry will be discussed using group theoretical arguments. The concepts summarized in this introductory chapter can be found in more detail in references 2, 5, 24, 28, 39 to 44.

1.1 Lattice dynamics and classification of vibrations

The study of the dynamics of a perfect crystalline lattice based on the many particle Hamiltonian consisting of the kinetic energies of all (valence) electrons

and ions (nuclei and core electrons) as well as the Coulomb interaction between them, neglecting relativistic corrections, is still a formidable task due to the large number of particles involved. The Hamiltonian $\mathcal{H}$ is simplified considerably by applying the Born-Oppenheimer or adiabatic approximation which separates the electronic and ionic motions from each other. Furthermore, the harmonic approximation is used for describing the interactions between the ions. As a result one obtains the following Hamiltonian for the ions [24]:

$$
\mathcal{H} = \mathcal{T} + U^{\mathrm{harm}} = \frac{1}{2} \sum_{i=1}^{3} \sum_{k=1}^{N} m_k \left(\frac{\partial u_{k,i}}{\partial t} \right)^2 + \frac{1}{2} \sum_{i,j=1}^{3} \sum_{k,l=1}^{N} \frac{\partial^2 V}{\partial u_{k,i} \partial u_{l,j}} u_{k,i} u_{l,j}
$$

$$(1.1)$$

Here m_k denotes the mass of the kth ion, $u_{k,i}$ denotes its displacement coordinate from the equilibrium position, N is the total number of atoms in the crystal, and V is the adiabatic electronic potential. Treating $\mathcal{H}$ classically and making use of the periodicity of the crystal lattice results in a system of $3n$ linear homogeneous equations, where n is the number of atoms in the primitive unit cell, describing a system of coupled harmonic oscillators. The solution of the characteristic equation of this system yields $3n$ eigenfrequencies $\omega_\lambda(\vec{q})$ for each wave vector $\vec{q}$. The functions $\omega_\lambda(\vec{q})$ are the $3n$ phonon branches of the phonon dispersion relation.

The Hamiltonian given in equation (1.1) is invariant under symmetry operations of the particular space group of the crystal. By a proper orthogonal transformation $\mathcal{H}$ can be represented in normal coordinates Q_k with frequencies ω_k [2]:

$$
\mathcal{H} = \frac{1}{2} \sum_{k=1}^{3N} \left[\left(\frac{\partial Q_k}{\partial t} \right)^2 + \omega_k^2 Q_k^2 \right]
$$

$$(1.2)$$

Due to the symmetry invariance, the normal coordinates form a basis for a $3N$ dimensional representation, which in general can be decomposed into irreducible representations of the point group of the crystal. Hence, lattice vibrations can be classified according to irreducible representations of one of the 32 crystallographic point groups to which the particular space group of the crystal belongs. In a similar manner, vibrations and rotations of molecules are classified. The representations are denoted by Mulliken symbols listed in table 1.1, which represent their symmetry characteristics [43, 45, 46]. Therefore, vibrations are assigned to a specific *symmetry species* or *symmetry type*. For instance, a vibration of A_{1g} type is totally symmetric under all symmetry operations, whereas an E_u type vibration is twofold-degenerate and antisymmetric with respect to an inversion [2]. For a given crystal structure, group theoretical techniques make it possible to determine the number of lattice vibrations, their symmetry characteristics, i.e., their symmetry type, and their degree of degeneracy [47]. This can be achieved by the factor group, molecular site group, or nuclear site group analysis method for lattice vibrations at the center of the Brillouin zone

Mulliken symbol	dimension	character χ				
		E	C_n	i	σ_h	C_2 or σ_v
A	1	1	1			
B	1	1	-1			
E	2	2				
F/T	3	3				
X_g				1		
X_u				-1		
X'					1	
X''					-1	
Y_1						1
Y_2						-1

Table 1.1: Abbreviations of irreducible representations of the crystallographic point groups and their corresponding symmetry characteristics. The Mulliken symbols are used to classify molecular and lattice vibrations. The letter X is a variable for any Mulliken symbol while Y is a variable for A or B [43, 45, 46].

(Γ-point). Knowing the symmetry type of the lattice vibrations enables one further to derive which modes couple to electromagnetic radiation. This procedure will be elucidated in the next chapter. An actual value for the adiabatic electronic potential V in equation (1.1) is only required when explicitly calculating the vibrational frequencies and amplitudes.

1.2 Raman spectroscopy

Raman spectroscopy is the analysis of light inelastically scattered by time-dependent inhomogeneities in a medium. This type of inelastically scattered radiation was discovered by the Indian physicist C. V. Raman in 1928 [48]. While Raman was studying the scattered radiation by liquids, he observed new lines in the spectra on either side of the exciting wavelength and identified the shifts in energy with the change in energy of the vibrational states of the molecules in the liquid [48–52]. For his experimental discoveries C. V. Raman received the Noble prize in physics in 1930 [53]. Already five years before Raman's experimental observation in 1923, the Austrian physicist A. Smekal analyzed the interaction of radiation with matter quantum mechanically [54]. He indicated the possibility of a change in energy of electromagnetic radiation by an amount equal to the difference between two states of the system. Thus, not only the change in energy of electromagnetic radiation inelastically scattered by molecular vibrations is refered to as the Raman effect but also scattering by quasi-particles, such as phonons, plasmons, and polaritons, or single particle excitations, like vibrational or electronic excitations of impurities in solids. An important semiclassical description of the Raman effect was developed by the

Czech physicist G. Placzek in 1934, known as the polarizability theory [55]. It allows one to derive selection rules for the Raman effect from the symmetry of the polarizability and accordingly of the susceptibility by applying group theoretical methods [48].

The polarizability theory

In the macroscopic framework of the polarizability theory, elementary excitations may induce a change in the in the polarizability $\boldsymbol{\alpha}$ of molecules or the electric susceptibility $\boldsymbol{\chi}$ of crystals which is the origin of Raman scattering [2]. An incident electric field present in a medium

$$\vec{E}(\vec{r}, t) = \vec{E}_{\mathrm{i}}(\vec{k}_{\mathrm{i}}, \omega_{\mathrm{i}}) \cos(\vec{k}_{\mathrm{i}}\vec{r} - \omega_{\mathrm{i}}t) \tag{1.3}$$

will induce a dipole moment in a molecule or a polarization $\vec{P}$ in a crystal:

$$\vec{P}(\vec{r}, t) = \epsilon_0 \int \boldsymbol{\chi}(\vec{r}, \vec{r}', t, t') \vec{E}(\vec{r}', t') \mathrm{d}\vec{r}' \mathrm{d}t' , \tag{1.4}$$

where ϵ_0 is the vacuum permittivity and $\vec{E}_{\mathrm{i}}$ is the amplitude of the incident electric field of frequency ω_{i} and wave vector $\vec{k}_{\mathrm{i}}$. In case of a vibrational excitation of the crystal lattice, for instance, the susceptibility will be modulated. Under the assumption that the exciting radiation is far away from singularities in the electronic susceptibility $\boldsymbol{\chi}$, the modulation can be treated as a perturbation and the susceptibility can be expanded in a Taylor series in normal coordinates Q_k of the excitation around the equilibrium positions:

$$\boldsymbol{\chi}(\vec{k}_{\mathrm{i}}, \omega_{\mathrm{i}}, Q_k) = \boldsymbol{\chi}_0 + \sum_k \left(\frac{\partial \boldsymbol{\chi}}{\partial Q_k}\right)_0 Q_k + \sum_{k,m} \left(\frac{\partial^2 \boldsymbol{\chi}}{\partial Q_k \partial Q_m}\right)_0 Q_k Q_m + \ldots \tag{1.5}$$

with

$$Q_k(\vec{r}, t) = Q_{k0}(\vec{q}, \omega_k) \cos(\vec{q}\vec{r} - \omega_k t) \tag{1.6}$$

One obtains for the polarization by substituting equations (1.5) and (1.6) into (1.4):

$$\begin{aligned} \vec{P}(\vec{r}, t, Q_k) = {} & \epsilon_0 \boldsymbol{\chi}_0 \vec{E}_{\mathrm{i}} \cos(\vec{k}_{\mathrm{i}}\vec{r} - \omega_{\mathrm{i}}t) + \\ & \frac{1}{2} \cdot \sum_k \left(\frac{\partial \boldsymbol{\chi}}{\partial Q_k}\right)_0 Q_{k0} \cdot \epsilon_0 \vec{E}_{\mathrm{i}} \cdot \big[\cos((\vec{k}_{\mathrm{i}} - \vec{q})\vec{r} - (\omega_{\mathrm{i}} - \omega_k)t) + \\ & \qquad\qquad + \cos((\vec{k}_{\mathrm{i}} + \vec{q})\vec{r} - (\omega_{\mathrm{i}} + \omega_k)t) \big] + \ldots , \end{aligned} \tag{1.7}$$

where $\vec{q}$ and ω_k are the wave vector and the frequency of the lattice vibration, respectively. The first term on the right hand side of equation (1.7) is a polarization vibrating in phase with the incident electric field. It causes elastically scattered light of frequency ω_{i}, known as Rayleigh scattering. The second and

third summand on the right hand side in the equation (1.7) are induced polarization waves by one phonon consisting of a Stokes shifted wave with frequency $\omega_S = \omega_i - \omega_k$ and wave vector $\vec{k}_S = \vec{k}_i - \vec{q}$ and an anti-Stokes shifted wave with frequency $\omega_{aS} = \omega_i + \omega_k$ and wave vector $\vec{k}_{aS} = \vec{k}_i + \vec{q}$. The equations describe one-phonon (first-order) Raman scattering and embody that energy and momentum are conserved during the inelastic scattering process. Higher-order terms in the expansion of the electric susceptibility χ in equation (1.5) give rise to scattering by more than one phonon (higher-order Raman scattering).

The maximal carry of the one-phonon wave vector is $2\vec{k}_i$ due to momentum conservation. Using light in the visible wavelength regime for excitation, this value is small compared to the size of the Brillouin zone. Thus, one-phonon Raman scattering of an ideal crystal structure only probes lattice vibrations from the center of the Brillouin zone ($\vec{q} \approx 0$). The constraint of an almost vanishing $\vec{q}$ value is referred to as the *wave-vector selection-rule* of one-phonon Raman scattering.

The scattering cross-section

Within the macroscopic framework, the spectral differential cross-section can be obtained with the help of the induced polarization in equation (1.7). For the Stokes component of first-order scattering by phonons follows [40, 42]:

$$\frac{\partial^2 \sigma_S}{\partial \Omega \partial \omega_s} = \frac{\omega_i \omega_s^3}{(4\pi)^2 c^4} \frac{n_s}{n_i} V_s V_t \cdot \left| \vec{e}_s \frac{\partial \chi}{\partial Q_k} \vec{e}_i \right|^2 \cdot (n(\omega_k) + 1) \frac{\hbar}{2N\omega_k} \cdot \Delta(\omega_i - \omega_s), \quad (1.8)$$

where ω_k is the phonon frequency, ω_i is the frequency of the incident radiation, and ω_s the frequency of the scattered light. The spectral differential cross-section further depends on the ratio of the refractive indices n_i and n_s of the medium for the incident and scattered radiation, on the scattering volume V_s, the total sample volume V_t, and on the number of primitive unit cells N of the crystal. The unit vectors $\vec{e}_i$ and $\vec{e}_s$ represent the polarization of the incident and scattered radiation, respectively, c is the speed of light, and $n(\omega_k)$ is the Bose-Einstein statistical factor. To account for the finite width of signals at frequency ω_k, equation (1.8) is weighted by the line shape function $\Delta(\omega_i - \omega_s)$, which usually exhibits a Lorentzian profile. The total Raman scattering cross-section σ_S is obtained by integrating the spectral differential cross-section over the scattered frequencies $\partial \omega_s$ and the solid angle element $\partial \Omega$. Similar cross sections can be derived for anti-Stokes and multi-phonon scattering. It follows from such considerations that first-order Raman spectra display a set of discrete lines, whereas higher-order processes give rise to a broad continuum of features.

The equations for the polarization and for the spectral differential scattering cross-section (1.7) and (1.8) demonstrate that a lattice vibration can only contribute to Raman scattering if it induces a change in the polarizability or sus-

ceptibility. In particular, the derived polarizability tensor $(\partial\boldsymbol{\chi}/\partial Q_k)_0$ must have nonvanishing components.

The Raman tensor

The derived polarizability tensor is proportional to the Raman tensor with the components $\mathcal{R}_{jl}^k = (\partial\chi_{jl}/\partial Q_k)_0$. It is a third rank tensor: the indices j and l cover the space coordinates x, y, and z, respectively. The third index k extends across the $3n - 3$ normal coordinates Q_k for the vibrations, where n is the number of atoms in the primitive unit cell. In the following, the term *Raman tensor* denotes for simplicity a second rank tensor $\boldsymbol{\mathcal{R}}^k$ of one individual mode k, in which case it has the form of a quadratic matrix with three rows and three columns. The actual elements of the matrix depend on the symmetry type of the mode, i.e., on its irreducible representation of a crystallographic point group, as well as on the orientation of the three orthogonal coordinate axes x, y, and z with respect to the crystallographic axes. For non-magnetic materials in the quasi-static approximation, i.e., if the excitation frequency is large compared to the frequency of the scattered radiation, the Raman tensor is fully symmetric [44]:

$$\mathcal{R}_{jl}^k = \mathcal{R}_{lj}^k \tag{1.9}$$

These approximations hold for the vast majority of cases. An important exception is resonant Raman scattering, where the quasi-static approximation is not valid and Raman tensors may be antisymmetric.

Whether or not a lattice vibration is Raman active, thus has nonvanishing tensor elements, can be determined on the one hand by analyzing the displacement of the atoms of that particular lattice vibration in the ideal crystal structure and by verifying if it induces a change in the susceptibility. On the other hand, one can make use of the symmetry properties of the ideal crystal structure and of the lattice vibrations introduced in chapter 1.1.

Application of group theory – Raman activity

In quantum mechanics, the transition probability for a system from an initial state described by Ψ_i to a final state described by Ψ_f is proportional to the following matrix element [2, 28, 41, 43]:

$$M_{if} = \int \Psi_f^* \hat{O} \Psi_i d\tau \,, \tag{1.10}$$

where $\hat{O}$ is the operator driving the transition. Using group theory, one can demonstrate that the matrix element in equation (1.10) may be nonzero, i.e., the transition from the initial to the final state is allowed, if the direct product of the representations of the initial state, the transition operator, and the final

state is or contains the totally symmetric representation. An equivalent formulation is that the direct product of the representations of the initial state and the transition operator is or contains the representation of the final state. In the case of Raman scattering, the driving operator of the transition is the derived polarizability tensor, which is a second rank tensor. Every tensor transforms as the product of coordinates; thus, its representation corresponds to that of the product of coordinates of the appropriate point group.[1] Assuming that the initial state belongs to the totally symmetric representation, i.e., the system is in the unexcited ground state, and that the final state is a phonon state characterized by its irreducible representation Γ_{f} of the point group of the crystal, a Raman transition is allowed if Γ_{f} belongs to the representation of the derived polarizability tensor of the corresponding crystallographic point group (at $\vec{q} \approx 0$). An equivalent formulation is that Γ_{f} must be contained at least once in the decomposition of the direct product of the polar vector representation Γ_{v} with itself [44]:

$$\Gamma_{\mathrm{v}} \otimes \Gamma_{\mathrm{v}} \supset \Gamma_{\mathrm{f}} \tag{1.11}$$

When any of the two conditions is satisfied, the phonon characterized by the irreducible representation Γ_{f} of the point group of an ideal crystal is *Raman active*, i.e., it exhibits a Raman tensor with nonvanishing components. Two-phonon processes are Raman active if the direct product $\Gamma_n \otimes \Gamma_m$ of the modes n and m contains irreducible representations that are themselves Raman active. In a similar manner, selection rules for infrared activity can be derived bearing in mind that the transition operator for an interaction with electromagnetic radiation is the dipole moment, which transforms according to the coordinates, thus, like a polar vector. The remaining lattice vibrations in an ideal crystal structure, which are neither Raman nor infrared active, do not couple to electromagnetic radiation and are called silent modes. By means of group theory, the matrix form of the Raman tensors can be constructed for all point groups and irreducible representations of lattice vibrations, tabulated for example in the book by Hayes and Loudon [40].

The scattered intensity – polarization or symmetry selection-rule

The intensity of inelastically scattered light is proportional to the square of the induced polarization and, therefore, to the square of the Raman tensor $\boldsymbol{\mathcal{R}}^k$. This yields

$$I^k \propto \left| \vec{e}_{\mathrm{s}}^{\,T} \cdot \boldsymbol{\mathcal{R}}^k \cdot \vec{e}_{\mathrm{i}} \right|^2 = \left| \sum_{j,l} e_{\mathrm{s},j} \cdot \mathcal{R}_{jl}^k \cdot e_{\mathrm{i},l} \right|^2 \tag{1.12}$$

for an individual mode k if the excitation frequency is far from than any singularities in the electronic polarizability or susceptibility [42]. The unit vectors $\vec{e}_{\mathrm{i}}$

---

[1] The transformation properties of the polarizability are demonstrated in the appendix of the book by Wilson [41].

and $\vec{e}_s$ represent the polarization of the incident and scattered radiation, respectively. If a mode is degenerate, the total scattered intensity is found by summing the intensities corresponding to the various Raman tensors of the same mode [2, 56]. Equation (1.12) is widely used in Raman spectroscopy since it determines if a Raman-active mode is in principle observable in a given scattering geometry or not. For instance, one may observe different Raman-active phonons when analyzing the scattered radiation parallel or perpendicular to the propagation direction of the incident radiation. It further follows from the approximation for the scattered intensity above and the spectral differential cross-section in (1.8) that Raman spectra depend on the symmetry type of the Raman-active lattice vibrations, since these determine the elements of the Raman tensor. Thus, Raman spectroscopy is not only sensitive to the chemical elements the crystal is composed of but also to its symmetry characteristics. To emphasize this, equation (1.12) is referred to as the *polarization* or *symmetry selection-rule* in literature.

In summary, lattice vibrations can be classified according to irreducible representations of the crystallographic point group to which the ideal crystal structure belongs. The symmetry characteristics of the lattice vibrations determine whether these are Raman active and induce selection rules on their detectability in an experiment, in addition, to the laws of energy and momentum conservation. Thus, one-phonon Raman spectra only probe lattice vibrations from the center of the Brillouin zone, whose representations transform like a second rank tensor. For a given experimental scattering geometry, these will appear in Raman spectra if they exhibit a nonzero scattering intensity according to the symmetry selection-rule. In the following chapter, perturbations of the ideal crystal structure by defects and their impacts on Raman spectra will be analyzed.

1.3 Perturbations of the ideal crystal structure and their impact on Raman spectra

In reality, there are no perfect crystals as entropy always leads to the formation of lattice defects [6]. The large variety of defects occurring can be classified according to their dimension [27, 57]: zero-dimensional defects are intrinsic point defects, such as vacancies, self-interstitials, or antisite defects, as well as extrinsic point defects, like interstitial or substitutional impurity atoms that have been introduced either by design or unintentionally during the synthesis. Chains of point defects and dislocations are one-dimensional defects. Examples for two-dimensional defects are the crystal surface or stacking faults. Voids or inclusions, among others, are considered to be three-dimensional defects. If the long-range order of the ideal crystal structure is lost and the material is composed of crystallites of varying size and orientation, it is referred to as polycrystalline or amorphous depending on the magnitude of the loss of the long range order.

As it was shown in the previous section 1.2, lattice vibrations of an ideal crystal structure may be observed in Raman experiments if they fulfill certain conditions defined by the laws of energy and momentum (wave vector) conservation as well as by the symmetry characteristics of the crystal structure: first-order Raman processes exhibit a Lorentzian line-shape originating from phonons with a well defined wave vector $\vec{q} \approx 0$ and a frequency ω, and whose irreducible representations of the crystallographic point group transform like a second rank tensor. These constraints might be lifted by perturbations of the ideal crystal structure. In particular, signals of Raman-active modes might vary in line shape and shift in frequency or normally Raman-forbidden modes of the perfect lattice might become Raman active, thus appear in the Raman spectra. The defects themselves can further be excited, exhibiting vibrational modes in Raman spectra that have no analogue to the lattice vibrations of the ideal crystal structure. These aspects are briefly introduced in the following already with regard to the oxide semiconductors studied in this thesis.

Defect modes – local vibrational, gap, or resonant modes

Defects in a crystalline material may give rise to new vibrational modes, which differ in real and frequency space from the lattice vibrations of an ideal crystal structure and, therefore, serving as probes of the defect and its environment [5]. The linear-chain vibration model provides an intuitive understanding of the characteristics of modes introduced by point defects, including vacancies and interstitials, in an otherwise perfect crystal lattice. The model is an oversimplification of the Hamiltonian problem in chapter 1.1, approximating a compound semiconductor by a one-dimensional linear-chain composed of alternating masses m and M connected by springs of force constant k. Restricting the problem to nearest-neighbor interactions and using periodic boundary conditions yields for the equation of motion:

$$\boldsymbol{M} \left(\frac{\partial^2 \vec{x}}{\partial t^2} \right) = \boldsymbol{k} \vec{x} \tag{1.13}$$

with

$$\vec{x} = \left(x_1 \dots x_j \dots x_n \right)^T , \tag{1.14}$$

$$\boldsymbol{M} = \begin{pmatrix} M & 0 & 0 & \dots \\ 0 & m & 0 & \\ 0 & 0 & M & \\ \vdots & & & \ddots \end{pmatrix} , \tag{1.15}$$

and

$$
\boldsymbol{k} = \begin{pmatrix}
2k & -k & 0 & \dots & 0 & -k \\
-k & 2k & -k & & & 0 \\
0 & -k & 2k & & & \vdots \\
\vdots & & & \ddots & & \\
0 & & & & & \\
-k & 0 & \dots & & &
\end{pmatrix} , \tag{1.16}
$$

where n is the number of atoms in the chain and x_j is the displacement of atom j. The matrices $\boldsymbol{k}$ and $\boldsymbol{M}$ are of dimension $n \times n$. Solving the equations of motions for the displacements can be turned into a (simple) diagonalization problem if a harmonic time dependence for the variables is assumed. The eigenvalues ω of the so-called dynamical matrix are the allowed vibrational frequencies and the eigenvectors the corresponding atom motions.

A defect may be introduced into the model, for instance, by simply replacing one atom of the chain by a new atom type of mass m'. As an example consider nitrogen doped ZnO approximated by a diatomic chain of in total 128 zinc and oxygen atoms with masses 65 u and 16 u, respectively, in which the oxygen atom at position 63 in the chain is substituted by a nitrogen atom of mass 14 u. For simplicity, any effects due to different bond lengths in the hexagonal structure of ZnO and to the different charge states of the nitrogen and oxygen atoms are neglected. A numerical solution of this linear-chain model in comparison to the unperturbed case results in a new vibrational mode at a frequency of about $608 \, \text{cm}^{-1}$. Using a larger number of atoms, does not seem to vary the outcome of the model calculation considerably. Figure 1.1(a) is a histogram of the numerically calculated vibrational frequencies, reflecting the phonon density of states (DOS), including the new mode lying above the vibrational bands of the ideal crystal. The spring constant $k = 1.325 \cdot 10^2 \, \text{N/m}$ in the model was chosen such that the upper limit of the optic bands resembles the experimental value of the $E_1(\text{LO})$ phonon frequency of ZnO of about $590 \, \text{cm}^{-1}$. In figure 1.1(b), the displacement of the atoms (eigenvectors) in the linear chain are exemplary shown for three different vibrations. The new mode C, the defect mode, is localized in space. Its amplitude is largest at the defect site (atom position 63) and approaches zero within a distance of a few atoms from the defect site. These elementary considerations illustrate the characteristics of localized modes that originate from vibrations of light impurities and give rise to sharp lines in Raman spectra at frequencies above the optic bands of the ideal crystal structure.

In addition to local vibrational modes, one further distinguishes between gap and resonant modes [40]. Gap modes may be activated by all kinds of defects and occur in the frequency gap of the single phonon DOS of the perfect lattice if such a gap exists at all. These modes are localized in space and give rise to sharp spectral lines. Resonant modes may also be activated by all kinds of defects, in particular, when an atom is substituted by a much heavier isotope. The vibrational amplitude of a resonant mode is enhanced at the defect site but does
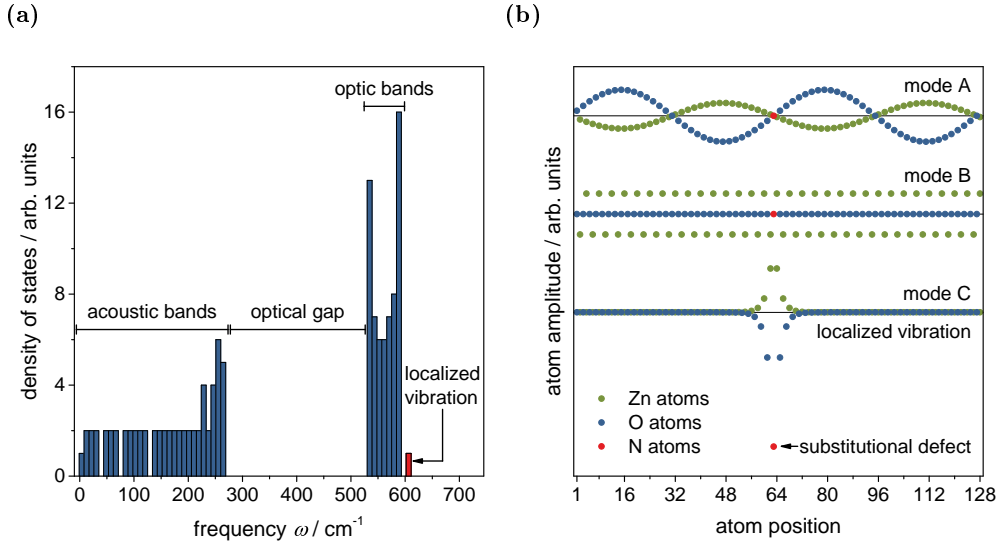
Figure 1.1: Linear-chain model-calculation for N doped ZnO consisting of in total 128 zinc and oxygen atoms. The oxygen atom at position 63 in the chain is substituted by a nitrogen atom. In (a) a histogram of the frequencies (eigenvalues) is shown, resembling the phonon density of states. The mode above the optical bands is due to the N impurity and not present in model calculations for pure ZnO. In (b) the displacement (eigenvectors) of the atoms in the chain are exemplary shown for three different vibrations. Mode C exhibits the characteristic features of a local vibrational mode (LVM) while modes A and B are not influenced by the defect and resemble lattice vibrations of unperturbed ZnO.

not die out far from the defect, in contrast to local vibrational and gap modes. Therefore, these modes are partially localized, giving rise to broader signals within the vibrational bands of the ideal crystal.

With increasing defect concentration, small clusters begin to form in the crystal. These may exhibit a number of vibrations of the localized, gap, and resonant type, thus, differ in real and frequency space from the lattice vibrations of the ideal crystal structure as well.

Defect modes are present in Raman spectra if they introduce a change in polarizability and if their concentration is large enough (about 10^{18} defect atoms/cm^3) to compete against second-order scattering from the host crystal [42]. Details and more sophisticated models for vibrations in disordered solids can be found in the extensive review article by Barker and Sievers from 1975 and in the more recent article by McCluskey from 2000, which covers localized modes of impurities in semiconductors [5, 29].

Besides modes of actually vibrating defect atoms, perturbations of the ideal crystal structure may further lift the Raman activity and wave-vector selection-rules. This may lead to scattering by normally Raman-forbidden lattice vibrations and of phonons with arbitrary wave vectors ($\vec{q} \neq 0$). Such kind of effects

are addressed in the following paragraphs.

Changes in Raman activity – symmetry forbidden modes

The ideal crystal symmetry, defining whether lattice vibrations couple to electromagnetic radiation, may be reduced when an external macroscopic perturbation is applied, e.g., uniaxial stress. According to the Curie principle, the new symmetry group is restricted to a subgroup of the original one, containing only those symmetry operations which are common to both the unperturbed and the perturbed system [28]. The subgroup of the original group representing the perturbed system may contain different irreducible representations than the unperturbed one. Therefore, vibrational modes which are Raman forbidden may become Raman active and degeneracies may be lifted if a macroscopic perturbation is applied that reduces the crystal symmetry.

These considerations may not only hold for macroscopic perturbations. For example, if one atom in an otherwise ideal crystal structure is substituted by an impurity, the symmetry of the crystal is reduced since the translational invariance is lost. In general, the presence of any kind of defect in a crystal breaks the translational symmetry such that the wave-vector (see discussion below) and Raman activity selection-rules derived for the ideal lattice do not strictly hold any longer in Raman spectroscopy. The new symmetry group includes only those operations that leave the defect site invariant. As a consequence, the Raman activity selection-rules for extended phonon states do not hold any longer as the presence of the defect may alter the polarizability change caused by the displacement pattern of the phonon eigenstates. Lowering the symmetry from that of the space group to the site symmetry of the defect may make the original irreducible representation reducible under the operations of the site group, i.e., it may be expanded in terms of irreducible representations of the point group characterizing the defect site. The expansion in the representations of the point group of the defect site may exhibit different behavior than that of the original mode. In particular, the expansion of a originally Raman-forbidden lattice vibration may contain Raman allowed irreducible representations of the point group of the defect site. Thus, vibrational modes that are Raman forbidden become Raman active and degeneracies may be lifted due to the reduction of the symmetry by defects.

In the following, the II-VI semiconductor ZnO that crystallizes in a wurtzite structure belonging to the space group C_{6v}^4 ($P6_3mc$, No. 186) is considered as an example [58, 59]. In ZnO, the oxygen and zinc atoms occupy sites of C_{3v} symmetry [60]. Consequently, substitutional or vacancy defects in ZnO locally reduce the ideal crystal symmetry from the C_{6v} point group to the C_{3v} one. The expansion of the original irreducible representations in the reduced symmetry is given by the correlation table of the C_{6v} point group to its subgroups, depicted in table 1.2, in which bold printed symbols indicate representations transforming like second rank tensors which, hence, may be Raman active. Depending on the orientation, it follows for the C_{3v} point group that the original silent B_1

point group		irreducible representations					
C_{6v}	$(6mm)$	$\mathbf{A_1}$	A_2	B_1	B_2	$\mathbf{E_1}$	$\mathbf{E_2}$
C_6	(6)	$\mathbf{A}$	$\mathbf{A}$	B	B	$\mathbf{E_1}$	$\mathbf{E_2}$
C_{3v} (σ_v)	$(3m)$	$\mathbf{A_1}$	A_2	$\mathbf{A_1}$	A_2	$\mathbf{E}$	$\mathbf{E}$
C_{3v} (σ_d)	$(3m)$	$\mathbf{A_1}$	A_2	A_2	$\mathbf{A_1}$	$\mathbf{E}$	$\mathbf{E}$
C_{2v}	$(mm2)$	$\mathbf{A_1}$	$\mathbf{A_2}$	$\mathbf{B_1}$	$\mathbf{B_2}$	$\mathbf{B_1 \oplus B_2}$	$\mathbf{A_1 \oplus A_2}$
C_3	(3)	$\mathbf{A}$	$\mathbf{A}$	$\mathbf{A}$	$\mathbf{A}$	$\mathbf{E}$	$\mathbf{E}$
C_2	(2)	$\mathbf{A}$	$\mathbf{A}$	B	B	$2\mathbf{B}$	$2\mathbf{A}$
C_S (σ_v)	(m)	$\mathbf{A'}$	$\mathbf{A''}$	$\mathbf{A'}$	$\mathbf{A''}$	$\mathbf{A' \oplus A''}$	$\mathbf{A' \oplus A''}$
C_S (σ_d)	(m)	$\mathbf{A'}$	$\mathbf{A''}$	$\mathbf{A''}$	$\mathbf{A'}$	$\mathbf{A' \oplus A''}$	$\mathbf{A' \oplus A''}$

Table 1.2: Correlation table of the C_{6v} point group and its subgroups [41, 61]. Bold printed symbols indicate representations transforming like second rank tensors, hence, which may be Raman active.

lattice vibration becomes Raman active whereas the B_2 mode remains Raman forbidden or that the B_2 mode becomes Raman active and phonons of B_1 symmetry type remain silent. If the symmetry perturbation is even stronger, e.g., a reduction to the C_{2v} point group, the twofold-degeneracy of each E symmetry type modes is lifted.

It should be noted that group theory based on symmetry arguments only states whether phonon modes couple to electromagnetic radiation, but it cannot predict the magnitude of these effects. The magnitudes depend entirely on the strength of the perturbation caused by the defects.

Relaxation of the wave-vector conservation-rule

In an ideal crystal structure, the momentum (wave vector) conservation restricts the first-order Raman scattering-processes to lattice vibrations from the center of the Brillouin zone ($\vec{q} \approx 0$), as it was shown in section 1.2. If the long-range order (translational symmetry) of the perfect lattice is lost, like in amorphous solids, Bloch's theorem is not longer applicable. Thus, the wave vector is not a good quantum number and the related selection rule is lifted [27]. Assuming that the correlation length, which characterizes the spatial extent of a normal mode vibrating state, in amorphous solids is short compared to optical wavelengths, Shuker and Gammon demonstrated that the wave-vector selection-rule breaks down, that all modes become Raman active, and that the first-order Raman scattering intensity is roughly proportional to the phonon density of states [3, 62]. Based on this picture of nearly localized lattice vibrations, Raman spectra of amorphous solids may not exhibit a discrete set of lines but rather broad

features, being a measure of the phonon DOS, e.g., experimentally observed in amorphous Ge and Si [63].

A relaxation of the wave-vector selection-rule also accounts for the characteristics of Raman spectra of materials between the extreme cases of highly crystalline and amorphous solids, e.g., partially disordered, mircocrystalline, or polycrystalline materials. With decreasing crystallite size, the first-order Raman signals redshift, broaden, and exhibit asymmetric line shapes (combinations of Lorentzian and Gaussian functions). These observations can also be described by the localization of lattice vibrations to a finite volume and a relaxed wave-vector selection-rule, however, not as strongly perturbed as in amorphous solids [64, 65].

In real crystalline samples, the wave-vector selection-rule ($\vec{q} \approx 0$) remains a useful approximation, despite the considerable amount of defects, that, in principle, lift the translational symmetry, like vacancies, impurities, and so on. However, defect-induced lattice vibrations violating the wave-vector selection-rule have been observed. For an overview see chapter 2.1.16 of reference 62.

In summary, defects may give rise to additional modes, which differ in real and frequency space from the lattice vibrations of an ideal crystal, and/or allow normally Raman-forbidden lattice vibrations to become Raman active due to symmetry reduction. If the defects induce such a strong perturbation that the long-range order of the perfect lattice is lost, the position in frequency and the shape of the Raman signals may be altered. In the extreme case of an amorphous solid, Raman spectra do not exhibit a set of discrete lines anymore but rather broad features. There are no general rules established yet when which effect will occur.

2 Experimental setup

To investigate the lattice dynamics of the oxide semiconductors, a commercially available Renishaw inVia Raman microscope is used. In the following paragraphs, the basic setup is described briefly, as well as the experimental methods for carrying out polarization-, pressure-, and temperature-dependent Raman experiments. The chapter ends with a short discussion of the procedure for the determination of phonon frequencies and intensities from experimental Raman spectra.

The experimental Raman setup

A schematic illustration of the optical light path of the experimental setup is depicted in figure 2.1. As excitation sources, three different laser wavelengths have been available: the 532 nm line of a diode-pumped frequency-doubled solid-state laser (50 mW), the 633 nm line of a HeNe laser (30 mW), or the 785 nm line of a diode laser (300 mW). The linearly polarized laser light is focused onto the sample's surface in a optical microscope by Leica Microsystems using a $50\times$ objective (Leica Microsystems, NA 0.75). The scattered radiation is collected by the same microscope in backscattering geometry. It is then dispersed by a spectrometer with a focal length of 250 mm and finally detected by a charged coupled device (CCD) camera. A Rayleigh rejection filter is installed in the light path in front of the spectrometer. It transmits only scattered light above a certain wavelength threshold. Anti-Stokes and Rayleigh scattered light are rejected, whereas the Stokes component of the scattered radiation is transmitted and investigated. For each excitation wavelength a customized Rayleigh rejection filter is required. These possess different wavelength thresholds in the range of about 100 to 300 cm^{-1} above the wavelength of the excitation laser. To study near-excitation Raman bands the Rayleigh rejection filter is replaced by a double monochromator (NExT filter). It allows one to tune the cut off wavelength for the 633 nm laser but leads to a greater loss in scattered intensity due to all the additional optical elements the light has to pass in the monochromator. To a first approximation, the spectral resolution is limited by the focal length, grating type, and slit width of the spectrometer. Table 2.1 lists achievable spectral resolutions. For the standard measurements using the 532 nm excitation laser in this thesis, the systems' spectral resolution is limited to about 5.1 cm^{-1}.
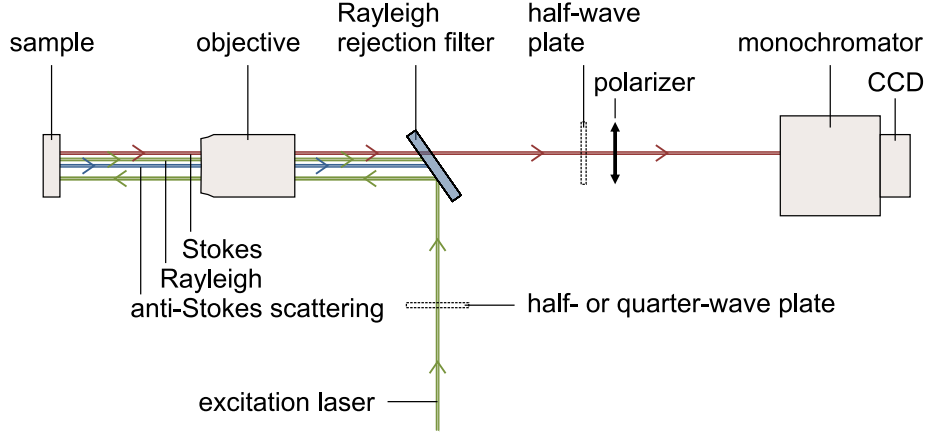
Figure 2.1: Schematic illustration of the experimental setup used for the Raman experiments. The polarizer and the wave plates can be installed optionally to realize various scattering geometries.

Polarization-dependent experiments – Determination of the phonon symmetry character

To analyze the symmetry properties of the lattice vibrations, and hence different Raman tensor elements, see equation (1.12), various polarization geometries can be realized for the visible excitation sources, i.e., for the wavelengths of 532 and 633 nm. If a polarizer is introduced between the Rayleigh rejection filter and the entrance slit of the spectrometer, parallel aligned polarization vectors of the incident laser light and the scattered radiation from the sample can be studied as depicted in figure 2.1. To investigate perpendicularly aligned polarization vectors, a half-wave plate ($\lambda/2$) can be placed in front of the polarizer, such that it rotates the polarization of the scattered light from the sample by 90° ($\pi/2$). The following polarizer then only transmits polarization vectors of the scattered light aligned perpendicularly to the incident one. This may also be achieved by rotating the polarizer by 90°. However, the grating is polarization sensitive and thus the intensity measurements would have been biased. If no additional polarization optics is introduced, all polarization orientations of the scattered radiation are detected simultaneously (unpolarized Raman spectra). It is further possible to rotate the incoming polarization vector of the excitation laser by 90° ($\pi/2$) or to circularly polarize it by introducing a half- or quarter-wave plate, respectively, in the light path of the exciting laser, see figure 2.1.

The various scattering configurations are labeled by the Porto notation [58]: $\vec{k}_i(\vec{e}_i\vec{e}_s)\vec{k}_s$, where the symbols $\vec{k}_i$ and $\vec{k}_s$ outside the parentheses denote the propagation directions of the incident and scattered radiation with respect to the crystal axes, respectively. The direction of their polarization vectors is given by the two symbols $\vec{e}_i$ and $\vec{e}_s$ inside the parentheses. In backscattering geometry,

grating/	slit width/	spectral resolution/cm^{-1}		
(lines/mm)	µm	532 nm	633 nm	785 nm
2400	65	3.8	2.7	
	20	1.2	0.8	
1800	65	5.1	3.6	
	20	1.6	1.1	
1200	65			3.5
	20			1.1

Table 2.1: Spectral resolution (spectral bandpass) of the experimental setup determined accordingly to equation (4.21) in reference 2.

the propagation directions of the incident and scattered light are antiparallel, e.g., $x(yy)\bar{x}$ denotes a measurement in which the incident radiation propagates along the x axis and the scattered radiation is detected along the $-x$ axes while their polarization vectors are directed along the y axis.

To obtain the full symmetry information of the lattice vibrations, the samples can be mounted on a rotating microscope stage. It allows one to rotate the crystal axes in plane with respect to the incident polarization vector of the excitation laser. This is equivalent to the rotation of the plane of polarization. Due to mechanical limitations, it is not possible to perfectly match the center of the rotating microscope stage with the laser line. Therefore, the laser spot is not rotated about a single sample location but covers a small area. The radius covered is about 50 µm in experiment. Assuming that the area covered by the laser during the rotation is homogenous and of one crystal orientation, the influence of the misalignment on the experiment is negligible.

Pressure-dependent experiments

To investigate Raman spectra as a function of hydrostatic pressure a diamond anvil cell (DAC) is used. For that purpose, a small part of a thin film or crystal was scraped or broken off using a thin needle and afterwards placed inside the DAC. A methanol-ethanol (4:1) mixture was used as a liquid pressure medium. The DAC was mounted on the optical microscope equipped with a $50\times$ long-distance objective (Olympus, NA 0.45) to focus the linearly polarized excitation laser into the DAC and to collect the scattered radiation from the sample. In that manner, Raman spectra as a function of hydrostatic pressure were collected at room temperature.

The fluorescence line R_1 of ruby is used as a pressure gauge [66]. For this purpose, ruby powder is placed in the DAC in addition to the sample. The fluorescence lines are fitted using a Lorentzian line-shape assuming a constant background. The wavelength λ of the fluorescence line R_1 almost linearly correlates

to the applied pressure and allows its determination in GPa [67]:

$$P = \frac{A}{B} \left[\left(\frac{\lambda}{\lambda_0} \right)^B - 1 \right] , \qquad (2.1)$$

where $\lambda_0 = 693.95\,\text{nm}$ is the zero pressure value, and $A = 1876$ and $B = 10.71$ are fit parameters. The standard error of the determined pressure values is better than $0.8\,\text{GPa}$ (upper bound) using the laws of propagation of uncertainty with $\Delta A = 6.7$, $\Delta B = 0.14$, and the spectral resolution of the Raman microscope of about $0.14\,\text{nm}$ ($5.1\,\text{cm}^{-1}$) as the relative error for λ and λ_0. The maximal achieved hydrostatic pressure was about $6.5\,\text{GPa}$.

Temperature-dependent experiments

In order to carry out temperature-dependent Raman experiments a Linkam Scientific Instruments heating and freezing microscope stage (THMS600) is attached to the optical microscope. To focus the excitation laser into the temperature stage and to collect the scattered radiation from the sample, the optical microscope is equipped with a $50\times$ long-distance objective (Olympus, NA 0.45). The sample under study is placed onto a silver block inside the temperature stage. It serves as a heating element to increase the sample's temperature up to about $870\,\text{K}$. On the other hand, the silver block can be directly cooled with liquid nitrogen. Thus, experiments in the temperature range between about 80 and $870\,\text{K}$ can be carried out.

Analysis of Raman spectra

The actual values of phonon frequencies or energies and corresponding phonon signal intensities determined from Raman spectra depend on the method how the background is treated, i.e., what is subtracted from the Raman spectra, as well as on the procedure how these quantities are analyzed. In general, neither the shape nor the magnitude, in sense of scattered intensity, of the background in Raman spectra are well known. Various physical processes contribute to it, such as Rayleigh scattering, cosmic rays, photoluminescence, or higher-order Raman scattering-processes from the sample itself or its substrate in case of thin films. Thus, no standard has been established yet on how to correct Raman spectra for its background.

In this thesis, a piecewise linear background is subtracted from the obtained Raman spectra if necessary. The chosen anchor points for the baseline might vary for different sections, however, almost remain the same within a set of Raman spectra that are compared to each other. Subsequently, signal positions and intensities are determined. For this purpose, two different methods are applied: on the one hand, these quantities are estimated by the naked eye. This is a simple approach and quickly carried out, however, the results depend on the experimentalist. On the other hand, the Raman spectra are fitted with

peak functions using the analysis software OriginPro by OrginLab. The latter method seems more sophisticated to yield independent results, but it depends on the line shape, number of signals fitted at the same time, or the fitting range, among others. Thus, it also depends on the experimentalist. Neither method is free of error nor are the determined values but as long as the same procedure is applied to a set of Raman spectra the results can be compared to each other. At the beginning of each analysis, the methods chosen to analyze the Raman spectra are briefly discussed.

3 Lattice dynamics of ZnO − Raman scattering of an ideal crystal structure?

Zinc oxide (ZnO) is a binary II-VI compound semiconductor with a wide and direct band gap. Its properties have been studied since the late 20s of the last century [9]. First Raman spectra of ZnO were published almost 50 years ago in 1966 [58]. Since that time, Raman spectroscopy is commonly used to probe the quality and crystal orientation of ZnO crystals and thin films.

The lattice dynamics of ZnO, in particular, the experimental analysis of the symmetry characteristics of Raman-active lattice vibrations are the subject of the following chapter. It serves as a basis for the study of the perturbed system nitrogen doped ZnO, which will be covered in chapter 4. The first two sections focus on selected properties of ZnO, on its lattice dynamics from a theoretical point of view, as well as on first- and second-order Raman scattering-processes. In the third part, the dependence of the scattered intensity by Raman-active ZnO phonons on sample rotation is analyzed. The findings demonstrate the correlation between the crystal structure, the phonon symmetry types, and the scattered intensities. All experimental results using Raman spectroscopy in this chapter are consistent with the laws of conservation as well as the Raman activity and the symmetry selection-rules established for an ideal hexagonal crystal structure. Inconsistencies with respect to theory are attributed to deviations from the ideal scattering geometry in experiment.

Sample characteristics

The ZnO thin films analyzed in this chapter have been grown by chemical vapor deposition (CVD). Details about the growth process can be found in reference 36. In addition, commercially available pure ZnO crystals from CrysTec GmbH and Tokyo Denpa Co., Ltd. (TEW) grown by a hydrothermal method have been investigated [68, 69]. The analyzed samples possess various crystal orientations.

3.1 Selected properties and lattice dynamics of ZnO

The binary II-VI compound semiconductor ZnO crystallizes in wurtzite structure, which belongs to the hexagonal crystal system [7, 9]. The symmetry
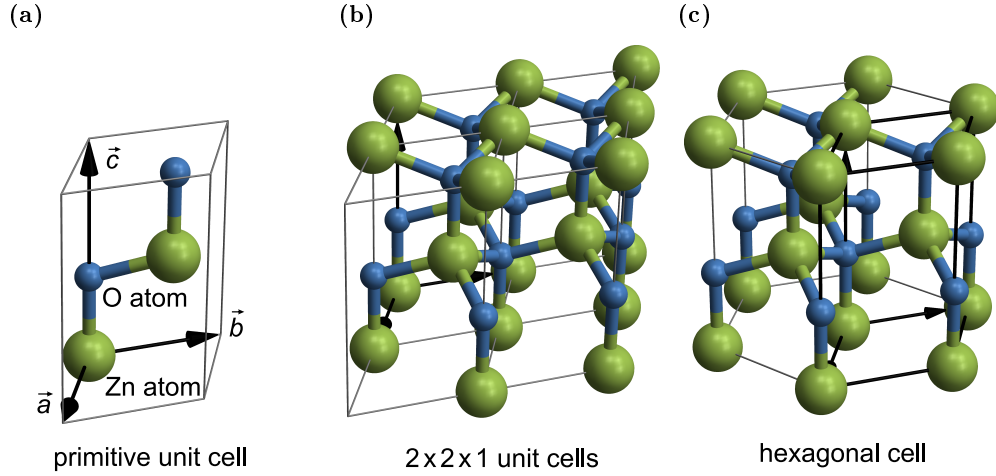
(a)   **(b)**   **(c)**

primitive unit cell   2 x 2 x 1 unit cells   hexagonal cell

Figure 3.1: Schematic illustration of the wurtzite crystal structure of ZnO. In (a) and (b) one and 2×2×1 primitive unit cells are shown, respectively. The latter demonstrates the tetrahedral coordination of the oxygen and zinc atoms. In (c) the hexagonal cell is illustrated. Bold printed lines represent the primitive unit cell.

characteristics of the wurtzite crystal structure are given by the space group C_{6v}^4 ($P6_3mc$, No. 186) and its corresponding point group C_{6v} ($6mm$). As depicted in figure 3.1, each zinc ion (Zn^{2+}) has four oxygen (O^{2-}) neighbors in a tetrahedral configuration and vice versa. This is typical for a sp^3 covalent bonding. However, due to the large differences in electronegativity of oxygen (3.44 in Pauling scale) and zinc (1.65 in Pauling scale) [70], the ZnO bond in the hexagonal crystal structure has a considerable degree of polarity and thus exhibits an additional distinct ionic character. ZnO is colorless and transparent in appearance with a large energy band gap of about 3.3 eV at room temperature [7, 71]. Nominally undoped ZnO is often intrinsically n-type conducting due to intrinsic defects and/or, more likely, due to the incorporation of extrinsic impurities during the growth process such as hydrogen [7–10]. The tetrahedral bonding geometry may also result in a zinc-blende crystal structure, which belongs to the cubic crystal system and whose symmetry properties are described by the space group T_d^2 ($F\bar{4}3m$, No. 216) and its corresponding point group T_d ($\bar{4}3m$). The cubic crystal structure, however, is less favorable than the wurtzite one [7]. In figure 3.1(a) the primitive unit cell of the wurtzite crystal structure is schematically illustrated. The primitive translation vectors $\vec{a}$ and $\vec{b}$ of the unit cell have equal length, include an angle of 120°, and are in the plane perpendicular to the primitive translation vector $\vec{c}$ that is directed along one of the tetrahedral binding orbitals [7, 9]. The hexagonal crystal structure of ZnO has four atoms ($n = 4$) per primitive unit cell, i.e., two ZnO molecular units, leading to $3n = 12$ phonon branches (vibrational eigenmodes) [58, 59]. According to group theory, the modes are classified by the following irreducible representations of the crystallographic point group C_{6v} at the Γ-point
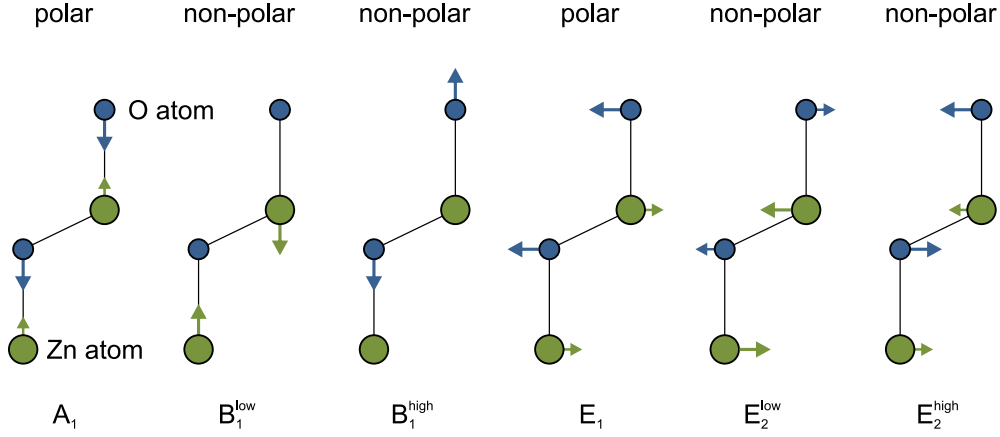
Figure 3.2: Atom displacement (eigenvectors) of the six optical lattice vibrations in wurtzite ZnO according to reference 9.

[58, 59]:

$$\Gamma = 2A_1 \oplus 2B_1 \oplus 2E_1 \oplus 2E_2 \qquad (3.1)$$

Lattice vibrations of symmetry type A and B are non-degenerate, whereas phonons of E symmetry are twofold-degenerate. The three acoustic phonon branches exhibit A_1 and E_1 symmetry character, therefore, the $3n-3 = 9$ optical phonon branches belong to the irreducible representations:

$$\Gamma_{\mathrm{opt}} = A_1 \oplus 2B_1 \oplus E_1 \oplus 2E_2 \qquad (3.2)$$

Using the group theoretical methods introduced in chapter 1.2, one obtains that A_1 phonons are both Raman and infrared active with a polarization parallel to the c axis. The twofold-degenerate phonons of E_1 symmetry type are also Raman and infrared active but polarized in the plane perpendicular to the c axis. Lattice vibrations of E_2 symmetry type are Raman active only and modes of B_1 character are silent, neither Raman nor infrared active.

The displacement of the oxygen and zinc atoms of the six optical lattice vibrations are schematically shown in figure 3.2. The A_1 mode pattern consists of oscillations of the Zn- versus O-sublattices directed along the c axis. Similarly, the two B modes oscillate along the c axis, however, only the zinc sublattice for one mode and only the oxygen sublattice is displaced for the other, referred to as B_1^{low} and B_1^{high}, respectively. Phonons of E symmetry type are directed in the plane perpendicular to the c axis and are thus twofold-degenerate. The E_1 mode pattern consists of oscillations of the Zn- versus O-sublattices, analogous to the A_1 mode pattern. The two phonons of E_2 symmetry character can in principle be divided into oscillations that predominantly involve zinc or oxygen atoms, named E_2^{low} and E_2^{high}, respectively.

Lattice vibrations of symmetry type A_1 and E_1 result in an oscillating polarization (polar modes) and thus induce macroscopic electric fields [56, 58, 59].
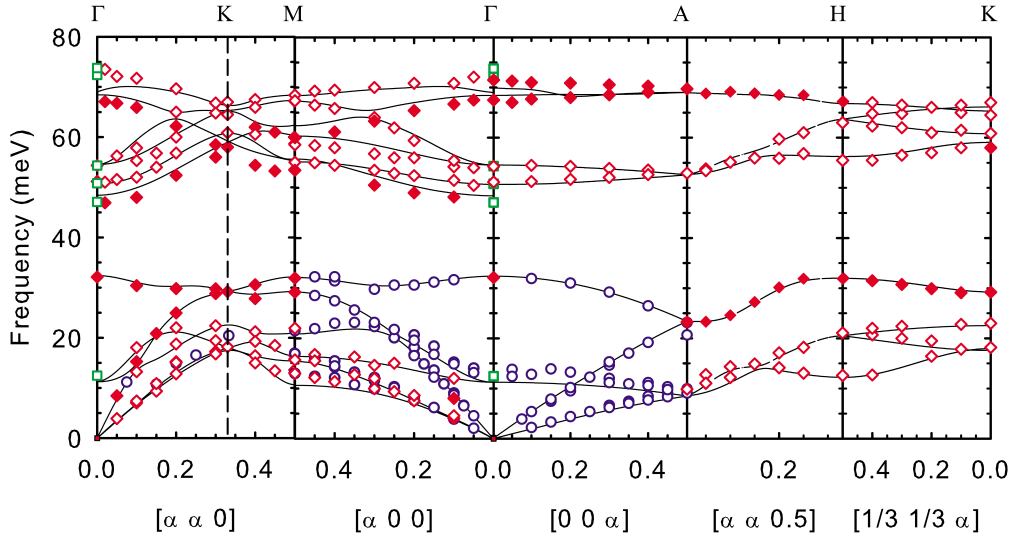
Figure 3.3: Phonon dispersion relation of ZnO along the main symmetry directions in the Brillouin zone [72]. Red diamonds and blue circles represent inelastic neutron scattering data, green squares are Raman data, and solid lines are outcomes of *ab initio* calculations. Reprinted figure with permission from J. Serrano *et al.*, Phys. Rev. B **81** (17), 174304 (2010), http://dx.doi.org/10.1103/PhysRevB.81.174304. Copyright (2015) by the American Physical Society.

These lead to additional restoring forces. As a consequence, the polar modes split into longitudinal (LO) and transverse optical (TO) phonons. Group theory does not account for the splitting of the polar modes since it is confined to non-propagating vibrations at the center of the Brillouin zone ($\vec{q} \approx 0$) [9]. No polarization is induced by the two vibrations of B_1 and E_2 symmetry character. Thus, in total eight optical phonon branches are expected in wurtzite ZnO at the Γ-point: $A_1(LO)$, $A_1(TO)$, B_1^{low}, B_1^{high}, $E_1(LO)$, $E_1(TO)$, E_2^{low}, and E_2^{high}.

The phonon dispersion relation of ZnO for the main symmetry directions in the Brillouin zone is depicted in figure 3.3. It is determined by inelastic neutron scattering and *ab initio* calculations based on density-functional perturbation theory [72]. Overall, an excellent agreement occurs between the experimental data points and the theoretical calculations (solid lines). Further ZnO dispersion relations may be found in references 73, 74, and 75. The dispersion relation can be divided into four regions: (1) acoustic phonons, which pass through the origin, (2) optical phonons between about 100 and 280 cm^{-1} (12.4 to 34.7 meV), involving predominantly oscillating zinc atoms, (3) a forbidden gap between 280 and 380 cm^{-1} (34.7 to 47.1 meV), and (4) optical phonons in the range of about 380 to 600 cm^{-1} (47.1 to 74.4 meV) , involving predominantly oscillating oxygen atoms. In accordance with the considerations above, eight optical phonon branches are found at the center of the Brillouin zone.

Figure 3.3 further visualizes an important property of ZnO crystallizing in the wurtzite structure: due to its hexagonal lattice structure and to the polar character of the A_1 and E_1 symmetry type modes, one has to take into account the phonon propagation direction (phonon wave vector). For example, the $A_1(LO)$ mode is visible along the direction from the Γ- to the A-point, thus along the c axis, but not in a direction perpendicular to it. This has to be kept in mind when studying ZnO specimens of different crystal orientation in the next chapter.

3.2 Raman-active lattice vibrations in ZnO

In the preceding chapter, the lattice dynamics of ZnO crystallizing in a wurtzite structure have been studied from a theoretical point of view. The considerations demonstrated that the maximal number of signals corresponding to one-phonon scattering processes of optical lattice vibrations in a Raman experiment of an ideal wurtzite ZnO crystal structure is six. Usually the number of lattice vibrations observed in experiment is lower because of the selection rules imposed by the scattering geometry and the second rank Raman tensors (see chapter 1.2). For wurtzite ZnO, whose symmetry characteristics are given by the point group C_{6v}, the Raman tensors have the following matrix form [40]:

$$
\begin{pmatrix} a & 0 & 0 \\ 0 & a & 0 \\ 0 & 0 & b \end{pmatrix}
\quad
\begin{pmatrix} 0 & 0 & -c \\ 0 & 0 & 0 \\ -c & 0 & 0 \end{pmatrix}
\quad
\begin{pmatrix} 0 & 0 & 0 \\ 0 & 0 & c \\ 0 & c & 0 \end{pmatrix}
\quad
\begin{pmatrix} 0 & d & 0 \\ d & 0 & 0 \\ 0 & 0 & 0 \end{pmatrix}
\quad
\begin{pmatrix} d & 0 & 0 \\ 0 & -d & 0 \\ 0 & 0 & 0 \end{pmatrix}
$$
$$
A_1(z) \qquad E_1(-x) \qquad E_1(y) \qquad E_2 \qquad E_2
$$
$$
\text{(3.3)}
$$

The coordinate in parenthesis denotes the direction of the phonon polarization. The phonon modes of E symmetry type are twofold-degenerate and their corresponding Raman tensor can be divided into two individual matrices. The matrix form of the Raman tensors depends on the setting of the coordinate axes. The tensors listed in equation (3.3) are defined with respect to the basis axes of a right-angled coordinate system x, y, and z, depicted in figure 3.4(a).[2] For a particular experimental scattering geometry, one can now determine if a Raman active lattice vibration is allowed or forbidden by inserting the appropriate tensors and polarization vectors, given with respect to the axes x, y, and z, in the approximation for the scattered intensity in equation (1.12). Table 3.1 lists the symmetry selection-rules of zone-center optical phonons in wurtzite ZnO for various scattering configurations.

---

[2]An alternative orientation of the coordinate axes is given in the book by Koster, in which the x axis of the right-angled coordinate system is oriented perpendicularly to the a-plane and accordingly the y axis is parallel to the a-plane [61]. The z axis is chosen in the same manner as in figure 3.4(a), parallel to the sixfold rotation axis. The matrix form of the Raman tensors is the same in both coordinate systems.
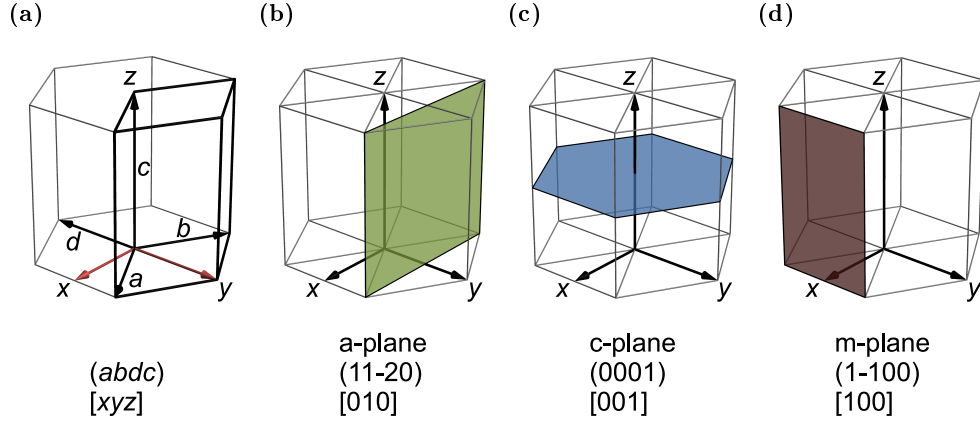
Figure 3.4: (a) Schematic illustration of the orientation of the primitive unit axes a, b, and c in the hexagonal structure with respect to the orthogonal co-ordinate axes x, y, and z. On the basis of the latter axes the Raman tensors are defined in the hexagonal crystal system belonging to the point group C_{6v}. (b)-(d) Illustration of three lattice planes in the hexagonal structure which are commonly used ZnO crystal orientations. Below each representation, the Bravais Miller indices ($abdc$) of the lattice planes and their corresponding normal vectors, represented in the right-angled coordinate system (xyz), are given.

| mode | frequency/ cm^{-1} | parallel polarization | | | crossed polarization | | |
		$x(yy)\bar{x}$ $y(xx)\bar{y}$	$x(zz)\bar{x}$ $y(zz)\bar{y}$	$z(xx)\bar{z}$ $z(yy)\bar{z}$	$x(yz)\bar{x}$ $x(zy)\bar{x}$	$y(xz)\bar{y}$ $y(zx)\bar{y}$	$z(xy)\bar{z}$ $z(yx)\bar{z}$
E_2^{low}	100	×	-	×	-	-	×
B_1^{low}	261	-	-	-	-	-	-
$A_1(TO)$	378	×	×	-	-	-	-
$E_1(TO)$	410	-	-	-	×	×	-
E_2^{high}	438	×	-	×	-	-	×
B_1^{high}	552	-	-	-	-	-	-
$A_1(LO)$	575	-	-	×	-	-	-
$E_1(LO)$	590	-	-	-	-	-	-

Table 3.1: Symmetry selection-rules of zone-center optical phonons in wurtzite ZnO for various scattering configurations denoted in the Porto notation. The listed phonon frequencies are experimental values at room temperature with the exception of the values for lattice vibrations of B symmetry type. The latter are silent modes and the corresponding phonon frequencies are results of *ab initio* calculations taken from reference 73.

First-order or one-phonon Raman scattering

Figure 3.5 depicts Raman spectra of CVD grown and hydrothermally grown wurtzite ZnO samples with different crystal orientations, defined in figure 3.4(b), (c), and (d). The spectra were recorded at room temperature using a linearly polarized 532 nm laser for excitation, and analyzing the polarization vector of the scattered radiation parallel to that one of the incident excitation laser. Depending on the sample orientation and, therefore, on the scattering configuration, different Raman-active one-phonon processes (dashed lines) are allowed: the four modes located at about 378, 410, 438, and 575 cm^{-1} are the Raman-active phonons of $A_1(TO)$, $E_1(TO)$, E_2^{high}, and $A_1(LO)$ symmetry character, respectively. The $E_1(LO)$ phonon at a frequency of about 590 cm^{-1} is not allowed in the scattering geometries considered here, see table 3.1. Due to the limited transmission range of the Rayleigh rejection filters in the microscope, the E_2^{low} mode at about 100 cm^{-1} is not completely accessible and, therefore, will not be analyzed in the following. For the spectra shown in figure 3.5, the samples have been aligned such that the $E_1(TO)$ mode is minimal and thus the intensity of the E_2^{high} mode is maximal. The lattice vibration of $A_1(LO)$ symmetry type exhibits a spectral feature that is weak in intensity. This is caused by a destructive interference of the deformation potential with the Fröhlich contribution, according to Callender *et al.* [76]. All experimentally observed Raman-active phonons are in accordance with the symmetry selection-rules summarized in table 3.1, e.g., phonons of $A_1(LO)$ and E_2 symmetry character are allowed for scattering of a c-plane oriented sample ($z(xx)\bar{z}$) and only those are observed in experiment.

Second-order or two-phonon Raman scattering

In first-order Raman scattering, the wave-vector conservation restricts the scattered phonons to the center of the Brillouin zone ($\vec{q} \approx 0$). This constraint of a nearly vanishing wave vector is limited to the sum of wave vectors in case of second- or higher-order Raman scattering. Thus, lattice vibrations from the entire Brillouin zone will be accessible in the experiment if the corresponding higher-order scattering-process is Raman active. The scattered intensity of higher-order processes is, in principle, governed by the phonon density of states or rather by the likelihood of the scattering process. As a typical example figure 3.6 shows the feature-rich structures caused by two-phonon scattering-processes in the range of 100 to 950 cm^{-1} of wurtzite ZnO specimens with different crystal orientations. The assignments of the spectral features in figure 3.6 to higher-order scattering-processes follows the work by Cuscó *et al.* [77].

Table 3.2 lists second-order scattering-processes in the range of 200 to 1000 cm^{-1} in wurtzite ZnO including their symmetry characters determined from experiment [77]. The latter are in agreement with the ones predicted by a group theoretical analysis of the perfect wurtzite lattice structure by Siegle *et al.* [78].
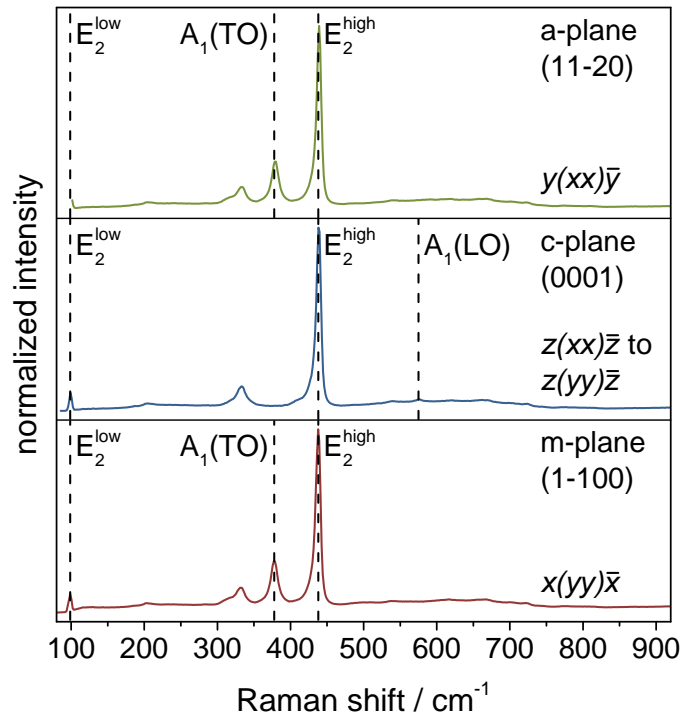
Figure 3.5: First-order Raman scattering-processes of wurtzite ZnO samples with different crystal orientations, hence for different scattering configurations. The spectra were recorded at room temperature using a linearly polarized 532 nm laser for excitation. The scattering configuration is denoted in the Porto notation. Black, dashed lines indicate allowed Raman-active ZnO phonons.
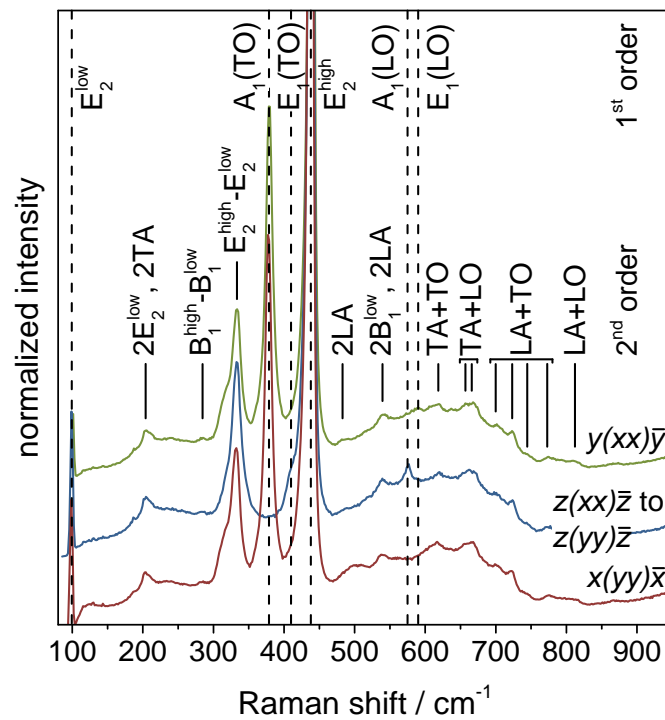
Figure 3.6: Enlarged view of the Raman spectra of wurtzite ZnO shown in figure 3.5. The spectra depict the rich structure of higher-order scattering-processes indicated by black, solid lines. The assignment of the spectral features follows the work by Cuscó *et al.* [77]. Black, dashed lines indicate first-order Raman scattering-processes in ZnO.

frequency/cm^{-1}		scattering	Brillouin zone	symmetry character	
here	ref. 77	process [77]	points/lines [77]	exp. [77]	th. [78]
204	203	$2E_2^{low}$; 2TA	Γ; L, M, H	A_1, (E_2)	A_1, E_2; -
284	284	B_1^{high}–B_1^{low}	Γ	A_1	A_1
333	333	E_2^{high}–E_2^{low}	Γ	A_1, (E_2, E_1)	A_1, E_2
	483	2LA	M-K	A_1	-
540	536	$2B_1^{low}$; 2LA	Γ; L, M, H	A_1	A_1; -
619	618	TA+TO	H, M	A_1	-
657	657	TA+LO	L, H	E_1, E_2	-
668	666	TA+LO	M	A_1	-
702	700	LA+TO	M	A_1	-
724	723	LA+TO	L-M	A_1	-
	745	LA+TO	L-M	A_1	-
773	773	LA+TO	M, K	A_1	-
	812	LA+LO	L, M	A_1	-
	980	2TO	L-M-K-H	A_1	-

Table 3.2: Room temperature frequencies of second-order Raman scattering-processes in wurtzite ZnO and their corresponding symmetry characters determined from experiment (exp.) in comparison to the ones predicted by a group theoretical analysis (th.) of the ideal wurtzite structure. Excerpt from table II in reference 77 and from table II in reference 78.

An analysis of the higher-order scattering-processes is essential to avoid misinterpretations of spectral features in Raman spectra of perturbed crystals. For example, defect modes often only exhibit weak scattering intensities, similar to the intensities of higher-order processes of the host material, and are therefore easily misidentified.

3.3 Probing the symmetry characteristics of Raman-active lattice vibrations

The first Raman spectra of crystalline ZnO, including polarization-dependent experiments and an analysis of the lattice dynamics of the wurtzite crystal structure by group theory were published almost 50 years ago by Damen *et al.* in 1966 [58]. Based on their findings, the symmetry types of the phonons in wurtzite ZnO were identified. The detailed analysis of the properties of the polar phonons and the discussion of the various scattering configurations in need to observe all phonons in wurtzite semiconductors by Arguello *et al.* from 1969 is also worth mentioning in this context [59]. In the following section, the established assignment of the irreducible representations of the C_{6v} point group to phonons in wurtzite ZnO will be reviewed. This is accomplished by making use of the dependence of scattered intensity on the orientation of the crystal axes
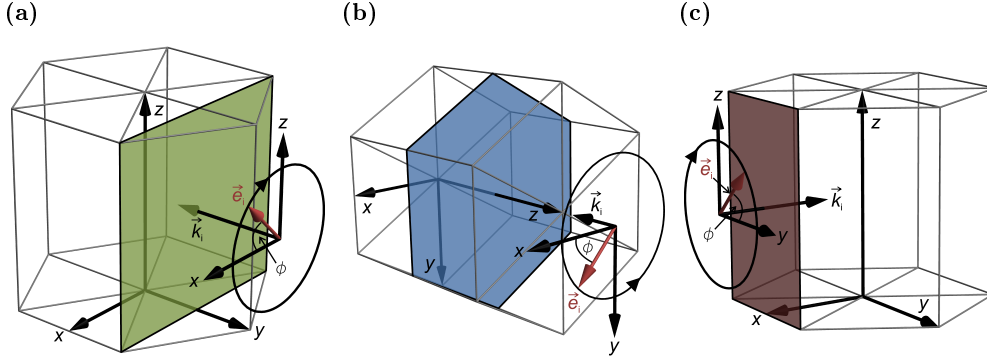
Figure 3.7: Schematic illustration of the orientation of the wave vector $\vec{k}_i$ and the polarization vector $\vec{e}_i$ for a rotation of the hexagonal crystal structure about (a) the y axis (normal to the a-plane), (b) the z axis (normal to the c-plane), and (c) the x axis (normal to the m-plane). The circles denote the rotation of the polarization vector and ϕ is the rotation angle.

with respect to the propagation direction of the incident and scattered radiation as well as on the orientations of their polarization vectors. In particular, the intensity dependence on the rotation of the sample will be studied. This is equivalent to the rotation of the plane of polarization and allows one to analyze the symmetry properties of the lattice vibrations, to confirm their assignment to symmetry characters, and to determine the ratios of the Raman tensor elements in wurtzite ZnO.

Theoretical calculation of the dependence of the scattered Raman intensity on sample rotation

At first, the procedure how to analyze the symmetry characteristics is introduced from the point of view of theory: figure 3.7(a), (b), and (c) schematically illustrate the orientation of the wave vector $\vec{k}_i$ and the polarization vector $\vec{e}_i$ of the excitation laser for a rotation of the sample about the x, y, or z axis with respect to the hexagonal crystal structure. The polarization vector is not necessarily aligned to one of the crystal axes, but lies in the xz- (a-plane), xy- (c-plane), or yz-plane (m-plane). To calculate the dependence of the scattered Raman intensity on the rotation angle, the polarization vectors are represented in polar coordinates, e.g., a vector rotating in the a-plane about the y axis has the form:

$$\vec{e}_{i,a} = \begin{pmatrix} \cos(\phi) \\ 0 \\ \sin(\phi) \end{pmatrix}, \tag{3.4}$$

where ϕ is the rotation angle between incident polarization vector $\vec{e}_{i,a}$ and the x axis. The polarization of the scattered light may now be analyzed paral-

lel or perpendicularly to the incident one, thus one obtains in polar coordinates:

$$\vec{e}_{\mathrm{s,a}}^{\,\parallel} = \begin{pmatrix} \cos(\phi) \\ 0 \\ \sin(\phi) \end{pmatrix} \tag{3.5}$$

or

$$\vec{e}_{\mathrm{s,a}}^{\,\perp} = \begin{pmatrix} -\sin(\phi) \\ 0 \\ \cos(\phi) \end{pmatrix}, \tag{3.6}$$

where $\parallel$ and $\perp$ denote parallel and perpendicularly oriented incident and scattered polarization vectors, respectively. Inserting these polarization vectors and the Raman tensors of wurtzite ZnO in equation (1.12) yields the dependence of the scattered Raman intensity on sample rotation about the y axis. For example, one obtains for modes of E_2 symmetry character ($y(xx)\bar{y} \leftrightarrow y(zz)\bar{y}$):

$$
\begin{aligned}
I^{\,\parallel}(E_2) \propto{}& \left| \begin{pmatrix} \cos(\phi) \\ 0 \\ \sin(\phi) \end{pmatrix}^T \begin{pmatrix} 0 & d & 0 \\ d & 0 & 0 \\ 0 & 0 & 0 \end{pmatrix} \begin{pmatrix} \cos(\phi) \\ 0 \\ \sin(\phi) \end{pmatrix} \right|^2 \\
&+ \left| \begin{pmatrix} \cos(\phi) \\ 0 \\ \sin(\phi) \end{pmatrix}^T \begin{pmatrix} d & 0 & 0 \\ 0 & -d & 0 \\ 0 & 0 & 0 \end{pmatrix} \begin{pmatrix} \cos(\phi) \\ 0 \\ \sin(\phi) \end{pmatrix} \right|^2 \\
\propto{}& \left| d \cos^2(\phi) \right|^2
\end{aligned}
\tag{3.7}
$$

The dependence of scattered intensities of any Raman-active ZnO phonon on the rotation of the sample about the x, y, and z axis can be determined similarly. The outcomes of such calculations are listed in table 3.3 and clearly show a distinct correlation between scattered intensity and symmetry character of the modes, which makes them distinguishable from each other and allows their identification in experiment.

Probing the dependence of the scattered Raman intensity on sample rotation by the experiment

Corresponding Raman experiments have been carried out on hydrothermally grown a-plane and CVD grown c-plane oriented ZnO specimens, thus for the rotation of the samples about the y or z axis of the wurtzite crystal structure, respectively. The Raman spectra have been recorded in backscattering geometry at room temperature using a linearly polarized 532 nm laser for excitation. Figure 3.8(a) depicts Raman spectra of the a-plane oriented ZnO sample for various rotation angles about the y axis ($y(xx)\bar{y} \leftrightarrow y(zz)\bar{y}$). The spectra are shifted vertically by a constant amount for clarity. Between 0° and 180° the E_2^{high} phonon reaches a single intensity maximum at about 90°, whereas the $E_1(TO)$ mode exhibits two maxima at 40° and 120°, and three minima at 0°,

	Raman mode	scattered Raman intensity I upon sample or plane of polarization rotation	
		$x(yy)\bar{x} \leftrightarrow x(zz)\bar{x}$	$x(yz)\bar{x} \leftrightarrow x(zy)\bar{x}$
m-plane, x axis	A_1	$|a|^2|\cos(\phi)|^4 + |b|^2|\sin(\phi)|^4 + \frac{1}{2}ab|\sin(2\phi)|^2\cos(\chi)$	$\frac{1}{4}|\sin(2\phi)|^2 \cdot [|a|^2 + |b|^2 - 2ab\cos(\chi)]$
	$E_1(-x)$	0	0
	$E_1(y)$	$|c|^2|\sin(2\phi)|^2$	$|c|^2|\cos(2\phi)|^2$
	E_2	$|d|^2|\cos(\phi)|^4$	$|d|^2|\sin(\phi)|^2|\cos(\phi)|^2$
		$y(xx)\bar{y} \leftrightarrow y(zz)\bar{y}$	$y(xz)\bar{y} \leftrightarrow y(zx)\bar{y}$
a-plane, y axis	A_1	$|a|^2|\cos(\phi)|^4 + |b|^2|\sin(\phi)|^4 + \frac{1}{2}ab|\sin(2\phi)|^2\cos(\chi)$	$\frac{1}{4}|\sin(2\phi)|^2 \cdot [|a|^2 + |b|^2 - 2ab\cos(\chi)]$
	$E_1(-x)$	$|c|^2|\sin(2\phi)|^2$	$|c|^2|\cos(2\phi)|^2$
	$E_1(y)$	0	0
	E_2	$|d|^2|\cos(\phi)|^4$	$|d|^2|\sin(\phi)|^2|\cos(\phi)|^2$
		$z(xx)\bar{z} \leftrightarrow z(yy)\bar{z}$	$z(xy)\bar{z} \leftrightarrow z(yx)\bar{z}$
c-plane, z axis	A_1	$|a|^2$	0
	$E_1(-x)$	0	0
	$E_1(y)$	0	0
	E_2	$|d|^2$	$|d|^2$

Table 3.3: Theoretical dependence of the scattered intensity I on sample or plane of polarization rotation about the x, y, or z axis of the hexagonal structure. Model functions in columns three and four describe the characteristic dependences of Raman-active phonons in wurtzite ZnO for parallel and perpendicularly oriented incident and scattered polarization vectors, respectively. The rotation is given by the angle ϕ between the incident polarization vector $\vec{e}_i$ and an axes of the right-angled coordinate system defined in figure 3.7. The variable χ is the phase difference between the complex Raman tensor elements a and b belonging to the A_1 mode.
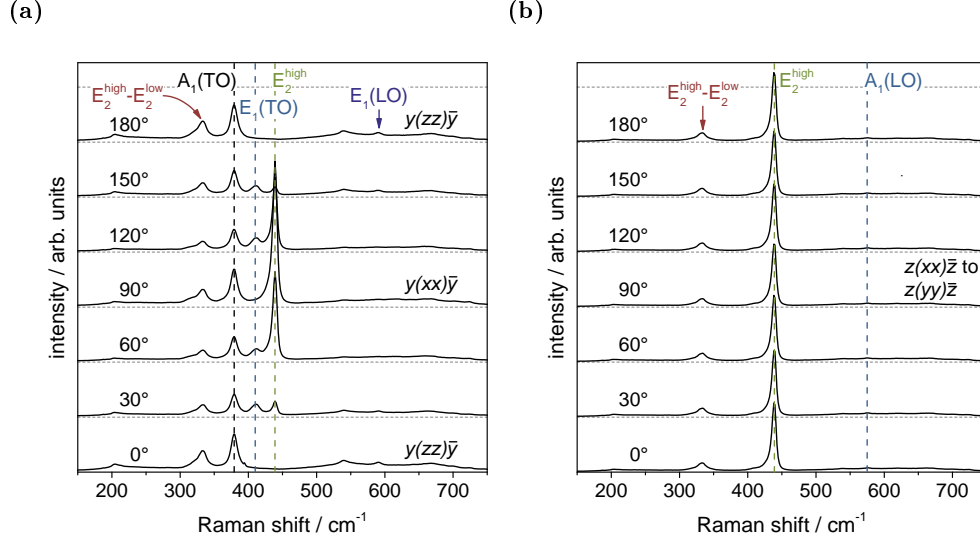
(a) (b)

Figure 3.8: Raman spectra of (a) a-plane and (b) c-plane oriented ZnO for various polarization orientations of the incident laser with respect to the crystal axes. The spectra were recorded at room temperature using a linearly polarized 532 nm laser for excitation. The numbers are experimental rotation angles and dashed lines indicate allowed first-order Raman scattering-processes. For clarity, the spectra have been shifted on the axis of ordinates.

90°, and 180°. In comparison to the $E_1(TO)$ phonon, the $A_1(TO)$ mode is phase shifted by 90° being maximal when the $E_1(TO)$ mode is minimal and vice versa. In contrast, the Raman spectra shown in figure 3.8(b) of the c-plane oriented ZnO specimen rotated about the z axis ($z(xx)\bar{z} \leftrightarrow z(yy)\bar{z}$) reveal that phonon signals of $A_1(LO)$ and E_2^{high} symmetry character are independent of the sample rotation.

The prominent features in the measured spectra were fitted with combinations of Gaussian and Lorentzian functions assuming a linear background in the range of 275 to 525 cm^{-1} for the $A_1(TO)$, $E_1(TO)$, and E_2^{high} phonon signals and in a narrow range around the $A_1(LO)$ one, chosen individually for each spectrum. In fact, the mode of E_2^{high} symmetry character is best described with a Fano-like line-shape due to its decay into a sum of longitudinal and transverse acoustic phonons [77, 79]. However, fitting with a Fano-like line-shape does not seem to improve the results of the peak positions and integrated areas. This might be due to the limited spectral resolution of about 5.1 cm^{-1} in the experiment and to the simplified assumption that the background possesses a linear shape. The results of these fits are shown in figure 3.9 and 3.10, in which the integrated peak area of each phonon signal is plotted versus the rotation angle for both polarization configurations, i.e., for parallel and perpendicularly oriented incident and scattered radiation. The error bars are the standard errors of the integrated area. Due to the fitting routine, the standard error of the Gaussian functions could not be estimated. In these cases, the largest observed stan-

dard error of fits with Lorentzian functions was used as an upper limit for that mode. Obviously, each Raman signal exhibits a distinct intensity dependence on rotation. Comparing these findings to the results in table 3.3 confirms the assignment of the symmetry characters and phonon signals in wurtzite ZnO. For example, only the signal at about $438\,\mathrm{cm}^{-1}$ reveals a dependence on rotation about the y axis for parallel aligned polarization vectors which is given by the calculation in equation (3.7). Thus, it can be identified with E_2 symmetry character. Discrepancies between experiment and theory are due to deviations from an ideal experimental geometry, which will be discussed in the following.

In figure 3.9(a), the derived intensities of the prominent features of the a-plane oriented ZnO sample for parallel aligned incident and scattered polarization vectors are shown versus the rotation angle $(y(xx)\bar{y} \leftrightarrow y(zz)\bar{y})$. The top graph depicts the peak areas of the lattice vibrations of $A_1(TO)$, $E_1(TO)$, and E_2^{high} symmetry character. The data points were fitted with the model functions in table 3.3 weighted by the standard errors of the integrated area (solid lines) to determine the Raman tensor elements. The findings for the phonons of $A_1(TO)$ symmetry character are only described correctly if the Raman tensor elements a and b are complex numbers. Thus, these may exhibit a nonzero phase difference χ. An appropriate value for the phase difference can account for the experimentally observed nonzero minimum Raman intensity and the $\pi/2$ ($90°$) periodicity of the signal. At first glance, complex Raman tensor elements are not allowed as the energy of the excitation laser below the band gap infers that the imaginary part of the dielectric function is zero. However, lattice vibrations of A_1 and E_1 symmetry type are both Raman and infrared active. Hence they exhibit a nonzero imaginary part of the dielectric function as demonstrated by infrared spectroscopic ellipsometry [80]. This may explain why the Raman tensor elements of the A_1 mode are complex numbers. Accordingly, the Raman tensors elements of E_1 symmetry type phonons may be complex numbers as well. These tensors only possess one single element, see equation (3.3). Thus, no phase difference is introduced when calculating the square of the absolute value.

The spectra of a-plane ZnO further exhibit a strong mode at about $332\,\mathrm{cm}^{-1}$ besides the three Raman-active one-phonon signals. This additional mode is assigned to the difference process $E_2^{\mathrm{high}} - E_2^{\mathrm{low}}$. Such a combination mode contains irreducible representations of A_1, A_2 (not Raman active), and E_2 symmetry character according to group theory, see table 3.2. The experimentally determined peak areas of the difference mode are given in the center of figure 3.9(a). They reveal a dependence on rotation similar to that of the lattice vibration of A_1 symmetry type. However, the data points do not perfectly match each other, e.g., the periodicity of the $A_1(TO)$ phonon signal is $\pi/2$ ($90°$) and that of the difference mode is about π ($180°$). One can account for these discrepancies by adjusting the ratio of the Raman tensor elements a and b. Hence, one can describe the difference mode $E_2^{\mathrm{high}} - E_2^{\mathrm{low}}$ by the same model function as that of the $A_1(TO)$. This finding is in good agreement with the results by
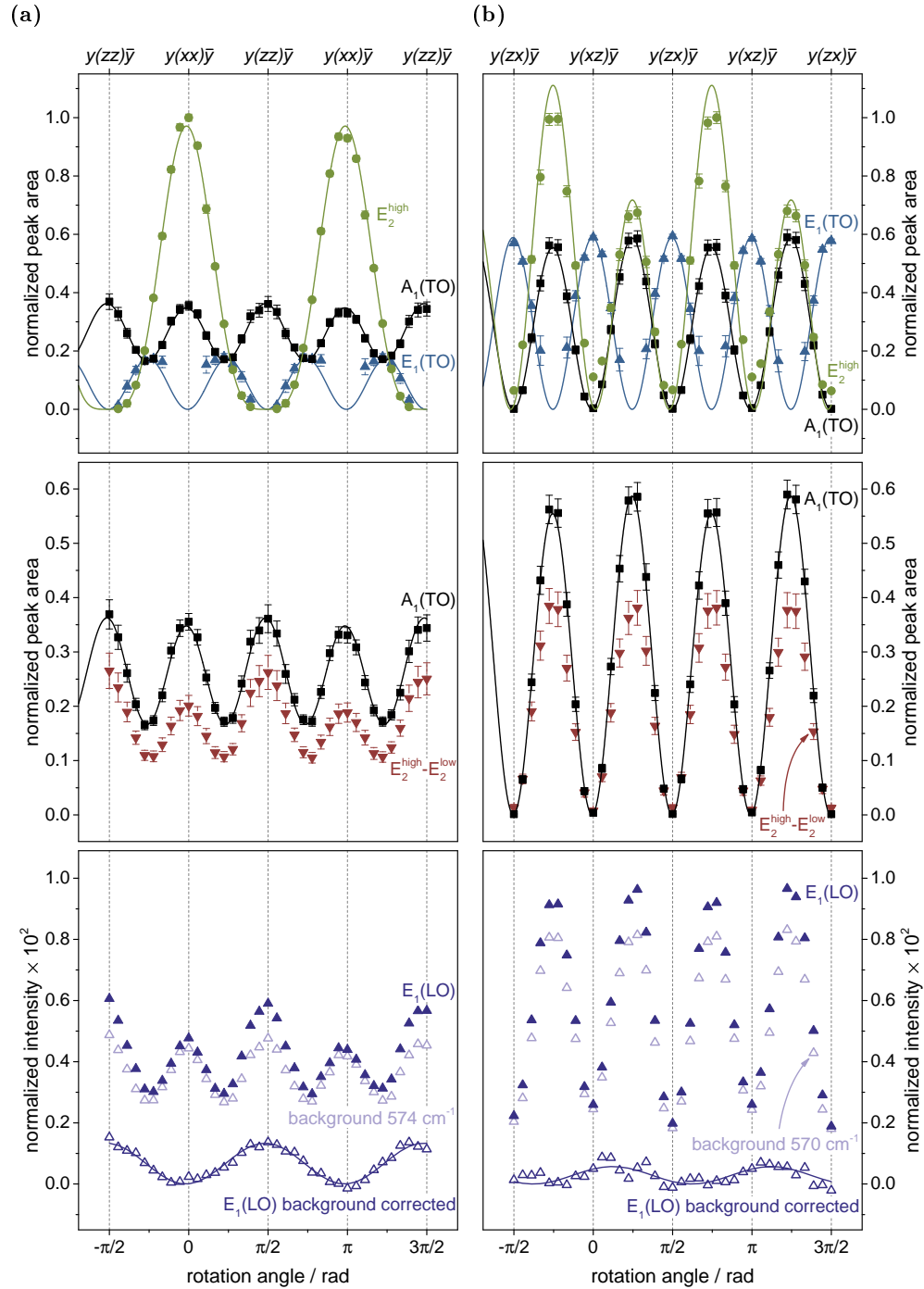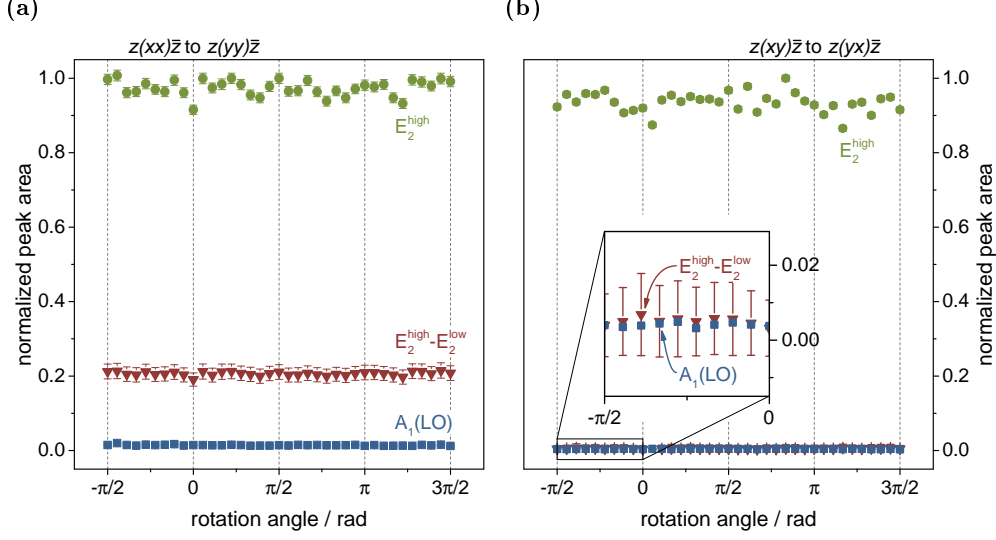
Figure 3.9: Normalized intensity of the prominent Raman signals of an a-plane oriented ZnO specimen versus sample rotation about the y axis for (a) parallel and (b) perpendicularly aligned incident and scattered polarization vectors. Signals are normalized to the maximum intensity of the E_2^{high} phonon. Solid lines are fits to the data points.

Figure 3.10: Normalized intensity of the prominent Raman signals of a c-plane oriented ZnO specimen versus sample rotation about the z axis for (a) parallel and (b) perpendicularly aligned incident and scattered polarization vectors. Signals are normalized to the maximum intensity of the E_2^{high} phonon.

Cuscó *et al.*, whose observations indicate that the symmetry of the $E_2^{high}-E_2^{low}$ feature is predominantly of A_1 character [77].

A closer look at the Raman spectra of the a-plane oriented ZnO sample reveals a weak spectral feature at about $590\,cm^{-1}$. Its frequency suggests a lattice vibration of $E_1(LO)$ character which is symmetry forbidden in backscattering geometry. Symmetry forbidden lattice vibrations may be observed in the experiment due to deviations from the ideal scattering geometry, e.g., caused by a slightly tilted sample. Such a deviation may cause a constant component p of the polarization along the normal axis of the sample's surface as illustrated in figure 3.11(a). Taking such effects into account, the polarization vectors for the incident and scattered radiation with respect to an a-plane oriented sample have the modified form:[3]

$$\vec{e}_{i,a} = \frac{1}{\sqrt{1+p^2}} \cdot \begin{pmatrix} \cos(\phi) \\ p \\ \sin(\phi) \end{pmatrix} = \vec{e}_{s,a}^{\parallel} \tag{3.8}$$

$$\vec{e}_{s,a}^{\perp} = \frac{1}{\sqrt{1+p^2}} \cdot \begin{pmatrix} -\sin(\phi) \\ p \\ \cos(\phi) \end{pmatrix} \tag{3.9}$$

Inserting these polarization vectors and the Raman tensors of wurtzite ZnO in equation (1.12) yields a nonzero intensity of the $E_1(y)$ mode that represents the

---

[3]Note: Because of the deviations from the ideal scattering geometry in experiment, the scalar product of the modified polarization vectors $\vec{e}_{i,a}$ and $\vec{e}_{s,a}^{\perp}$ is nonzero, therefore they are not perpendicularly oriented to each other anymore.
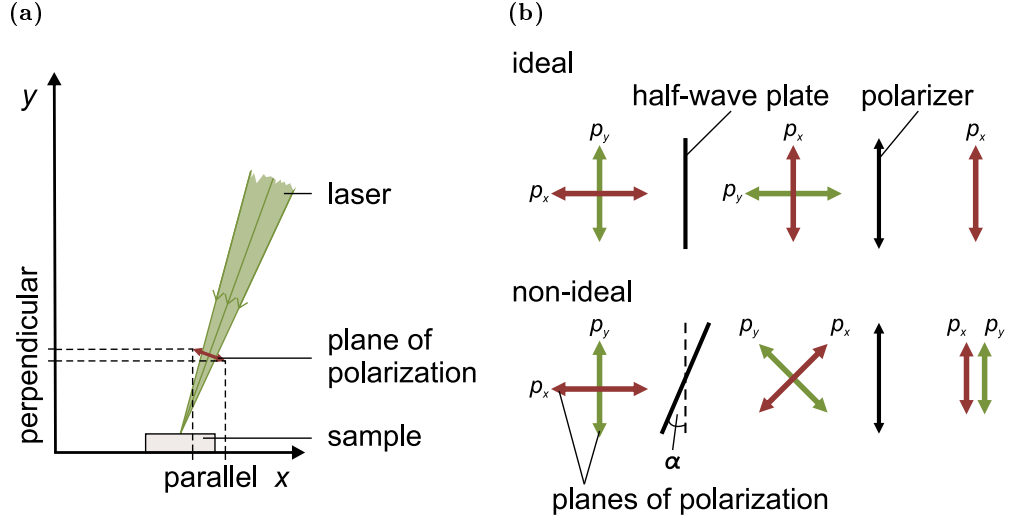
(a)

(b)

Figure 3.11: Schematic illustration of deviations from an ideal experimental geometry that lead to typical difficulties in measuring a zero signal. (a) Titled sample with respect to the incident laser. This results in a nonzero component of the polarization along the normal axis of the sample's surface. (b) Misalignment of the half-wave plate and the polarizer by an angle α. Both polarization components p_x and p_y pass the polarizer to a certain extent.

phonon of $E_1(LO)$ symmetry character:

$$I^{\parallel}(E_1(y)) \propto \left| \frac{2cp\sin(\phi)}{1+p^2} \right|^2 \tag{3.10}$$

$$I^{\perp}(E_1(y)) \propto \left| \frac{cp(\sin(\phi)+\cos(\phi))}{1+p^2} \right|^2 \tag{3.11}$$

As long as the polarization component p along the normal axis of the sample's surface is small, its influence on the remaining lattice vibrations of symmetry type A_1, $E_1(TO)$, and E_2 upon sample rotation seems to be negligible.

For simplicity, the intensity of the $E_1(LO)$ signal was determined by the naked eye and plotted versus the rotation angle for both polarization configurations in the lower graphs of figure 3.9. It is located in the frequency region of second-order scattering-processes and exhibits only a weak signal intensity. Therefore, the behavior of the background has to be considered. Signals close in Raman shift to the $E_1(LO)$ phonon at 574 and $570\,\mathrm{cm}^{-1}$ are included in the lower graphs of figure 3.9 (purple, open triangles). These demonstrate that the background is angle dependent. The $E_1(LO)$ signal is well described by equations (3.10) and (3.11) (solid lines) after subtracting an $[\sin^2(2\phi) + y]$ angle-dependent background.

In figure 3.9(b), the estimated intensities of the prominent features of the a-plane oriented ZnO specimen for perpendicularly aligned incident and scattered

polarization vectors are shown versus the rotation angle $(y(xz)\bar{y} \leftrightarrow y(zx)\bar{y})$. Each lattice vibration reveals a specific intensity dependence on sample rotation in the experiment. However, those are not reflected correctly by the model functions listed in table 3.3. For example, the peak area of the phonon of E_2^{high} symmetry character, depicted in the top graph of figure 3.9(b), exhibits a periodicity of π (180°) in experiment, but it is expected to follow a product of sine and cosine functions according to the model calculations. Hence a $\pi/2$ (90°) periodicity is expected. This is caused by the imperfect alignment of the polarizer and the half-wave plate ($\lambda/2$) in the setup, leading to the detection of parallel and perpendicularly polarized light simultaneously, as illustrated in figure 3.11(b). To account for such a deviation from the ideal scattering geometry of an a-plane oriented sample, the scattered polarization vector has to be modified to

$$\vec{e}_{s,a}^{\perp} = \begin{pmatrix} \cos(\phi)\sin\alpha - \sin(\phi)\cos\alpha \\ 0 \\ \sin(\phi)\sin\alpha + \cos(\phi)\cos\alpha \end{pmatrix}, \tag{3.12}$$

where α is the tilt angle between the polarizer and the half-wave plate ($\lambda/2$). The solid lines in the top and center graphs of figure 3.9(a) are based upon the model functions in table 3.3, whereas the ones in the top and center graphs of figure 3.9(b) are based on model calculations using the modified polarization vector in equation (3.12). The fits are in excellent agreement with the data points. As expected, the estimated intensity dependence of the second-order process $E_2^{high} - E_2^{low}$ follows that of the lattice vibration of A_1 symmetry character, see the center graph of figure 3.9(b). The behavior of the symmetry forbidden $E_1(LO)$ lattice vibration upon sample rotation, which is shown in the lower graph of figure 3.9(b), was already discussed above.

The misalignment of the polarizer and the half-wave plate ($\lambda/2$) was estimated by curve fitting the trigonometric model functions to the data points. This yields a tilt angle of less than 7°. Further, the ratios of the curve fitting parameters a, b, c, and d give the relative values of the Raman tensor elements for wurtzite ZnO, summarized in table 3.4. The phase difference χ between the Raman tensor elements a and b of the $A_1(TO)$ symmetry type lattice vibration were obtained to about 93° and 104° for parallel and perpendicularly aligned incident and scattered polarization vectors, respectively. It was shown by Strach *et al.* that the choice of the parameters a, b, and the phase χ is not unique for perpendicularly oriented polarization vectors of the incident and scattered radiation [81]. Thus, the ratios for crossed polarization vectors given in table 3.4 are not well defined. Nevertheless, they are in good agreement with the values estimated by fitting the scattered intensities upon rotation for parallel aligned polarization vectors. Further it should be noted that the relative values of the Raman tensor elements for the two different polarization configurations in table 3.4 are close to each other but not within their standard errors. This might be caused by the simplified assumption of a linear background.

As depicted in figure 3.10, the peak area of the prominent features of the c-plane oriented ZnO specimen is independent on sample rotation about the z axis. This

orientation	tensor element		parallel polarization	crossed polarization
a-plane	$A_1(TO)$	$|a/d|$	0.611 ± 0.006	0.585 ± 0.022
	$A_1(TO)$	$|b/d|$	0.599 ± 0.005	0.413 ± 0.039
	$E_1(TO)$	$|c/d|$	0.424 ± 0.004	0.404 ± 0.001
	E_2^{high}	$|d/d|$	1.000 ± 0.002	1.000 ± 0.004
c-plane	$A_1(LO)$	$|a/d|$	0.121 ± 0.001	–
	E_2^{high}	$|d/d|$	1.000 ± 0.002	–

Table 3.4: Ratio of the Raman tensor elements estimated from the parameters of fits to the scattered intensity of Raman-active ZnO phonons upon sample rotation for two specific polarization configurations, i.e., for parallel and perpendicularly aligned incident and scattered polarization vectors (see reference 36). All tensor elements are normalized to that of the E_2^{high} mode.

is in excellent agreement with the model functions listed in the table 3.3. A small contribution of the symmetry forbidden phonon of $A_1(LO)$ character is observed in the Raman spectra for perpendicularly oriented incident and scattered polarization vectors caused by the misalignment of the polarizer and half-wave plate ($\lambda/2$). The corresponding signal intensities upon rotation are included in figure 3.10(b). The intensity dependence of the difference process $E_2^{high}-E_2^{low}$ follows that of the lattice vibration of A_1 symmetry character like in the case of the a-plane oriented ZnO sample. The relative values of the Raman tensor elements of the c-plane oriented ZnO sample can be estimated by simply taking the square root of the mean values of the fitted peak areas and dividing the appropriate parameters obtained. These results are also listed in table 3.4. It should be mentioned that the ratios of $|a/d|$ for the longitudinal and transverse optical lattice vibrations of A_1 symmetry type differ by a factor of about 0.6, which may be caused by their difference in bond polarity.

Concluding remarks

Raman spectra of ZnO crystallizing in a wurtzite structure exhibit at most six different signals corresponding to one-phonon Raman scattering-processes. Higher-order scattering-processes reveal a rich structure but are less intense. By analyzing the dependence of the scattered Raman intensities on sample rotation, the symmetry characters of the phonons have been verified and the ratios of the Raman tensor elements in ZnO were determined. All ZnO Raman spectra investigated in this chapter did not reveal any impact with regard to perturbations of the perfect crystal lattice. The experimental findings are consistent with the laws of conservation as well as the Raman activity and the symmetry selection-rules established for an ideal hexagonal crystal structure. This holds true, even though the samples possess defects in reality such as intrinsic point defects or extrinsic impurities. Therefore, Raman spectroscopy is not sensitive to such kinds of defects at the concentration level present in the ZnO samples

studied and in the frequency range considered here in experiment. Nonetheless, it must be noted in this context that defect related modes have been observed in undoped ZnO above the optic bands of ZnO [82].

4 Lattice dynamics of nitrogen doped ZnO − probing the origin of additional Raman modes

Nitrogen was naturally believed to be the best candidate for a shallow acceptor dopant in the II-VI semiconductor ZnO since it possesses a similar ionic radius as oxygen and since it was successfully used to p-type dope ZnS and ZnSe [30–32]. Starting with the work of Minegishi *et al.*, several reports demonstrated p-type conductivity in nitrogen doped ZnO [83]. Nevertheless, none of the approaches using nitrogen (or any other possible dopant) achieved stable, reproducible, and homogenous p-type conductivity yet to overcome the doping asymmetry in ZnO. Convincing evidence is given by theory and experimental investigations using electron paramagnetic resonance spectroscopy (EPR) and photo-EPR that isolated N_O is a deep acceptor approximately $1.4\,\text{eV}$ above the valence band edge and thus not accounting for the hole densities observed [84].

Not only the transport properties of nitrogen doped ZnO but also its lattice dynamics have been extensively investigated in the past, since these reveal unusual characteristics: Raman spectra of nitrogen doped ZnO specimens exhibit five additional nitrogen-related modes that are directly observable at N concentrations as low as 10^{18} atoms/cm^3 and increase in intensity with rising N content in ZnO samples [11, 14, 16, 85]. Various origins for the N-related signals have been controversially discussed in the literature: localized modes, disorder activated scattering, vibrating N-related complexes, or the Raman activity of silent ZnO phonons [11–19]. In this chapter, the characteristics of these additional nitrogen-related signals are analyzed and reviewed with respect to the considerations in chapter 1.3 about perturbations of the ideal crystal structure and their impacts on Raman spectra. The first section compares Raman spectra of nitrogen doped ZnO samples grown by various techniques and with different crystal orientations. It is followed by a discussion of the interpretations proposed in literature for the appearance of the additional modes upon nitrogen doping of ZnO. In the third part, the Raman-active ZnO phonons and the nitrogen-related modes are analyzed with respect to the amount of nitrogen incorporated in ZnO as well as their behavior upon hydrostatic pressure applied and sample rotation about different crystal axes. The latter yields the symmetry properties of the additional modes. The findings indicate that the nitrogen-related modes might originate from Raman-forbidden ZnO phonons or from clusters containing N atoms/ions embedded in ZnO. The chapter is brought to an end by discussing the possible formation of Zn_3N_2-like clusters or nanoinclusions,

which may cause the nitrogen-related modes, and their relevance for doping, since the formation of such inclusions would limit the solubility of nitrogen in ZnO.

Sample characteristics

The ZnO and nitrogen doped ZnO thin films analyzed in this chapter have been grown by three different methods, i.e., sputtering, chemical vapor deposition (CVD), and molecular beam epitaxy (MBE), on various ZnO substrates with different crystal orientation. Details about the growth processes can be found in references 86, 87, and 88, respectively. For comparison, commercially available pure ZnO crystals from CrysTec GmbH and Tokyo Denpa Co., Ltd. (TEW) grown by a hydrothermal method have been investigated as well [68, 69]. The nitrogen concentration in the doped samples ranges from 10^{19} up to 10^{21} atoms/cm^3, determined by secondary ion mass spectroscopy (SIMS). Zinc nitride (Zn_3N_2, CAS: 1313-49-1) specimens were provided by Alfa Aesar GmbH & Co KG in powder form with purity of 99% [89].

4.1 Nitrogen-related modes in doped ZnO

Raman spectra of nitrogen doped ZnO reveal modes at about 277, 511, 583, 645, and 860 cm^{-1} (grey shaded areas) in addition to the allowed Raman-active ZnO phonons (black, dashed lines) as depicted in figure 4.1. The additional modes are independent of the growth technique and crystal orientation. A closer examination of the Raman spectra of the various specimens reveals slight variations in the phonon frequency of the additional modes as well as of the Raman-active ZnO lattice vibrations. This is particularly observed for samples differing in the applied growth technique. The thin films or crystals may not possess fully relaxed crystal lattice structures depending on the growth process, substrates, and amount of nitrogen incorporated in ZnO, which may affect the lattice vibrations [90, 91]. For example, changes in interatomic distances may lead to shifts in the observed phonon frequencies of a few wave numbers, similar to those shifts present in the various Raman spectra depicted in figure 3.5 and 4.1. Despite of such small discrepancies, the Raman spectra of all N doped ZnO specimens appear similar and exhibit five additional modes. Comparing the Raman spectra of an undoped and nitrogen doped ZnO specimen shown in figure 4.2 in detail, it is evident that the five additional features can neither be assigned to any first- (black, dashed lines) nor higher-order (black, solid lines) Raman scattering-processes of an ideal wurtzite ZnO crystal, see also tables 3.1 and 3.2. Hence, the additional features are nitrogen-related modes (NMs).
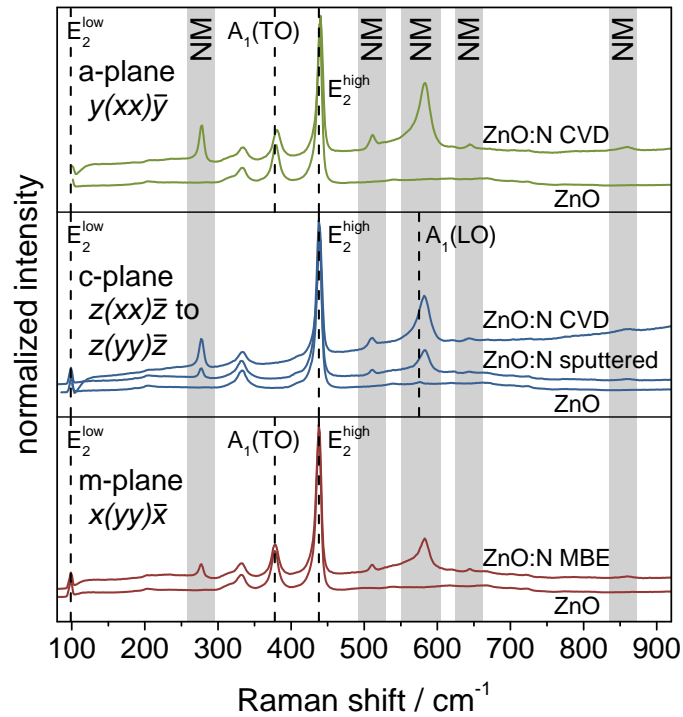
Figure 4.1: Comparison of normalized Raman spectra of ZnO and nitrogen doped ZnO samples grown by different techniques. The spectra were recorded at room temperature using a linearly polarized 532 nm laser for excitation. Black, dashed lines indicate allowed Raman-active ZnO phonons and grey, shaded areas nitrogen-related signals. For clarity, the spectra have been shifted on the axis of ordinates.
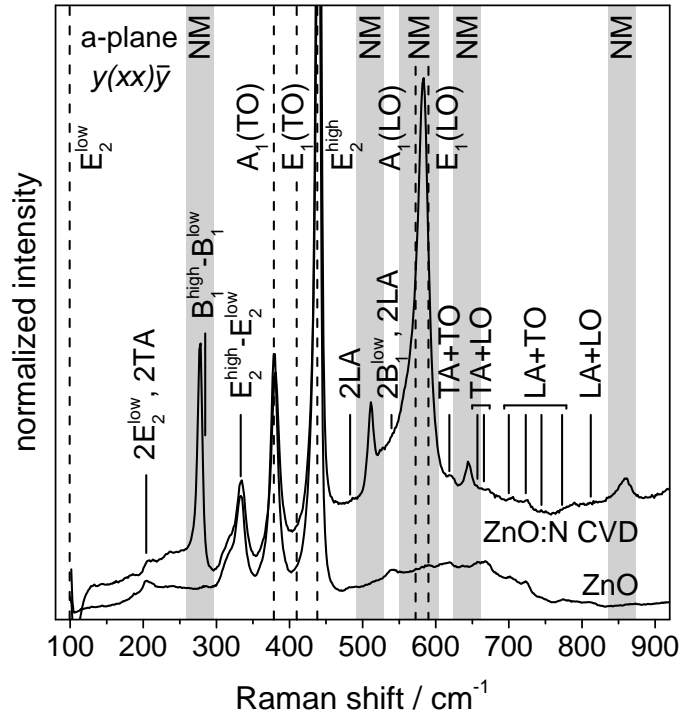
Figure 4.2: Comparison of normalized Raman spectra of ZnO and nitrogen doped ZnO grown by CVD. The Raman spectra were recorded at room temperature using a linearly polarized 532 nm laser for excitation. Grey, shaded areas indicate nitrogen-related signals that can neither be assigned to any first- (black, dashed lines) nor higher-order (black, solid lines) Raman scattering-process of an ideal wurtzite ZnO crystal. The assignment of the spectral features follows the work by Cuscó *et al.* [77].

4.2 Interpretations of the origin of the nitrogen-related modes

Before analyzing the characteristics of the N-related modes in detail, selected interpretations proposed in literature for the appearance of these additional modes upon nitrogen doping of ZnO are briefly reviewed (see also reference 92), such as local vibrations of a single N atom on anion site (N_O), vibrating complexes or intrinsic host lattice defects, or the activation of silent ZnO phonons.

The first report of five additional signals at about 274, 508, 581, 642, and $857\,cm^{-1}$ in Raman spectra of nitrogen doped ZnO dates back to an analysis of the properties of metal-organic chemical vapor deposition (MOCVD) grown ZnO and N doped ZnO films by Wang *et al.* from 2001 [12]. Due to its frequency, Wang and coworkers attributed the additional mode at about $581\,cm^{-1}$ to the $A_1(LO)$ symmetry type phonon of wurtzite ZnO, usually found at about $575\,cm^{-1}$. They suggested that it is increased in intensity due to a decrease of the carrier concentration in the N doped sample in comparison to the pure ZnO one. For the remaining additional modes no explanation was given but proposed that these are related to the nitrogen doping since they were not present in the undoped ZnO film. The assignment of the signal at about $581\,cm^{-1}$ to the $A_1(LO)$ mode of wurtzite ZnO is shared by several authors. However, it is assumed to be caused by host lattice defects [93] or to originate from resonantly enhanced longitudinal optical phonons [94].

In 2002, Kaschner *et al.* published a comprehensive Raman study of additional modes in CVD grown ZnO containing different nitrogen concentrations [11]. They observed similar additional signals in the Raman spectra like Wang *et al.* with frequencies of about 275, 510, 582, 643, and $856\,cm^{-1}$. All five modes appeared already for N concentrations as low as 10^{18} atoms/cm^3 and scaled linearly with the nitrogen content incorporated in ZnO. Kaschner *et al.* suggested to use the additional modes as a quantitative measure of nitrogen in ZnO and interpreted these in terms of nitrogen-related local vibrational modes.

The local vibration of a single N atom on anion site (N_O), however, does not explain all experimentally observed signals. In a crystal with a hexagonal lattice structure at most two different vibrational frequencies, one vibration parallel to the c axis and one in the plane perpendicular to it, are expected for the local vibration of a single N atom substituting an oxygen lattice site (N_O). Consequently, such a vibration cannot account for five additional signals found in the experiment. Furthermore, no shifts in frequency have been observed for the signals at 277, 512, and $582\,cm^{-1}$ in ZnO upon ^{14}N or ^{15}N implantation, suggesting that nitrogen motion is not involved in these three vibrations [17]. The linear-chain model illustrated in chapter 1.3 as well as density functional theory (DFT) calculations for N doped ZnO further support these findings. Due to the smaller mass of the nitrogen atom compared to the oxygen one, the localized nitrogen vibration should give rise to a mode at about $608\,cm^{-1}$ according to the linear-chain model. Advanced DFT calculations yield two nitrogen like vibrations at

about 600 and 610 cm^{-1} [95]. Both computations result in phonon frequencies of the localized nitrogen mode above the optic bands of the ZnO host. It has to be mentioned that DFT calculations for phonon frequencies may be misjudged by 10 to 20 cm^{-1} and can be tampered by supercell artifacts. Nonetheless, the results indicate that only the high-frequency N-related modes at about 645 or 860 cm^{-1} may originate from localized N vibrations on an oxygen lattice site. Unfortunately, these modes have not been addressed in the isotope study by Artús *et al.* in reference 17.

Various complexes have been considered to be the origin of the N-related modes in ZnO: the low-frequency signal at about 275 cm^{-1} was attributed to the vibration of Zn atoms surrounded to some extend by N atoms substituting O lattice sites by Wang *et al.* [15]. This was adapted from local phonon density of states calculations for various lattice defects. Yet, no experimental evidence has been given for such a locally vibrating zinc atom. Alternatively, Friedrich *et al.* suggested Zn$_i$-N$_O$ and Zn$_i$-O$_i$ complexes to cause the modes at about 274 and 510 cm^{-1} on the basis of a zinc isotope study and *ab initio* calculations [18]. However, those authors neither addressed the origin of the other N-related modes nor the corresponding likelihood of formation for such complexes. It is worth noting that numerous complexes exhibit vibrational frequencies above the optic bands of the ZnO host and thus are not related to the additional modes observed in N doped ZnO. For example, first principal calculations for substitutional diatomic molecules, like NO, NC, CO, N$_2$, and O$_2$, on an oxygen lattice site in ZnO yield stretch frequencies between 960 and 2100 cm^{-1} [96]. These frequencies are close to those of the corresponding free molecules. Further examples are modes at about 974, 1511, and 2240 cm^{-1} observed in the Raman spectra of MOCVD grown ZnO doped with N, which may be attributed to NNO, NO, and CN complexes [97], respectively, as well as several features near 2300 cm^{-1} reported in ZnO:N films grown by CVD, which may originate from complexes involving nitrogen and hydrogen [85]. Finally, an infrared absorption peak at about 3152 cm^{-1} observed in ZnO grown by chemical vapor transport in an ammonia ambient was attributed to the bond stretching mode of a N$_O$-H complex [98, 99]. The assignment was based on an analysis of the signal shifts in frequency due to different nitrogen and hydrogen isotopes. These experimental and theoretical findings suggest that neither the local vibration of a single N atom on anion site nor the vibration of one (diatomic) complex alone can explain all additional nitrogen-related modes observed in experiment.

Bundesmann *et al.* analyzed polarized Raman spectra of pulsed laser deposition (PLD) grown ZnO films doped with various elements other than nitrogen such as Al, Fe, Ga, Li, and Sb [13]. In the Raman spectra of the Al, Fe, and Sb doped films grown under an O$_2$ atmosphere as well as in a Ga doped film intentionally grown in an atmosphere containing nitrogen (N$_2$O) four additional modes were found at about 277, 511, 583, and 644 cm^{-1}. These modes are comparable in frequency with the so far called nitrogen-related modes. Only one additional mode at about 277 cm^{-1} occurred in the Ga doped specimen that was grown under pure O$_2$ atmosphere and surprisingly none was found in the spectra of Li doped ZnO specimens deposited from a target containing nitrogen (Li$_3$N). Since

the frequency range was limited to $760\,\mathrm{cm}^{-1}$ in experiment, the fifth nitrogen-related mode at about $860\,\mathrm{cm}^{-1}$ was not investigated. The N content in all samples was tested using a Rutherford backscattering (RBS) experiment with a detection limit of 2-3 at. %. No evidences for nitrogen were found in any sample. From these findings, Bundesmann *et al.* questioned the relation proposed by Kaschner and coworkers between the additional modes and nitrogen incorporated in ZnO. Rather, they concluded that the modes at 277, 511, 583, and $644\,\mathrm{cm}^{-1}$ are related to various specific dopants and, therefore, originate from intrinsic host lattice defects. In contrast to the observations by Bundesmann *et al.*, no additional modes, except an enhanced $A_1(LO)$ phonon, were found by several groups in ZnO grown by different techniques and implanted with various dopants like: Ga by Reuss *et al.* [14]; Ga, O, or Si by Yu *et al.* [16]; O, P, or Zn by Artús *et al.* [17]; Ar, Co, Fe, Mn, Ni, or V by Schumm *et al.* [92, 100]. On the other hand, these groups observed additional modes in the Raman spectra of ZnO samples implanted with N. These discrepancies may be clarified by considering that the detection limit of the RBS technique is above the concentration of 10^{18} nitrogen atoms/cm^3 for which the additional modes have already been observed in doped ZnO [11, 16]. Therefore, it may be possible that the samples analyzed by Bundesmann *et al.* were unintentionally doped with nitrogen during the preparation or growth process, leading to the appearance of the additional modes in the Raman spectra [16].

It must be noted that various authors besides Bundesmann *et al.* reported on additional features in Raman spectra of ZnO specimens, which were grown explicitly without nitrogen. For example, Liu *et al.* observed additional modes at about 276, 510, 582, and $643\,\mathrm{cm}^{-1}$ in sputtered ZnO doped with phosphorus [101]. Furthermore, some groups found one additional mode in Raman spectra of undoped or doped ZnO similar to the nitrogen-related signal at about $275\,\mathrm{cm}^{-1}$ [102–104].

Another explanation of the origin of the additional signals was given by Manjón and coworkers [19]: by comparing various experimental results with *ab initio* calculations of the lattice dynamics of ZnO, they attributed the two strongest additional signals at 277 and $583\,\mathrm{cm}^{-1}$ to silent B_1^{low} and B_1^{high} ZnO phonons and the remaining features to second-order scattering-processes, i.e., signals at about 511, 645, and $860\,\mathrm{cm}^{-1}$ were assigned to $2B_1^{\mathrm{low}}$, $B_1^{\mathrm{high}}+TA$, and $B_1^{\mathrm{low}}+B_1^{\mathrm{high}}$ processes, respectively. Manjón *et al.* argued that Raman scattering of silent modes is induced by the breakdown of the translational symmetry of the lattice caused by defects or impurities, thus, caused by disorder activated Raman scattering (DARS). Group theoretical considerations agree with such an approach, as it was shown in chapter 1.3. A N_O point defect in wurtzite ZnO breaks the perfect translational symmetry of the crystal, i.e., the local site symmetry C_{3v} of zinc or oxygen lattice sites is lower than that of the point group C_{6v} of the ideal ZnO crystal. If the perturbation is strong enough, the symmetry character of a vibrational mode will be affected, which in turn may change its Raman activity. Carrying out the expansion of the irreducible representations of the modes in terms of representations of the point group characterizing the defect site shows that the silent B_1 modes in the point group C_{6v} indeed are transformed into

Raman-active modes of A_1 symmetry character in the C_{3v} point group, as depicted in table 1.2. Thus, the explanation by Manjón *et al.* seems consistent, as the calculated values given in reference 73 of 261 and $552\,\mathrm{cm}^{-1}$ as well as the experimental values obtained by inelastic neutron scattering of 259 and $552\,\mathrm{cm}^{-1}$ in reference 72 for the two silent B_1 modes are somewhat close to the experimental values of the additional modes observed in Raman spectra of N doped ZnO.

4.3 Characteristics of the nitrogen-related modes

The preceding section briefly summarized the divergent attempts to explain the appearance of the additional modes in Raman spectra of N doped ZnO. In order to analyze the influence of nitrogen doping on the lattice dynamics of ZnO and to more closely examine the characteristics of the additional modes, a series of CVD grown samples containing different N concentrations and crystal orientations (a-/c-plane) are investigated in the following paragraphs. The Raman-active ZnO lattice vibrations and the nitrogen-related modes are discussed with respect to the amount of nitrogen incorporated in ZnO as well as their behavior upon hydrostatic pressure applied in comparison to *ab initio* calculations and upon sample rotation about a crystal axis. The latter yields the symmetry properties of the additional modes. The findings shed new light on the origin of the additional modes, in particular questioning whether the assignment to silent B modes of wurtzite ZnO is valid at all.

Dependence on the amount of nitrogen incorporated

Figure 4.3(a) displays Raman spectra of a-plane oriented ZnO with nitrogen concentrations in the range of 10^{19} up to 10^{21} atoms/cm^3 recorded at room temperature using a linearly polarized $532\,\mathrm{nm}$ laser for excitation. The samples have been aligned such that the intensity of the $\mathrm{E}_2^{\mathrm{high}}$ phonon is maximal and, thus, the one of $\mathrm{E}_1(\mathrm{TO})$ symmetry type is minimal. To obtain comparable spectra a individual piecewise linear background was subtracted from each Raman spectrum, exemplary shown in figure 4.3(a) for the sample containing about 8.77×10^{20} nitrogen atoms/cm^3. As a measure of scattered intensity, the signals were fitted with a Lorentzian line-shape to determine their peak areas, which are given as a function of N content in figure 4.3(b). This procedure is not optimal since the background reveals a much more complex form, however, the method is sufficient to demonstrate the dependence of the intensity of the lattice vibrations on the amount of nitrogen incorporated (see also chapter 2). Consistent with previous reports, the additional modes increase in intensity with rising nitrogen content in the ZnO specimens [11, 14, 16, 85]. Kaschner *et al.* even observed a linear dependence on the nitrogen concentration in doped ZnO in the range of 10^{18} up 10^{19} defect atoms/cm^3 [11]. This finding agrees well with the dependences found in figure 4.3(b), however, at a concentration of about 10^{21} nitrogen atoms/cm^3 the scattered intensity abruptly decreases. The collapse in
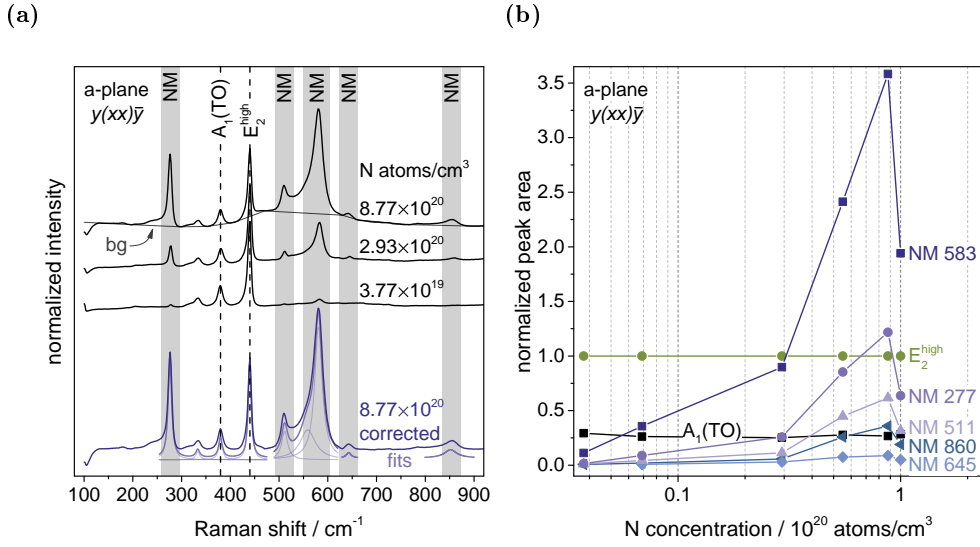
(a)

(b)

Figure 4.3: Analysis of a-plane oriented N doped ZnO: (a) Normalized Raman spectra recorded at room temperature using a linearly polarized 532 nm laser for excitation. Black, dashed lines indicate Raman-active ZnO phonons and grey, shaded areas nitrogen-related signals. For clarity, the spectra have been shifted on the axis of ordinates. Signals in the spectra were fitted with a Lorentzian lineshape after subtracting a piecewise linear background (bg), exemplary shown for the specimen containing about 8.77×10^{20} N atoms/cm^3. (b) Signal peak area normalized to that of the E_2^{high} phonon as a function of N content. Solid lines are guides to the eye.

rising intensity may indicate that the solubility limit of nitrogen is exceeded leading to a different incorporation of the dopant in ZnO such that it does not contribute to Raman scattering anymore. A damaged sample, e.g., having an inhomogeneous nitrogen distribution, may also be the cause for the nonlinear behavior. Further experiments are required to clarify the reason for the decrease in scattered intensity. In addition to the five nitrogen-related modes, the Raman spectra exhibit a high-frequency signal at about $3152\,\text{cm}^{-1}$ which is assigned to the bond stretching mode of a N_O-H complex [98, 99]. It also scales in intensity with the nitrogen amount incorporated in ZnO (not shown here). In contrast, the intensity of the Raman-active ZnO phonon of $A_1(\text{TO})$ symmetry character remains constant upon nitrogen doping.

The analysis of the distinct features in the Raman spectra is shown in detail in figure 4.4. With the exception of the signal at about $511\,\text{cm}^{-1}$, all additional modes decrease in frequency with rising nitrogen content and the full width at half maximum (FWHM) increases. For example, the N-related mode at $277\,\text{cm}^{-1}$ shifts about $1.5\,\text{cm}^{-1}$ across the entire investigated nitrogen range. On the other hand, the Raman-active ZnO lattice vibrations are neither significantly altered in frequency nor line shape.

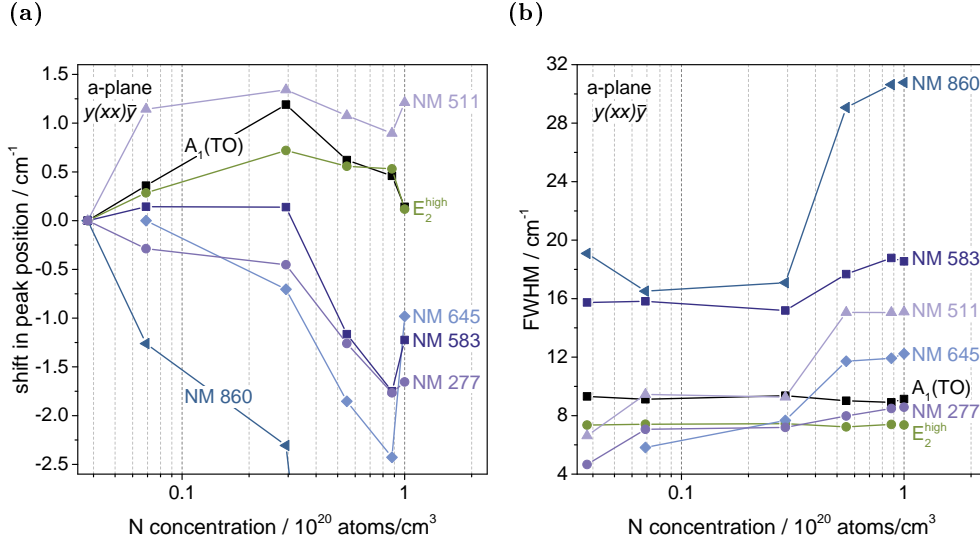The findings for the c-plane oriented ZnO specimens are given in figure 4.5.

(a)   **(b)**

Figure 4.4: Analysis of a-plane oriented N doped ZnO: (a) Shift in signal frequency with respect to the specimen containing the lowest amount of nitrogen and (b) signal full width at half maximum (FWHM) as a function of N content. Solid lines are guides to the eye.

It seems that the scattered intensity or rather the peak area increases upon nitrogen doping, reflecting the trend observed for the a-plane oriented crystals, whereas the decrease in phonon frequency is not confirmed. However, a detailed analysis is not possible due to the small number of three samples.

The trends shown in figures 4.3(b) and 4.5(a) upon doping confirm that the additional modes are somewhat related to nitrogen. On the other hand, the Raman-active ZnO lattice vibrations are not affected by the doping process. This can be interpreted as evidence that the nitrogen doped ZnO samples still possess a high crystal quality, i.e., the translational symmetry is not strongly perturbed by the dopant.

Dependence on hydrostatic pressure – determination of pressure coefficients

Figure 4.6(a) depicts four representative Raman spectra of an a-plane oriented ZnO specimen containing about 5.5×10^{20} nitrogen atoms/cm^3 at different hydrostatic pressures of about 0.2, 2.2, 4.5, and 6.5 GPa. The spectra were recorded in backscattering geometry at room temperature using a linearly polarized 532 nm laser for excitation while the sample was placed inside a diamond anvil cell (experimental details see chapter 2). No particular polarization orientation was selected for the scattered radiation in experiment, thus all polarization orientations of the scattered radiation are analyzed simultaneously. The Raman-active ZnO phonons of $A_1(TO)$, $E_1(TO)$, and E_2^{high} symmetry type
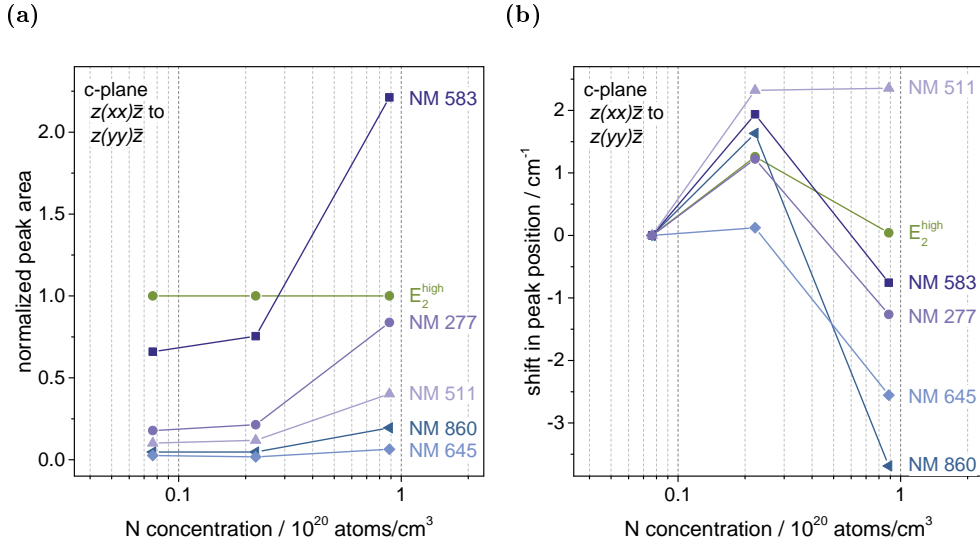
Figure 4.5: Analysis of c-plane oriented N doped ZnO: (a) Signal peak area normalized to that of the E_2^{high} phonon and (b) shift in signal frequency with respect to the specimen containing the lowest amount of nitrogen as a function of N content. Solid lines are guides to the eye.

as well as four out of five N-related modes are observed in the Raman spectra across the entire pressure range, i.e., from ambient pressure up to 6.5 GPa. Due to its weak intensity, the nitrogen-related mode at about 860 cm^{-1} is only investigated up to an applied hydrostatic pressure of 0.9 GPa. The second-order scattering-processes $2E_2^{low}$ and $E_2^{high}-E_2^{low}$ at 204 and 331 cm^{-1} (at 0.2 GPa) are present in all Raman spectra upon pressure as well as a signal at about 548 cm^{-1} (at 0.2 GPa). The latter is close in frequency to the mode that Cuscó *et al.* assigned to the combination mode $2B_1^{low}$ and LA overtones [77]. In the following, the signal is preliminary attributed to the $2B_1^{low}$ scattering process. The origin of the broad feature in the Raman spectra at about 882 cm^{-1} (at 0.2 GPa) is unknown. As previously discussed, the E_2^{low} mode is not accessible due to experimental limitations and the remaining first-order Raman-active scattering-processes of $A_1(LO)$ and $E_1(LO)$ symmetry character are not allowed in the backscattering configuration parallel to the y axis, i.e., for an a-plane crystal orientation.

The peak positions of the prominent features were determined by subtracting a piecewise linear background from each of the spectra and subsequently fitting every signal using a Lorentzian line-shape, exemplarily shown in the lower part of figure 4.6(a) for the spectra recorded at a pressure of about 0.2 GPa. For simplicity, the E_2^{high} mode was also described by a Lorentzian and not by a Fano line-shape. To improve the procedure, several unidentified features in the spectra were fitted as well if needed, e.g., signals at about 242, 319, 461, and 882 cm^{-1} in the Raman spectra at a pressure of 0.2 GPa. Figure 4.6(b) depicts the peak positions as a function of pressure. The determined standard errors
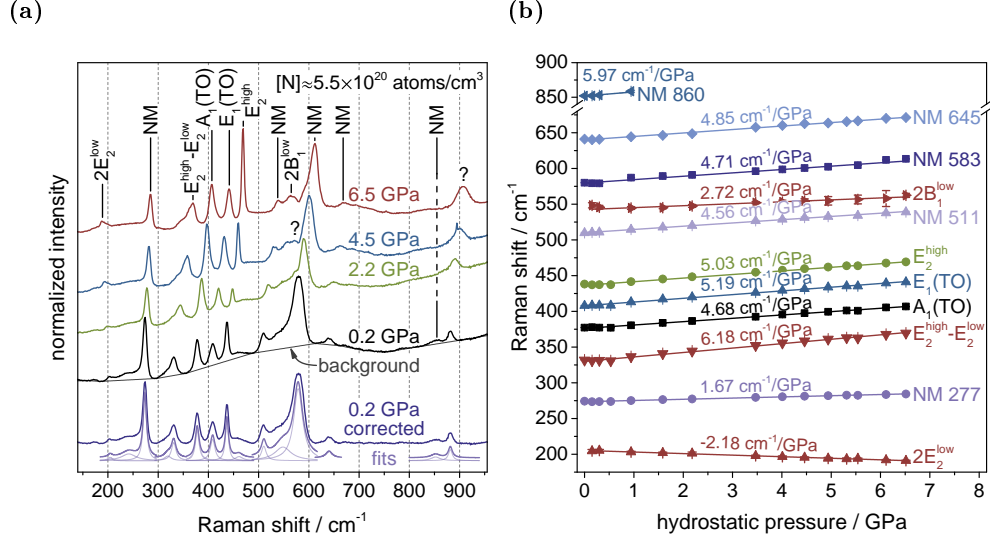
(a) **(b)**

Figure 4.6: (a) Representative Raman spectra of an a-plane oriented N doped ZnO sample containing about 5.5×10^{20} nitrogen atoms/cm^3 at different hydrostatic pressures. The assignment of the modes follows the work by Cuscó *et al.* [77]. Question marks "?" denote signals of unknown origin. The corresponding peak positions were determined by fitting each signal with a Lorentzian lineshape after subtracting a piecewise linear background, exemplary shown for the spectrum at a pressure of 0.2 GPa. (b) Determined peak positions as a function of applied hydrostatic pressure. Solid lines are fits to the data points weighted by the standard errors of the peak potions (y error).

of the peak positions are given as error bars in figure 4.6(b) and yield a mean value of $0.7\,\text{cm}^{-1}$, which is much smaller than the system's spectral resolution of $5.1\,\text{cm}^{-1}$. Surprisingly, some modes reveal an unusual behavior for small applied pressures, e.g., the E_2^{high} mode with a frequency of about $437.9\,\text{cm}^{-1}$ at ambient pressure should exhibit a positive shift upon increasing pressure; however, its value is slightly downshifted to $436.9\,\text{cm}^{-1}$ at a pressure of 0.2 GPa. All phonons then show the expected behavior above 0.5 GPa.

To determine the zero-pressure frequency ω_0 and the hydrostatic pressure coefficient $\partial\omega/\partial P$ of a signal, the corresponding data points in figure 4.6(b) were fitted with a linear function (solid lines) weighted by the standard errors of the peak positions. Table 4.1 summarizes the results of such fits using different constraints: (i) using all data points ($\lambda_0 = 693.95\,\text{nm}$), (ii) neglecting the data points at 0.2, 0.3, and 0.5 GPa ($\lambda_0 = 693.95\,\text{nm}$), i.e., the data points for which some modes exhibited an unusual shift upon pressure, and (iii) using the λ_0 value of 694.24 nm from reference 67 for calculating the applied pressure and neglecting negative pressure values. Depending on these constraints, the zero-pressure frequencies and hydrostatic pressure coefficients differ slightly from each other but are still in reasonable agreement. In the following, the values calculated based on the λ_0 value of 693.95 nm and using all data points (method (i)) are

mode	$\omega_0/\mathrm{cm}^{-1}$			$(\partial\omega/\partial P)/(\mathrm{cm}^{-1}/\mathrm{GPa})$		
	(i)	(ii)	(iii)	(i)	(ii)	(iii)
$A_1(\mathrm{TO})$	376	376	380	4.68 ± 0.09	4.63 ± 0.08	4.74 ± 0.11
$E_1(\mathrm{TO})$	408	409	413	5.19 ± 0.11	4.95 ± 0.09	5.07 ± 0.16
E_2^{high}	436	437	441	5.03 ± 0.06	4.88 ± 0.06	4.94 ± 0.08
$2E_2^{\mathrm{low}}$	205	205	203	-2.18 ± 0.06	-2.16 ± 0.07	-2.17 ± 0.07
$E_2^{\mathrm{high}} - E_2^{\mathrm{low}}$	330	332	335	6.18 ± 0.12	5.88 ± 0.10	6.14 ± 0.19
$2B_1^{\mathrm{low}}$	542	541	543	2.72 ± 0.30	3.17 ± 0.16	3.18 ± 0.16
NM 277	274	274	275	1.67 ± 0.04	1.58 ± 0.03	1.70 ± 0.04
NM 511	510	510	513	4.56 ± 0.08	4.50 ± 0.08	4.71 ± 0.22
NM 583	580	580	583	4.71 ± 0.22	4.52 ± 0.24	4.73 ± 0.32
NM 645	640	640	642	4.85 ± 0.09	4.75 ± 0.11	5.30 ± 0.13
NM 860	852	-	-	5.97 ± 1.62	-	-

Table 4.1: Zero-pressure frequencies and hydrostatic pressure coefficients of Raman-active ZnO lattice vibrations and nitrogen-related modes in N doped ZnO. The values were determined from linear fits to the data points in figure 4.6(b) using different constraints: (i) using all data points ($\lambda_0 = 693.95\,\mathrm{nm}$), (ii) neglecting the data points at 0.2, 0.3, and 0.5 GPa ($\lambda_0 = 693.95\,\mathrm{nm}$), and (iii) using the λ_0 value of 694.24 nm from reference 67 and neglecting negative pressure values. The standard error in ω_0 is less than 1 cm^{-1}.

discussed.

The zero-pressure frequencies ω_0 and hydrostatic pressure coefficients $\partial\omega/\partial P$ of the prominent features observed in N doped ZnO are compared to the experimentally derived findings by Reparaz *et al.* [105] and to the results of *ab intio* calculations by Serrano *et al.* for wurtzite ZnO [73] in table 4.2. With the exception of the longitudinal optical phonons, the calculated phonon frequencies of all first-order Raman scattering-processes in ZnO agree fairly well with the experimental values reported by Reparaz and coworkers. The frequencies of the LO phonons are estimated too small by theory, deviating by about 18 and 31 cm^{-1}, and are predicted in reverse order. In addition, all pressure coefficients obtained by the *ab intio* calculations are slightly overestimated, excluding the phonon of $E_1(\mathrm{LO})$ symmetry character, whose calculated coefficient is smaller than observed in experiment.

The parameters determined from the nitrogen doped ZnO specimen are given in columns six and nine of table 4.2: the pressure coefficients for the Raman-active lattice vibrations of $A_1(\mathrm{TO})$, $E_1(\mathrm{TO})$, and E_2^{high} symmetry type match the ones obtained for pure wurtzite ZnO, implying that the lattice dynamics of ZnO are not perturbed by doping the semiconductor with nitrogen. The findings for the second-order scattering-processes support this interpretation. Assuming that these processes only arise from scattered phonons from the center of the Brillouin zone (Γ-point), their corresponding pressure coefficients are simply given

assignment according to			$\omega_0/\mathrm{cm}^{-1}$			$(\partial\omega/\partial P)/(\mathrm{cm}^{-1}/\mathrm{GPa})$		
			ZnO		ZnO:N	ZnO		ZnO:N
	mode	Manjón *et al.* [19]	theory [73]	exp. [105]	exp.	theory [73]	exp. [105]	exp.
1st order scattering	E_2^{low}		91	98		-1.05	-0.78	
	B_1^{low}		261			1.50		
	$A_1(\mathrm{TO})$		391	377	376	5.29	4.91	4.68 ± 0.09
	$E_1(\mathrm{TO})$		409	411	408	5.22	5.03	5.19 ± 0.11
	E_2^{high}		440	438	436	5.58	5.04	5.03 ± 0.06
	B_1^{high}		552			4.96		
	$A_1(\mathrm{LO})$		560	578		4.77	4.56	
	$E_1(\mathrm{LO})$		556	587		4.39	4.55	
2nd		$2E_2^{low}$	182	196	205	-2.10	-1.56	-2.18 ± 0.06
		$E_2^{high}-E_2^{low}$	349	340	330	6.63	5.82	6.18 ± 0.12
		$2B_1^{low}$	522		542	3.00		2.72 ± 0.30
N-related	NM 277	B_1^{low}	261		274	1.50		1.67 ± 0.04
	NM 511	$2B_1^{low}$	522		510	3.00		4.56 ± 0.08
	NM 583	B_1^{high}	552		580	4.96		4.71 ± 0.22
	NM 645	$B_1^{high}+\mathrm{TA}$			640			4.85 ± 0.09
	NM 860	$B_1^{low}+B_1^{high}$	813		852	6.46		5.97 ± 1.62

Table 4.2: Zero-pressure frequencies and hydrostatic pressure coefficients of Raman-active ZnO lattice vibrations and nitrogen-related modes in N doped ZnO. The outcomes of *ab initio* calculations at the Γ-point (theory) and experimental findings (exp.) for wurtzite ZnO from references 73 and 105, respectively, are listed for comparison. Parameters given for the second-order scattering-processes in ZnO are based on the assumption that these only arise from scattered phonons from Γ-point and therefore are simply obtained by summing or subtracting the values of the individual first-order processes.

by summing or subtracting the values of the individual first-order processes. For example, using the coefficients determined by Reparaz *et al.* for the ZnO phonons of E_2^{low} and E_2^{high} symmetry character of -0.78 and $5.04\,cm^{-1}/GPa$, respectively, yield a shift upon pressure of $5.82\,cm^{-1}/GPa$ for the difference mode. This is in reasonable agreement with the value of $6.18\,cm^{-1}/GPa$ derived from the N doped ZnO specimen. As listed in table 4.2, the experimentally determined pressure coefficients of the second-order processes $2B_1^{low}$ and $2E_1^{low}$ also match the values obtained by such a simple analysis based on the findings for ZnO. It must be noted that the results for the signal possibly corresponding to the combination mode $2B_1^{low}$ are very sensitive to the procedure how the background is treated, whether an additional pressure-independent mode observed at about $570\,cm^{-1}$ in the Raman spectra is included in the determination of the peak positions or not (which was done here), and to the data range used for determining the zero-pressure frequency and pressure coefficient (see table 4.1). Therefore, the values derived for the signal preliminary assigned to the $2B_1^{low}$ mode have to be viewed with caution.

In the following, the nitrogen-related modes are analyzed: at first sight, their characteristics upon pressure seem to confirm the assignment to silent ZnO lattice vibrations of B_1 symmetry character proposed by Manjón *et al.*, given in column three of table 4.2. The modes at about 277 and $583\,cm^{-1}$ exhibit hydrostatic pressure coefficients of 1.67 and $4.71\,cm^{-1}/GPa$, respectively, which match the values of 1.50 and $4.96\,cm^{-1}/GPa$ computed for the silent modes of B_1^{low} and B_1^{high} symmetry character. Unfortunately, it is not possible to investigate the findings for the signal at about $645\,cm^{-1}$ with respect to a combination process of B_1^{high} symmetry character and transversal acoustic (TA) phonons because no data upon pressure is available for the TA modes. In comparison to the obtained results for the nitrogen-related mode at about $583\,cm^{-1}$, one can only draw the conclusion that the pressure coefficient for the TA modes must be very small if the assignment is correct. The shifts upon pressure determined for the nitrogen-related mode at $860\,cm^{-1}$ agrees with the values calculated for the second-order process $B_1^{low}+B_1^{high}$ by theory. However, a significant analysis is not possible due to the small number of four data points obtained in experiment. The nitrogen-related mode at $511\,cm^{-1}$ reveals a large shift upon pressure of $4.56\,cm^{-1}/GPa$ that does not coincide with the value of about $3.00\,cm^{-1}/GPa$ estimated for the combination mode $2B_1^{low}$ to which it was attributed by Manjón and coworkers. This may be owed to the fact that the calculation for the pressure coefficients of the second-order processes is based on the simplified assumption of arising only from scattered phonons from the center of the Brillouin zone. Table 4.3 lists phonon frequencies and their pressure coefficients at various high symmetry points of the Brillouin zone along the dispersion relations of the silent modes of B symmetry type taken from reference 73. Using the average of these coefficients to determine an improved shift upon pressure yields a value of $3.24\,cm^{-1}/GPa$ for the combination mode $2B_1^{low}$ that also does not coincide with the one obtained for the nitrogen-related mode at about $511\,cm^{-1}$. As discussed above, the signal at about $548\,cm^{-1}$ (at $0.2\,GPa$) exhibits a shift upon pressure which agrees much better with the one calculated for the combination

symmetry	ω/cm^{-1}		$(\partial\omega/\partial P)/(\mathrm{cm}^{-1}/\mathrm{GPa})$	
point	$\mathrm{B}_1^{\mathrm{low}}$	$\mathrm{B}_1^{\mathrm{high}}$	$\mathrm{B}_1^{\mathrm{low}}$	$\mathrm{B}_1^{\mathrm{high}}$
Γ	261	552	1.50	4.96
A	189	557	1.30	4.56
H	258	539 (514)	1.89	4.77 (5.45)
L	267	554	1.78	4.81
average	244	551 (554)	1.62	4.78 (4.95)

Table 4.3: Calculated phonon frequencies and pressure coefficients at high symmetry points of the Brillouin zone along the dispersion relation of the modes with B symmetry character at the Γ-point. Data according to reference 73.

process $2\mathrm{B}_1^{\mathrm{low}}$.

Critical reviewing the outcome of the *ab initio* calculations for the silent lattice vibrations of B symmetry character in ZnO further reveals fairly large discrepancies between the calculated phonon frequencies and that of the nitrogen-related modes, see table 4.2. This is surprising, since the Raman-active ZnO lattice vibrations are represented quite accurately by the theory with the exception of the LO phonons.

Dependence on sample rotation – symmetry characteristics

To study the symmetry characteristics of the nitrogen-related modes, CVD and MBE grown nitrogen doped ZnO specimens were rotated in distinct steps about the axis defined by the linearly polarized 532 nm excitation laser. After each rotation step, a polarized Raman spectrum was recorded in backscattering geometry at room temperature. For simplicity, the intensities or amplitudes of the prominent features in the Raman spectra have been estimated by selecting the maximal data point of the corresponding signal and correcting it for a linear background chosen individually below each one with the naked eye.

Figures 4.7 and 4.8 depict the intensities of the Raman-active ZnO lattice vibrations and the nitrogen-related modes of representative CVD grown ZnO:N specimens as a function of the rotation angle about the y (normal to the a-plane) and z axis (normal to the c-plane), respectively. In addition, the scattered intensities of Raman-active lattice vibrations of pure ZnO samples are shown. The axes refer to the right-angled coordinate system of the hexagonal structure shown in figure 3.4(a). For all four polarization configurations, the behavior of the ZnO lattice vibrations of $\mathrm{A}_1(\mathrm{TO})$ and $\mathrm{E}_1(\mathrm{TO})$ symmetry character as well as of the difference mode $\mathrm{E}_2^{\mathrm{high}}-\mathrm{E}_2^{\mathrm{low}}$ upon rotation is consistent with their symmetry characters in an ideal ZnO crystal structure. An exception is the phonon of $\mathrm{E}_2^{\mathrm{high}}$ symmetry type when the sample is rotated about the y-axis, shown

in figure 4.7. The corresponding signal does not entirely vanish upon rotation for rotation angles of $-\pi/2$ and $\pi/2$ for parallel polarization geometry or for multiplies of $\pi/2$ for perpendicular polarization geometry which is not reflected by the model functions given in table 3.3 and therefore is somewhat inconsistent with its symmetry character. The scattered intensities of the nitrogen-related modes are independent of the rotation angle, i.e., they are constant or cannot be detected. It is notable that the additional mode at about $645\,\mathrm{cm}^{-1}$ exhibits a depolarization ratio $\rho = I_\perp/I_\parallel$ about one for the a- and c-plane oriented samples, where $I_\parallel$ and $I_\perp$ are the intensities of scattered light whose polarizations are parallel or perpendicular to the polarization of the incident radiation. On the other hand, the depolarization ratios of the remaining nitrogen-related modes are less than one.

The findings upon the rotation of the sample about the x axis (normal to the m-plane) of a MBE grown nitrogen doped ZnO specimen are displayed in figure 4.9. The intensity dependence of the Raman-active ZnO lattice vibrations is the same as on the rotation of the sample about the y axis. This is consistent with their symmetry characters. The only exception to this rule is the intensity dependence of the phonon of $\mathrm{E}_2^{\mathrm{high}}$ symmetry type since its signal does not entirely vanish upon rotation. In contrast to the findings upon the rotation about the y and z axis, the nitrogen-related modes are not independent of the rotation angle at all times. In particular, four out of five additional modes reveal a specific dependence on rotation for perpendicular oriented incident and scattered polarization vectors $(x(yz)\bar{x} \leftrightarrow x(zy)\bar{x})$, see figure 4.9(b).

Assuming that due to the presence of $\mathrm{N_O}$ the local site symmetry of point group C_{3v} determines the Raman activity and also the symmetry character of extended lattice modes, the scattered intensity dependence on sample or plane of polarization rotation of formerly silent B_1 modes may be deduced. The Raman tensors for the point group C_{3v} $(3m)$ have the matrix form [40]:

$$
\begin{pmatrix} a & 0 & 0 \\ 0 & a & 0 \\ 0 & 0 & b \end{pmatrix} \quad
\begin{pmatrix} d & 0 & -e \\ 0 & -d & 0 \\ -e & 0 & 0 \end{pmatrix} \quad
\begin{pmatrix} 0 & d & 0 \\ d & 0 & e \\ 0 & e & 0 \end{pmatrix} \tag{4.1}
$$

$$
\mathrm{A}_1(z') \qquad\qquad \mathrm{E}(-x') \qquad\qquad \mathrm{E}(y')
$$

These tensors are defined with respect to three orthogonal axes x', y', and z'. The axes are specified along symmetry operations of the trigonal crystal class C_{3v}. According to Koster et $al.$, the z' axis is parallel to the threefold rotation axis and the y' axis is normal to one of the three reflection planes [61].[4] These symmetry directions correspond to the z and y axis of the hexagonal crystal class C_{6v}, respectively, as depicted in figures 3.1 and 3.4(a). The intensity dependence of the A_1 mode on rotation is the same for both crystal structures

---

[4]An alternative orientation of the coordinate axes is given in the book by Nye [106]. The corresponding Raman tensors are listed in the article by Loudon [56]. In both orientations the Raman tensor of the A_1 mode has only diagonal elements.
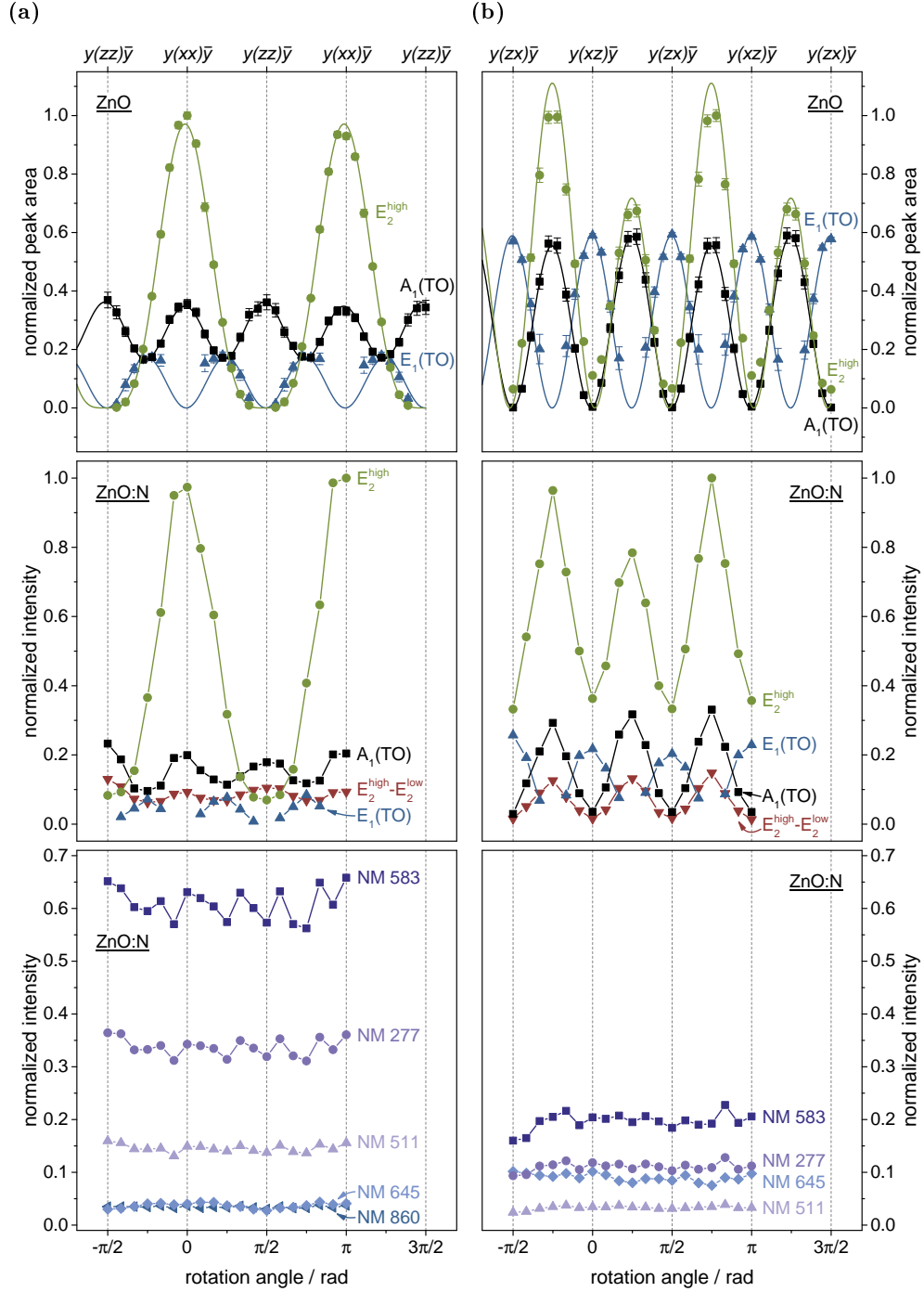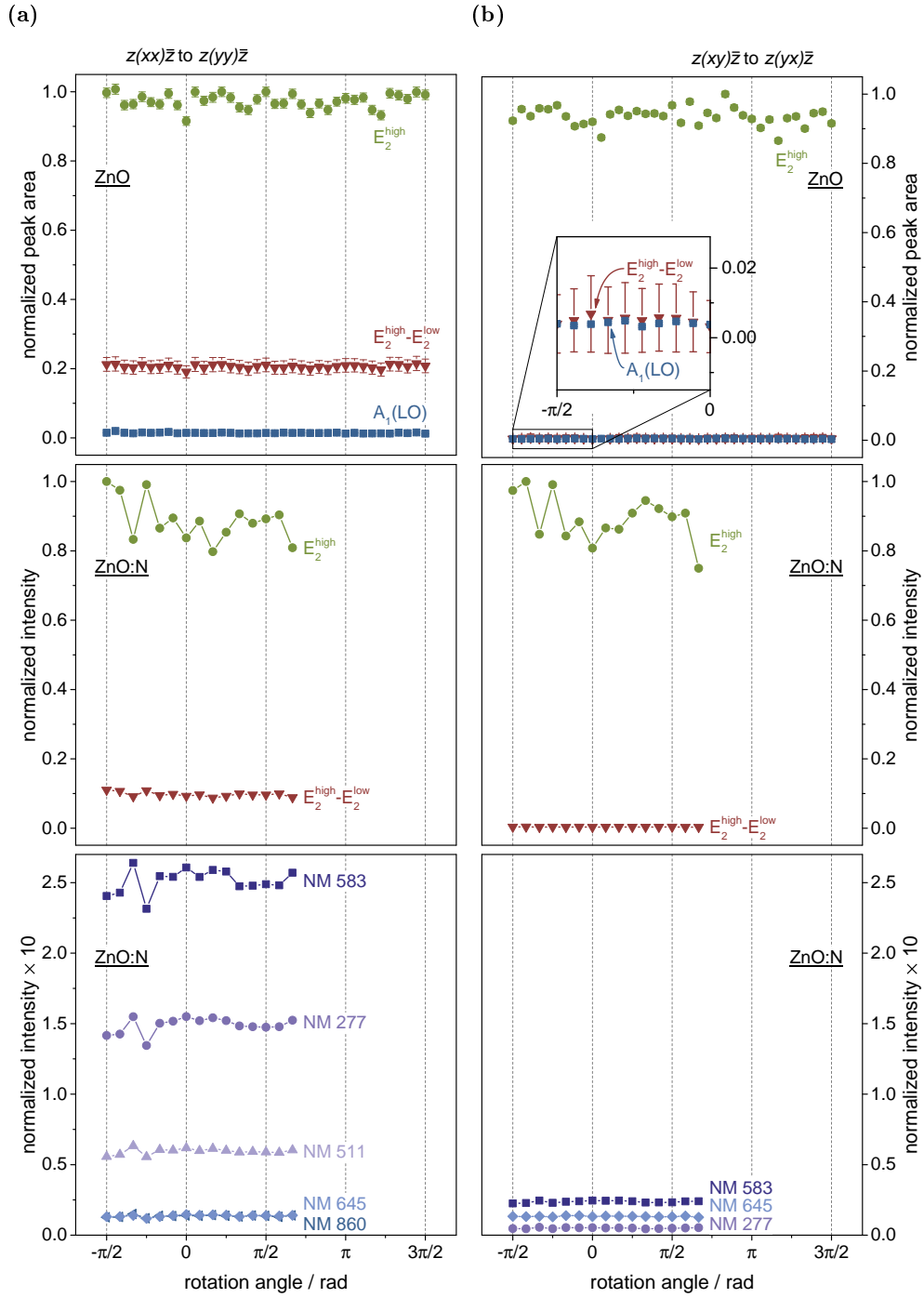
Figure 4.7: Normalized intensity of the prominent Raman signals of an a-plane oriented ZnO and N doped ZnO specimen ([N] $\approx 2.93 \times 10^{20}$ atoms/cm^3, CVD grown) versus sample rotation about the y axis for (a) parallel and (b) perpendicularly aligned incident and scattered polarization vectors. Signals are normalized to the maximum intensity of the E$_2^{high}$ phonon. Solid lines are fits to the data points in the top graph and guides to the eye in the center and bottom graphs.
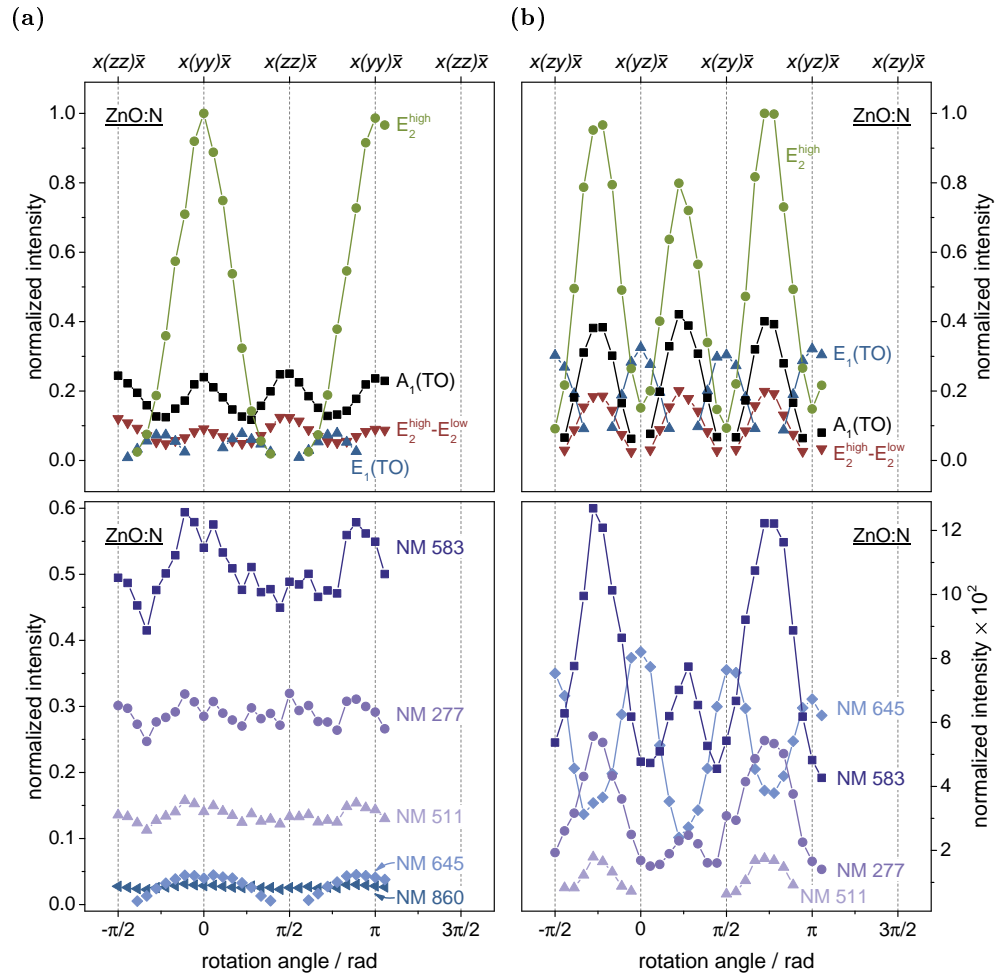
Figure 4.8: Normalized intensity of the prominent Raman signals of a c-plane oriented ZnO and N doped ZnO specimen ($[N] \approx 7.65 \times 10^{19}$ atoms/cm^3, CVD grown) versus sample rotation about the z axis for (a) parallel and (b) perpendicularly aligned incident and scattered polarization vectors. Signals are normalized to the maximum intensity of the E_2^{high} phonon. Solid lines are guides to the eye in the center and bottom graphs.

Figure 4.9: Normalized intensity of the prominent Raman signals of a m-plane oriented N doped ZnO specimen (MBE grown) versus sample rotation about the x axis for (a) parallel and (b) perpendicularly aligned incident and scattered polarization vectors. Signals are normalized to the maximum intensity of the E_2^{high} phonon. Solid lines are guides to the eye.

since the axes of the two coordinate systems (xyz) and $(x'y'z')$ are in principle in line and since the mode of A_1 symmetry character preserves its shape when reducing the symmetry from C_{6v} to C_{3v}. Thus, if the nitrogen-related modes at 277 and $583\,\mathrm{cm}^{-1}$ are assigned to silent B_1 modes, which transform into Raman-active A_1 modes due to the symmetry reduction (assuming $C_{3v}(\sigma_v)$ symmetry, see table 1.2), the intensity of the corresponding Raman signals should be given by the model functions describing the ZnO lattice vibration of A_1 symmetry type in the hexagonal crystal structure belonging to the point group C_{6v}. The same applies to the combination processes $2B_1^{\mathrm{low}}$ and $B_1^{\mathrm{low}}+B_1^{\mathrm{high}}$ attributed to the additional modes at about 511 and $860\,\mathrm{cm}^{-1}$, since the direct product $A_1 \otimes A_1$ is simply of A_1 character in C_{3v} symmetry.

The nitrogen-related modes do not exhibit the same intensity dependence on sample rotation in the experiment than the ZnO lattice vibration of A_1 symmetry character. This leads to the question whether a set of parameters a, b, and χ of the model functions describing the ZnO phonon of A_1 symmetry type exists that represents the experimental findings for the nitrogen-related modes. At first, the sample rotation about the z axis of the hexagonal structure is considered. As depicted in table 3.3, the model function describing the A_1 mode is independent of the rotation angle which matches the corresponding experimental findings for the scattered intensities of the nitrogen-related modes, shown in figure 4.8. An imperfect alignment of the polarizer and the half-wave plate ($\lambda/2$) in the setup may explain the appearance of the additional modes in the experiment when the scattered radiation is analyzed perpendicularly to that of the incident one. The same assumption is needed to describe the experimental findings for the Raman-active lattice vibrations in pure ZnO correctly, see chapter 3.3. In figure 4.7, the scattered intensities of the nitrogen-related modes are depicted as a function of the rotation angle about the y axis. No angular dependence is found. This may be surprising as the corresponding model function in general depends on the rotation angle according to table 3.3. However, it is independent of the rotation angle and represents the experimental findings for parallel oriented incident and scattered polarization vectors when setting its parameters to $a = b$ and $\chi = n\pi$ or $a = -b$ and $\chi = m\pi$ with $n \in \{0, \pm2, \pm4, ...\}$ and $m \in \{\pm1, \pm3, \pm5, ...\}$. The same parameters also fit the estimated intensities when the scattered polarization vector is analyzed perpendicularly to that of the incident one if again an imperfect alignment between the polarizer and the half-wave plate ($\lambda/2$) is assumed. In contrast, the model function for the rotation about the y axis, which is equivalent to the one about the x axis, does not represent the experimental findings for the nitrogen-related modes upon rotation about the x axis of the hexagonal structure. No angular dependence is found on rotation when the scattered radiation is analyzed parallel to that of the incident one except for the nitrogen-related mode at about $645\,\mathrm{cm}^{-1}$ as depicted in figure 4.9(a). On the other hand, four out of five additional modes reveal a specific dependence on rotation for perpendicularly oriented polarization vectors, see figure 4.9(b). For both polarization configurations, the parameters listed above only account for scattered intensities that are independent of the rotation angle. Therefore, the assignment proposed by Manjón *et al.* is in question if

the assumption is valid that the perturbation introduced by the defect N_O is large enough to manipulate the Raman activity and the symmetry character of extended lattice modes.

It should be noted, however, that the experimental findings upon rotation for the Raman-active ZnO lattice vibrations in the ZnO:N samples can be described using the picture above. The original E_1 and E_2 modes in the hexagonal crystal class C_{6v} are given by a combination of the two E modes in C_{3v} symmetry. As already discussed, the shape of the A_1 mode is preserved when the symmetry is reduced. Keeping this and the tensors listed in 4.1 in mind, the theoretical intensity dependence on rotation can be calculated for the original A_1, E_1, and E_2 modes. The outcomes seem to match the experimental findings for the Raman-active ZnO lattice vibrations.

If clusters or complexes are aligned in a particular manner with respect to the crystal axes of the ZnO host matrix, the scattered intensities of the corresponding modes will exhibit to some extent a dependence on rotation about the crystal axes. Jokela and McCluskey reported on absent or sine-like intensity dependence in infrared-spectroscopic experiments on polarization rotation of modes associated with N_O-H and O-H complexes in ZnO [99, 107]. Their findings indicate that these complexes are tilted under a well defined angle with respect to the c axis. Similar results are expected to occur in Raman experiments. The N_O-H mode is visible at about $3152\,\mathrm{cm}^{-1}$ in the Raman spectra of the CVD grown specimens, however, it does not show an angular-dependent intensity modulation on sample rotation (not shown). These results do not confirm the observations by Jokela and McCluskey and may indicate that N_O-H complexes are oriented at random in CVD grown nitrogen doped ZnO. This demonstrates that the formation of an aligned complex might depend on the synthesis condition. With this picture in mind, one may speculate if the nitrogen-related modes originate from complexes or clusters oriented at random in ZnO:N excluding the MBE grown samples.

Concluding remarks

The lattice dynamics of ZnO crystallizing in a wurtzite structure were studied under the influence of nitrogen doping. Up to an amount of 10^{21} nitrogen atoms/cm^3 incorporated in ZnO, the signals corresponding to Raman-active ZnO lattice vibrations neither shift in frequency nor vary in line shape, their pressure coefficients match those of pure ZnO, and their behavior upon rotation is consistent with the corresponding symmetry characters of an ideal ZnO hexagonal crystal structure belonging to the point group C_{6v}. Only the outcomes for the lattice vibration of E_2^{high} symmetry character upon rotation could not adequately be explained by its symmetry type. The reason is not clear yet. Nevertheless, the experimental findings provide evidence that the Raman-active ZnO lattice vibrations are not influenced by doping the II-VI compound semiconductor with nitrogen and corroborate the assumption that the doped

samples still possess a high crystal quality, i.e., that the translational symmetry is not strongly perturbed.

Nitrogen doped ZnO reveals five additional modes in the frequency range between 277 and 860 cm^{-1} next to the Raman-active ZnO lattice vibrations independent of the growth technique applied. The additional modes scale in intensity with nitrogen content and shift between about 1.6 and 6.0 $\text{cm}^{-1}/\text{GPa}$ upon hydrostatic pressure, which matches the range of pressure coefficients reported for Raman-active ZnO phonons. In contrast to ZnO lattice vibrations, the nitrogen-related modes are independent in signal intensity on sample rotation about the y or z axis of the hexagonal structure in CVD grown samples. Only in MBE grown nitrogen doped ZnO, the additional modes revealed an intensity dependence on rotation about the x axis normal to the m-plane. Further experimental work must be done to clarify if there exists a correlation between the symmetry characteristics of the nitrogen-related modes and the synthesis method of the samples or their crystal orientation.

Various attempts to explain the appearance of the additional modes in nitrogen doped ZnO were introduced: a local vibration of a single N atom on anion site or of a simple diatomic molecule may clarify the origin of any one nitrogen-related mode but this kind of defect cannot account for five different signals observed in an experiment. One solution proposed by Manjón and coworkers assigned the additional modes to silent B modes of wurtzite ZnO and their corresponding second-order processes, induced by the breakdown of the translational symmetry of the lattice caused by defects or impurities [19]. This approach may also explain the observation of the additional modes by Bundesmann *et al.* in ZnO doped with various other elements than nitrogen [13]. Although the Raman-active ZnO modes have been described quite accurately in theory, there are large discrepancies for the silent B modes between the outcome of *ab initio* calculations and the nitrogen-related modes observed in experiments. For example, the calculated vibrational frequencies do not match the ones of the additional signals in N doped ZnO well, nor is the estimated pressure coefficient for the combination mode 2B_1^{low} close to the one derived from experiment for the N-related signal at about $511\,\text{cm}^{-1}$. Based on the experimental findings, it is not possible to identify the symmetry type of the nitrogen-related modes; however, their symmetry characteristics cannot be represented in a conclusive picture by silent B modes of wurtzite ZnO if the assumption is valid that the perturbation introduced by the defect N_O is large enough to manipulate the Raman activity and the symmetry character of extended lattice modes. None of the findings alone may give conclusive evidence for the origin of the additional modes, but taken together, the assignment of these ones to silent B modes of wurtzite ZnO becomes disputable.

Furthmüller *et al.* showed with *ab initio* density functional theory and quasiparticle calculations that clustering of N atoms in ZnO is energetically favored over the formation of an isolated N atom on an anion site [108]. Clusters containing N atoms/ions may exhibit several Raman-active vibrations that may explain all additional modes observed in N doped ZnO. Conclusively, an increase in

N content in the ZnO specimens leads to higher density of clusters within the sample volume excited by the laser in the Raman experiment and therefore to an increase in scattered intensity. An absent angle dependence of the Raman intensity is known to occur for gases or liquids, where molecules serving as scatterers are oriented at random. A similar situation may arise if an ensemble of clusters containing N atoms/ions of different orientations within a ZnO matrix are probed. Depending on the crystal orientation of the substrate and/or the growth method employed, the clusters may reveal a preferred orientation with respect to the hexagonal structure and then exhibit a dependence on sample rotation, as observed in case of the m-plane oriented MBE grown specimens. Based on these considerations, the formation of Zn_3N_2-like clusters in N doped ZnO is the subject of the following chapter.

4.4 Evidence and influence of Zn_3N_2-like clusters in nitrogen doped ZnO

The schematic phase triangle in figure 4.10 illustrates the phase coexistence in the Zn-N-O system. The figure is provided by Prof. Dr. J. Janek along with the following description [109]: The thermodynamically stable compounds ZnO, Zn_3N_2, and $Zn(NO_3)_2$ are included in the phase triangle. In addition, the existence of a narrow homogeneous phase field (green shaded area) for the non-stoichiometric solid solution $ZnO_{1-3x+\delta}N_{2x}$ is assumed which basically corresponds to non-stoichiometric wurtzite ZnO with some N on O sites. The latter solid solution should exhibit the same Raman spectra as ZnO with at maximum two local modes due to N_O. Under oxidizing condition the formation of zinc nitrate may occur, but probably only at low temperatures (three-phase fields II, III, and V). The addition of nitrogen to ZnO under reducing conditions will lead to the formation of a Zn_3N_2 secondary phase once the solubility limit for nitrogen is exceeded (three-phase regions I and IV). Accordingly, the attempt to incorporate high amounts of nitrogen into ZnO may lead to precipitation of Zn_3N_2-like clusters in an otherwise hexagonal crystal structure of non-stoichiometric $ZnO_{1-3x+\delta}N_{2x}$. The following discussion will therefore focus on the characteristics of Zn_3N_2, its lattice dynamics from a theoretical point of view as well as on experimental Raman spectra of Zn_3N_2 powder. In the end, possible consequences for the properties of wurtzite ZnO or rather $ZnO_{1-3x+\delta}N_{2x}$ due to the formation of Zn_3N_2-like clusters are briefly addressed.

Lattice dynamics of zinc nitride – predictions by group theory and experimental Raman spectra

Zinc nitride (Zn_3N_2) crystallizes in a cubic anti-bixbyite structure belonging to the space group T_h^7 ($Ia\bar{3}$, No. 206) [110–113]. Its primitive unit cell contains 40 atoms, yielding 117 optical and three acoustic phonon branches [114]. The
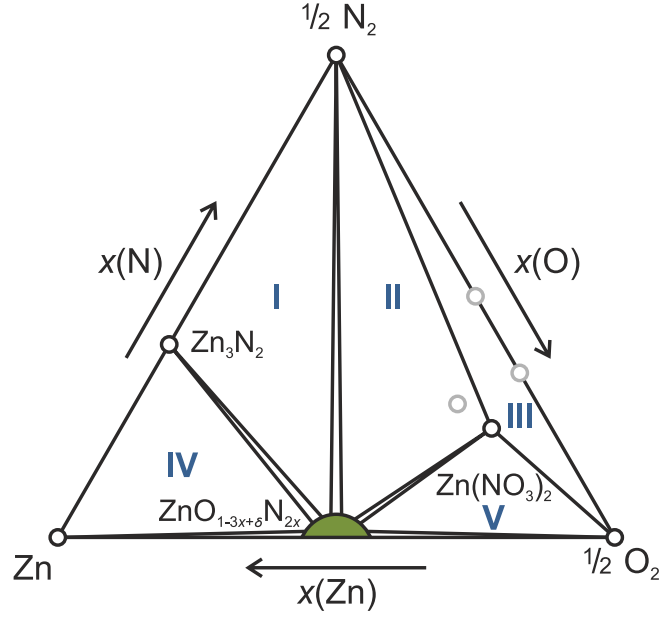
Figure 4.10: Schematic Gibbs phase triangle for the Zn-N-O ternary system (isothermal cross-section) including the thermodynamically stable compounds ZnO, Zn_3N_2, and $Zn(NO_3)_2$ as well as narrow homogeneous phase field (green shaded area) for the non-stoichiometric solid solution $ZnO_{1-3x+\delta}N_{2x}$ [109]. Grey circles indicate further compounds or phases.

symmetries of the vibrational modes at the center of the Brillouin zone are [115]:

$$\Gamma = 4A_g \oplus 5A_u \oplus 4E_g \oplus 5E_u \oplus 14T_g \oplus 17T_u \qquad (4.2)$$

Lattice vibrations of E and T symmetry type are twofold- and threefold-degenerate, respectively. Vibrational modes of A_g, E_g, and T_g symmetry character are Raman active. The three acoustic phonons have T_u symmetry character while the remaining 16 modes of T_u character are infrared-active phonons. A_u and E_u modes are silent. According to the group theoretical analysis there are in total 22 Raman-active modes in Zn_3N_2.

Experimental Raman spectra of extended crystalline Zn_3N_2 specimens have not been reported in the literature to date. In sputtered Zn_3N_2 thin films three broad features in the region of 260, 570, and $700\,cm^{-1}$ have been observed, whereas Raman spectra of CVD grown microtips, which are likely contaminated with oxygen, exhibit a rich structure of several features at about 267, 325, 372, 433, 504, 571, and $610\,cm^{-1}$ [116–120]. The 22 Raman-active modes predicted by group theory have not been identified in experiment yet, which might be due to the lack of highly crystalline specimens.

Here, Zn_3N_2 powder was studied as crystals have not been available. The spectrum of Zn_3N_2 powder (Alfa Aesar) in figure 4.11 exhibits five well separated signals at about 198, 266, 322, 426, and $563\,cm^{-1}$. It must be noted that Raman
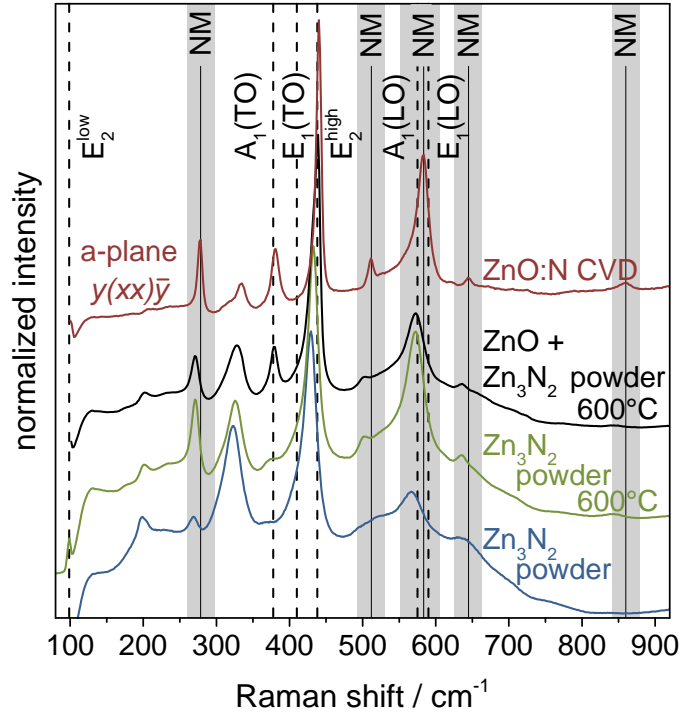
Figure 4.11: Normalized Raman spectra of Zn_3N_2 powder, Zn_3N_2 powder annealed at 600°C in air, and a CVD grown N doped ZnO layer ([N] $\approx 2.93 \times 10^{20}$ atoms/cm^3). The spectra were recorded in backscattering geometry at room temperature using a linearly polarized 532 nm laser for excitation. The Zn_3N_2 samples were measured unpolarized. For comparison a combination of a ZnO sample and Zn_3N_2 powder annealed at 600°C spectra is shown (black solid line). Black, dashed lines indicate Raman-active ZnO lattice vibrations and grey, shaded areas nitrogen-related signals. For clarity, the spectra have been shifted on the axis of ordinates.

spectra of randomly oriented scatterers in a liquid as well as in a powder sample or clusters embedded in a host matrix might differ from spectra of an ideal crystal structure [40, 64, 65]. Apart from a shift to lower wave numbers, the appearance of the peaks in the spectra of the Zn_3N_2 powder is somewhat similar to that of the (additional) signals in nitrogen doped ZnO samples. The discrepancy almost vanishes after annealing the powder successively at 400, 500, 550, and 600°C in air. Each time the powder was annealed for two hours and subsequently cooled down to room temperature before taking a Raman spectrum. In the end, the blackish appearance of the powder changed to a greyish/greenish color. In the Raman spectra of the annealed sample, the Zn_3N_2-like signals shift to higher wave numbers and three signals at about 502, 636, and 844 cm^{-1} become more pronounced. This may be related to the incorporation of oxygen, leading to the formation of a ZnO phase in Zn_3N_2 confirmed by X-ray diffraction (XRD). The linear combination of the Raman spectra of annealed Zn_3N_2 powder and of pure wurtzite ZnO shows a striking agreement with the

Raman spectrum of ZnO:N, demonstrating that the additional signals in nitrogen doped ZnO may indeed originate from cubic Zn_3N_2-like clusters. Since it is possible that in specific modes only zinc lattice planes vibrate, the observation of Zn_3N_2 phonons does not contradict the results by Artús *et al.*, who demonstrated that N motion is not involved in three of the nitrogen-related modes [17].

It should be noted that an XRD analysis of representative CVD grown, MBE grown, and sputtered N doped ZnO layers did not reveal any evidence of a secondary phase, in particular no Zn_3N_2 reflections are observed. This implies that the Zn_3N_2-like clusters are very small. This conclusion is in agreement with the Raman experiments. The Zn_3N_2-like clusters need to be very small so that their number within the sample volume excited by the laser in the Raman experiment is sufficient to yield the behavior of an ensemble of randomly oriented scatterers (at least in case of the c-plane oriented ZnO:N sample, see discussion below). On the other hand, the clusters must be large enough to exhibit similar Raman signatures than annealed Zn_3N_2 powder. Extensions of a few nanometers only corresponding to maybe tens of atoms are likely, therefore, the clusters may also be regarded as Zn_3N_2-like nanoinclusions.

Depolarization ratios of the nitrogen-related modes

The hypothesis of randomly oriented Zn_3N_2-like clusters in nitrogen doped ZnO is to some extend corroborated by the findings for the depolarization ratio ρ of the additional modes introduced in the preceding chapter. The depolarization ratio depends on the experimental scattering geometry and is determined by the nonzero Raman tensor elements [39, 40]. Therefore, it yields information about the symmetry characteristics of Raman-active modes even when probing an ensemble of randomly oriented scatterers. Depolarization ratios are tabulated for various scattering geometries of the direction of the incident and scattered radiation in the book by Long [39]. For lattice vibrations of A_g, E_g, and T_g symmetry character in the cubic crystal class T_h analyzed in a backscattering configuration one obtains ratios of 0, 3/4, and 3/4, respectively. In resonant Raman scattering, where the excitation frequency is close to singularities in the electronic susceptibility or polarizability of the material under study (here to an interband transition across the band gap of the nanoinclusions), antisymmetric tensors contribute to the scattered Raman intensity and modes of T_g symmetry character may exhibit $\rho > 1$ (anomalous depolarization ratio). However, depolarization ratios of vibrations with A_g and E_g symmetry in a cubic crystal system are not altered by the resonance, i.e., ρ remains 0 and 3/4, respectively. A vanishing ρ value occurs only for A type vibrations in cubic symmetry groups since no Raman tensor of any other crystal class possesses only equal, diagonal tensor elements.

The corresponding experimental values can be determined from the data points in figures 4.7, 4.8, and 4.9. In case of the c-plane oriented ZnO:N specimen, four of the five nitrogen-related modes, except the $645\,cm^{-1}$ signal, exhibit $\rho \approx 0$

in accordance with originating from A symmetry character modes of randomly oriented cubic nanoinclusions within the ZnO matrix. A ratio $\rho \approx 1$, as observed for the $645 \, \mathrm{cm}^{-1}$ signal, may indicate that the visible excitation is in resonance with an interband transition of the nanoinclusions. Incorporation of N into ZnO typically leads to a brownish appearance of the specimens. The assumption that the corresponding absorption in the visible spectral range is related to the formation of cubic Zn_3N_2-like nanoinclusions, is consistent with the resonance behavior indicated by $\rho \approx 1$ of the additional signal at $645 \, \mathrm{cm}^{-1}$ and in accordance with a vanishing depolarization ratio for the remaining nitrogen-related modes associated with A type vibrations. The findings for the additional modes of the a- and m-plane oriented specimens do not yield vanishing depolarization ratios. This is in contrast to A type vibrations in cubic symmetry groups of randomly oriented scatterers, thus, being a major shortcoming of the model proposed. On the other hand, it may simply demonstrate a preferred orientation of the Zn_3N_2-like clusters in the ZnO host matrix controlled by the synthesis conditions and/or substrate orientation.

Consequences due to the formation of Zn_3N_2-like clusters

The formation of Zn_3N_2-like clusters or nanoinclusions in nitrogen doped ZnO may limit the achievable concentration of the deep acceptor N_O in ZnO which may explain why no local vibrations of N atoms on anion sites have been reported yet. Furthermore, nitrogen doped ZnO films show a donor acceptor pair (DAP) emission at about $3.24 \, \mathrm{eV}$ as the signature of the shallow acceptor [14, 88, 121–124], allowing one to speculate that the occurrence of this acceptor may be correlated with the formation of Zn_3N_2-like nanoinclusions at high N content as proposed by Limpijumnong *et al.* [125]. The interfaces between the Zn_3N_2-like nanoinclusions and the surrounding $ZnO_{1-3x+\delta}N_{2x}$ matrix may be the location of the corresponding acceptor [125]. If the hypothesis above is valid, controlling the formation of Zn_3N_2-like clusters and making active use of their correlation with the shallow acceptor may prove to be a novel approach for achieving p-type ZnO-based material.

However, it must be noted that not all ZnO:N samples analyzed did exhibit the DAP emission at all or some time after their growth, whereas the nitrogen-related modes seem to be always present in the corresponding Raman spectra. In earlier investigations of CVD grown samples, Lautenschläger *et al.* already demonstrated that the DAP emission depends on the amount of nitrogen incorporated as well as on the substrate orientation and polarity [124]. Further experimental work is required to explore the correlation between the additional modes in the Raman spectra and the DAP emission in low temperature photoluminescence experiments, its degeneration, and the speculative formation of Zn_3N_2-like clusters.

	experimental observations	origin of the nitrogen-related modes			
		LVM N_O	diatomic molecule	silent ZnO modes	clusters (Zn_3N_2)
N-related modes	number of modes	−	○	+	+
	increase in intensity with nitrogen content	+	+	+	+
	appearance independent of growth technique	○	○	○	○
	dependence on hydrostatic pressure	○	○	−	+
	dependence on sample rotation (symmetry)	○	○	−	+
ZnO	dependence on sample rotation (symmetry)	+	+	+	+

Table 4.4: Comparison of the various explanations for the appearance of the nitrogen-related modes in N doped ZnO to the experimental observations. The symbols + and − indicate whether the experimental findings are in agreement with the explanation of the origin or not. If an ansatz does not yield a (distinct) prediction, the corresponding cell is marked with an open circle ○.

Concluding remarks

Table 4.4 compares the various attempts to explain the appearance of the additional signals in N doped ZnO to the experimental observations. The Raman modes due to Zn_3N_2-like clusters or nanoinclusions may explain all additional modes and their characteristics in ZnO after N incorporation. However, structurally different clusters containing N atoms/ions, like ZnN_4, cannot entirely be ruled out based on the findings so far. Transmission electron microscopy (TEM) experiments may clarify the existence of clusters and identify their shape in N doped ZnO. In addition, theoretical modeling may give insight into whether Zn_3N_2-like clusters are energetically favored and how their orientation depends on the growth conditions.

5 Lattice dynamics of Cu_2O – correlation of intrinsic defects and Raman modes

The copper-oxygen compound system can crystallize in different structures characterized by different oxidation states of copper depending on the growth method and synthesis conditions [33, 126]: CuO (tenorite or cupric oxide, τ), Cu_4O_3 (paramelaconite, π), or Cu_2O (cuprite or cuprous oxide, κ). Cupric and cuprous oxide are thermodynamically stable, whereas the paramelaconite phase is metastable [127–129]. In addition, non- and metastable Cu_xO_y defect phases have been reported in the literature [130, 131]. Each oxidation state of the copper-oxygen system exhibits distinct Raman spectra due to their differences in crystal structure, making them easily distinguishable from each other in experiments.

The Raman spectrum of crystalline cuprous oxide stands out. For the most part, it is independent of the growth method and the conditions employed. Curiously, however, Raman spectra of Cu_2O are dominated by Raman-forbidden infrared-active and silent lattice vibrations rather than by the single Raman-active phonon predicted by group theory for the ideal crystal structure. This unusual finding is in contrast to the Raman spectra of most other crystalline materials and is the subject of the following chapter. The first two sections focus on selected properties of Cu_2O, its lattice dynamics from a theoretical point of view, and the unusual Raman spectra observed in the experiments. Two possible explanations are considered: resonant Raman scattering, where the exciting laser or scattered photon frequency is close to singularities in the electronic susceptibility or polarizability of the material under study, and scattering by phonons with an arbitrary wave vector, which is known to occur in amorphous materials. Under certain conditions, resonant Raman scattering mechanisms or the relaxation of the wave-vector selection-rule can explain the observation of normally Raman-forbidden lattice vibrations in experiment. In the third part, intrinsic defects typically occurring in cuprous oxide are addressed. It is shown that these may be a another cause for the unusual Raman spectra. A group theoretical analysis of the symmetry reduction due to the presence of defects demonstrates that either interstitial defects in a tetrahedral configuration or copper vacancies in the so-called split configuration, a point defect particular to Cu_2O, introduce Raman activity for all phonons that are Raman forbidden in case of a perfect crystal lattice. Density functional theory (DFT) calculations for supercell defect structures provide evidence that the copper split vacancy induces a strong perturbation of the crystal structure of Cu_2O, allowing the

conclusion that the unusual Raman spectra may be caused by the presence of copper split vacancies. This assumption is corroborated by the symmetry characteristics of the lattice vibrations observed in Raman spectra of a crystalline MBE grown Cu$_2$O sample with (100) orientation analyzed in the last section of this chapter.

Sample characteristics

The cuprous oxide (Cu$_2$O) thin films analyzed in this chapter have been grown by five different methods, i.e., copper oxidation by heating, ion-beam sputter deposition (IBSD), radio-frequency sputter deposition (RFSD), reactive sputter deposition (RSD), chemical vapor deposition (CVD), and molecular beam epitaxy (MBE). For comparison, a natural bulk crystal has been investigated.

5.1 Selected properties and lattice dynamics of Cu$_2$O

The crystal structures of the two stable phases and the single metastable phase of the copper-oxygen compound system are schematically illustrated in figure 5.1. Cupric oxide (CuO) crystallizes in a monoclinic structure belonging to the space group C_{2h}^6 ($C2/c$, No. 15) [132]. The crystal structure of paramelaconite (Cu$_4$O$_3$) is tetragonal, described by the space group D_{4h}^{19} ($I4_1/amd$, No. 141) [133, 134]. Cuprous oxide (Cu$_2$O) crystallizes in a cubic structure whose symmetry characteristics are given by the space group O_h^4 ($Pn\bar{3}m$, No. 224) and its corresponding point group O_h ($m\bar{3}m$) [135–139]. The band structure of the compound semiconductor Cu$_2$O shows a direct energy gap at the center of the Brillouin zone of about $2.17\,\mathrm{eV}$ at low temperatures ($4.2\,\mathrm{K}$) [140–142]. An electric-dipole transition across the direct gap, between the maximum of the valence band and the minimum of the conduction band at the Γ-point, is forbidden by the parity selection-rule [135, 143]. Natural Cu$_2$O crystals are translucent with a dark red or black color [144]. It is well established that cuprous oxide is intrinsically p-type conducting, most likely caused by intrinsic point defects (non-stoichiometry), in particular by copper vacancies and copper split vacancies [34, 145–150]. As depicted in figure 5.1(c), each oxygen ion (O^{2-}) has four copper (Cu$^+$) neighbors in a tetrahedral configuration and each copper ion is linearly coordinated with two oxygen ions as nearest neighbors at equal distances. These copper-oxygen bonds in Cu$_2$O are of combined ionic and covalent character [151].

The cubic crystal structure of Cu$_2$O has six atoms ($n = 6$) per primitive unit cell, i.e., two Cu$_2$O molecular units, leading to $3n = 18$ phonon branches [152]. In contrast, Cu$_4$O$_3$ has 14 atoms in its primitive unit cell and thus exhibits a total of 42 vibrational eigenmodes [33, 153], whereas cupric oxide contains four atoms per primitive unit cell, resulting in a total of twelve phonon branches [154, 155]. The vibrational modes of cuprous oxide are classified by the following
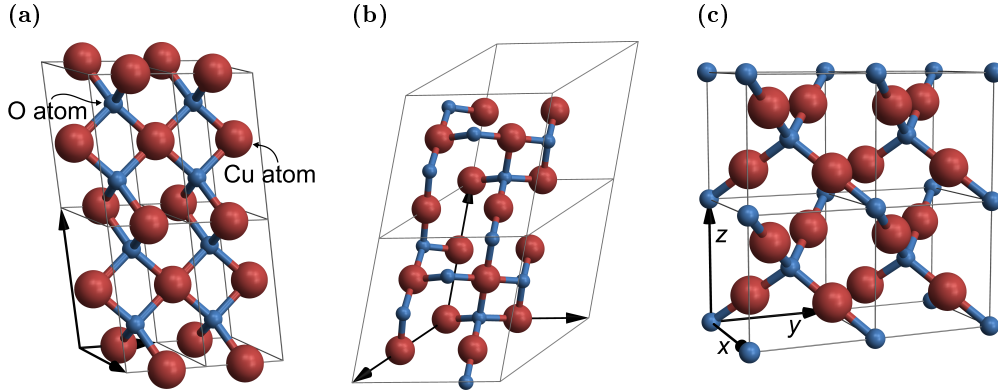
(a) **(b)** **(c)**

Figure 5.1: Schematic illustration of the three different phases of the copper-oxide compound system: (a) Cupric oxide (CuO) crystallizes in a monoclinic, (b)paramelaconite (Cu$_4$O$_3$) in a tetragonal, (c) and cuprous oxide (Cu$_2$O) in a cubic crystal structure. The orientation of the orthogonal coordinate axes x, y, and z is indicated for the cubic structure in (c).

irreducible representations of the crystallographic point group O_h at the Γ-point [135, 136]:

$$\Gamma = A_{2u} \oplus E_u \oplus T_{2g} \oplus 3T_{1u} \oplus T_{2u} \qquad (5.1)$$

Lattice vibrations of A, E, and T symmetry are one-, two-, and threefold-degenerated, respectively. The three acoustic phonons have T_{1u} symmetry character. Accordingly, the 15 optical phonon branches belong to the irreducible representations:

$$\Gamma_{opt} = A_{2u} \oplus E_u \oplus T_{2g} \oplus 2T_{1u} \oplus T_{2u} \qquad (5.2)$$

The two modes of T_{1u} symmetry character are infrared-active lattice vibrations, which split into longitudinal and transverse optical phonons similar to the A_1 and E_1 modes in ZnO. Phonons of A_{2u}, E_u, and T_{2u} symmetry are silent modes. The only Raman-active lattice vibration in Cu$_2$O belongs to the threefold-degenerated T_{2g} symmetry type. Due to the mode degeneracy, in total eight optical phonon branches are expected in cubic Cu$_2$O at the Γ-point: A_{2u}, E_u, T_{2g}, two $T_{1u}(LO)$, two $T_{1u}(TO)$, and T_{2u}.

The displacement of the copper and oxygen atoms of the six (or rather eight) optical lattice vibrations are schematically shown in figure 5.2 [135, 152]. The E_u, T_{2u}, and one of the T_{1u} mode patterns are rotations of the Cu tetrahedron about its center. The second mode of T_{1u} symmetry character consists of the relative motion of the Cu- and O-sublattices. Phonons of A_{2u} symmetry type are oscillations of the copper atoms along the diagonal axes of the cubic structure, being the breathing mode of the Cu tetrahedron, and T_{2g} lattice vibrations consist of the relative motion of the oxygen sublattices with respect to each other.
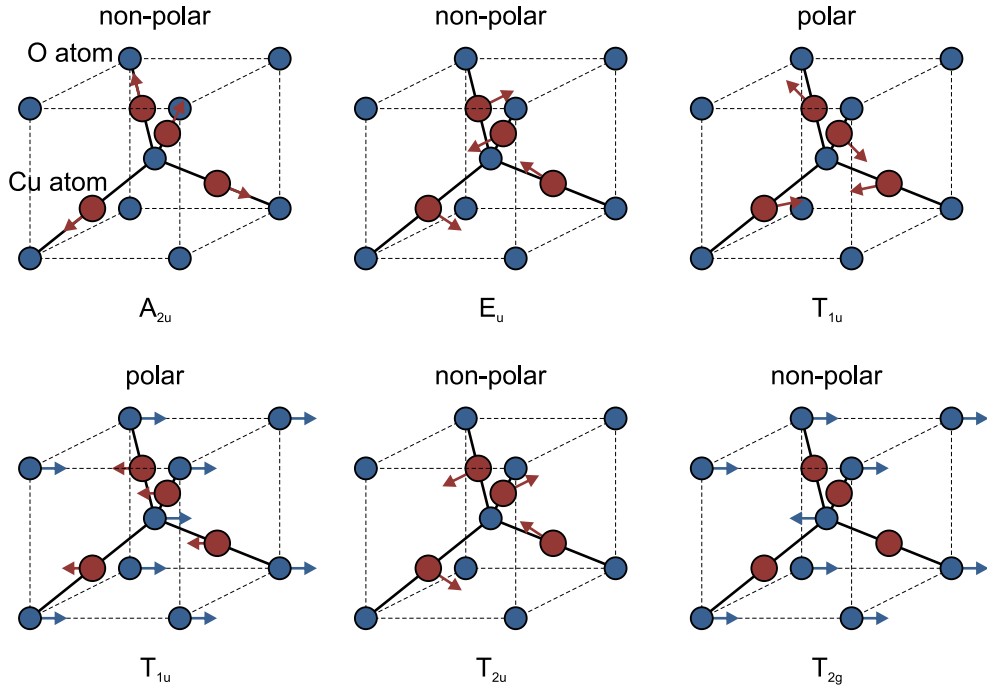
Figure 5.2: Atom displacement (eigenvectors) of the six optical lattice vibrations in cubic Cu_2O according to references 135 and 152.
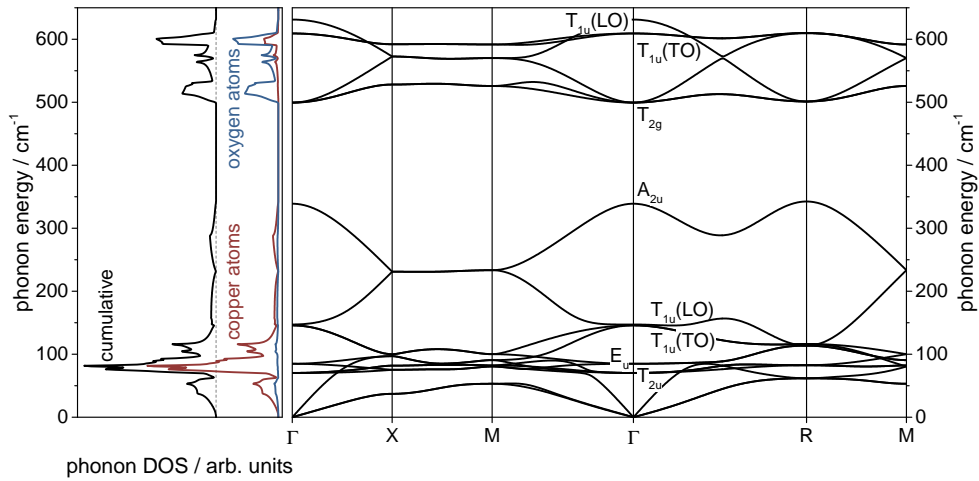

Figure 5.3: Phonon density of states (DOS) and dispersion relation along the main symmetry directions in the Brillouin zone of cuprous oxide determined by the real space small displacement method according to the group of Prof. Dr. C. Heiliger [156]. For clarity, the cumulative phonon DOS (black line) is shifted horizontally with respect to the ones involving only copper (red line) or oxygen atoms (blue line).

Figure 5.3 depicts the phonon dispersion relation of cuprous oxide for the main symmetry directions in the Brillouin zone and the corresponding phonon density of states determined by the real space small displacement method according to the group of Prof. Dr. C. Heiliger [156]. In accordance with the considerations above, eight optical phonon branches are found at the center of the Brillouin zone. The dispersion relation can be divided into four regions: (1) acoustic phonons, which pass through the origin, (2) optical phonons between about 70 and 340 cm^{-1}, involving predominantly oscillating copper atoms, (3) a forbidden gap between 340 and 500 cm^{-1}, and (4) optical phonons in the range of about 500 to 630 cm^{-1}, involving predominantly oscillating oxygen atoms.

5.2 Forbidden phonons in Raman spectra of Cu_2O

According to the group theoretical analysis, only lattice vibrations of T_{2g} symmetry character are Raman active in a perfect cubic Cu_2O crystal lattice. The Raman tensor of the threefold-degenerated T_{2g} mode can be divided into three individual matrices of the form [40]:

$$
\begin{pmatrix} 0 & 0 & 0 \\ 0 & 0 & d \\ 0 & d & 0 \end{pmatrix} \quad
\begin{pmatrix} 0 & 0 & d \\ 0 & 0 & 0 \\ d & 0 & 0 \end{pmatrix} \quad
\begin{pmatrix} 0 & d & 0 \\ d & 0 & 0 \\ 0 & 0 & 0 \end{pmatrix} \tag{5.3}
$$
$$
\mathrm{T}_{2g}^{(1)} \qquad\qquad \mathrm{T}_{2g}^{(2)} \qquad\qquad \mathrm{T}_{2g}^{(3)}
$$

These matrices are defined with respect to the basis axes of a right-angled coordinate system x, y, and z, depicted in figure 5.1(c), and determine whether the mode is detectable for a particular scattering configuration. Table 5.1 lists the symmetry selection-rules of the phonon of T_{2g} symmetry type in backscattering geometry. From this, it follows that a Raman spectrum of crystalline cuprous oxide aligned along a crystal axes should exhibit only one signal if the polarization vector of the scattered radiation is analyzed perpendicularly to that of the incident excitation laser or if all polarization orientations of the scattered radiation are analyzed simultaneously.

Figure 5.4 depicts Raman spectra of different crystalline Cu_2O samples, i.e., a natural bulk crystal, a thermally oxidized copper sheet as well as thin film samples grown by molecular beam epitaxy (MBE), chemical vapor epitaxy (CVD), ion-beam sputter deposition (IBSD), radio-frequency sputter deposition (RFSD), and reactive sputter deposition (RSD).[5] The Raman spectra were recorded in backscattering geometry using a linearly polarized 532, 633, or 785 nm laser for excitation. All polarization orientations of the scattered radiation were analyzed simultaneously (unpolarized Raman spectrum). With the exception of the MBE grown sample, which is described in section 5.4, the specimens do

---

[5]Note: The sample grown by radio-frequency sputter deposition (RFSD) may contain hydrogen.
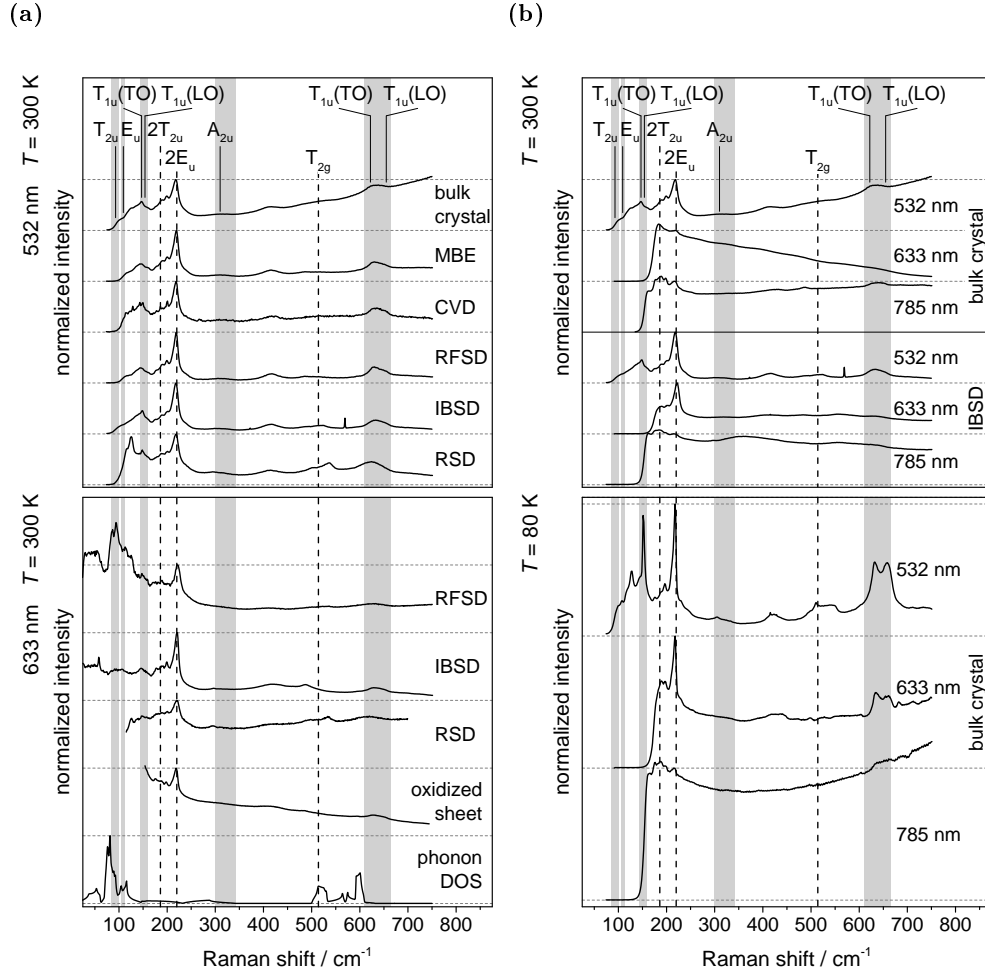
Figure 5.4: Normalized Raman spectra of cuprous oxide specimens grown by various techniques in comparison to a natural bulk crystal and to the calculated phonon DOS (see also figure 5.3). The spectra were measured unpolarized in backscattering geometry: (a) at room temperature using a linearly polarized 532 (top) or 633 nm (bottom) laser for excitation and (b) at room temperature (top) and at about 80 K (bottom) using a linearly polarized 532, 633, or 785 nm laser for excitation. Black, dashed lines indicate the Raman-active phonon of T$_{2g}$ symmetry type and selected Raman-active second-order scattering-processes. Grey, shaded areas display bands of Raman-forbidden signals. For clarity, the spectra have been shifted on the axis of ordinates.

mode/ tensor	frequency/ cm^{-1}	parallel polarization			crossed polarization		
		$x(yy)\bar{x}$ $x(zz)\bar{x}$	$y(xx)\bar{y}$ $y(zz)\bar{y}$	$z(xx)\bar{z}$ $z(yy)\bar{z}$	$x(yz)\bar{x}$ $x(zy)\bar{x}$	$y(xz)\bar{y}$ $y(zx)\bar{y}$	$z(xy)\bar{z}$ $z(yx)\bar{z}$
T_{2g}	512-515	-	-	-	×	×	×
$T_{2g}^{(1)}$		-	-	-	×	-	-
$T_{2g}^{(2)}$		-	-	-	-	×	-
$T_{2g}^{(3)}$		-	-	-	-	-	×

Table 5.1: Symmetry selection-rules of the single Raman-active T_{2g} phonon in Cu_2O for various scattering configurations denoted in the Porto notation. The contribution of the three matrices in equation (5.3) are given separately. Listed phonon frequencies are determined from experimental Raman spectra recorded at different temperatures (2 to 300 K) and using various excitation sources [4, 137, 152, 157–162].

not possess a distinct crystal orientation and thus an alignment along one of the crystal axes with respect to the polarization vector of the excitation laser is not possible. In contradiction to the theoretically expected Raman activities, the spectra in figure 5.4 reveal a multitude of signals almost independent of the method and conditions of the synthesis of the crystalline Cu_2O material. The dominant features are assigned to Raman-forbidden phonons of T_{1u} symmetry character and to the Raman-active second-order scattering-process $2E_u$, while the Raman-active T_{2g} phonon can only be conjectured as a weak feature. Similar spectra of bulk Cu_2O crystals are reported in the literature, slightly varying in mode intensities and number of modes observed [4, 137, 152, 157–162]. Table 5.2 summarizes the experimentally determined phonon frequencies in comparison to DFT calculations and lists their infrared or Raman activity based on the ideal crystal structure. These findings raise the question why the Raman activity and symmetry selection-rules for an ideal cubic Cu_2O crystal structure break down.

Resonant Raman scattering

The spectral differential cross-section for first-order scattering by phonons as well as the Raman activity and symmetry selection-rules, introduced in chapter 1.2 within the macroscopic framework, do not strictly hold any longer if the exciting laser or scattered photon frequency gets close to singularities in the electronic susceptibility or polarizability of the material under study. In other words if the incident or scattered photon frequency is close in energy to an electronic transition. New effects may occur under conditions of resonance that can be understood by a quantum mechanical treatment of Raman scattering (microscopic theory) [62]. The matrix elements contributing to the scattering cross-section may exhibit singularities in their energy denominator yielding an

	symbol/notation			degeneracy	Raman shift/cm^{-1}		activity
	Mulliken	Koster	BSW		experiment	DFT	
1st order scattering	T_{2u}	Γ_5^-	Γ_{25}	3	85-100	71	silent
	E_u	Γ_3^-	Γ_{12}'	2	107-110	84	silent
	T_{1u}	Γ_4^-	Γ_{15} (TO)	2	147-152	147	infrared
	T_{1u}	Γ_4^-	Γ_{15} (LO)	1	148-154	148	infrared
	A_{2u}	Γ_2^-	Γ_2'	1	300-350	338	silent
	T_{2g}	Γ_5^+	Γ_{25}'	3	512-515	499	Raman
	T_{1u}	Γ_4^-	Γ_{15} (TO)	2	609-635	608	infrared
	T_{1u}	Γ_4^-	Γ_{15} (LO)	1	645-665	630	infrared
2nd	$2T_{2u}$	$2\Gamma_5^-$	$2\Gamma_{25}$			181	Raman
	$2E_u$	$2\Gamma_3^-$	$2\Gamma_{12}'$			218-221	Raman

Table 5.2: Symmetry characters and Raman shifts of lattice vibrations observed in Raman spectra of Cu_2O in comparison to Raman shifts obtained by DFT calculations. The experimental Raman spectra were recorded at different temperatures (2 to 300 K) and using various excitation sources [4, 137, 152, 157–162], whereas the DFT results were calculated for $T = 0\,K$ [156]. The irreducible representations of the point group O_h are given in the Mulliken, Koster, and Bouckaert-Smoluchowski-Wigner (BSW) notation.

enhancement of the Raman scattering probability close to or at resonance. By this means higher order terms in the expansion of the matter-radiation (e.g., exciton-photon) and matter-lattice (e.g., exciton-phonon) interaction Hamiltonians may become significant, resulting in altered Raman activity and symmetry selection-rules with respect to off-resonance Raman scattering. Compaan and Cummins observed strong first-order Raman scattering in cuprous oxide of all Raman-forbidden modes, somewhat similar to the spectra shown in figure 5.4, when the exciting laser frequency is in resonance with the $1S$ exciton state of the lowest absorption transition (yellow exciton series), which is an electric-dipole forbidden but quadrupole allowed transition [163]. The sharp resonance of only a few wave numbers at $16396\,cm^{-1}$ (2.03 eV) as well as the observation and enhancement of Raman-forbidden phonons is a consequence of the electric-quadrupole term in the exciton-photon interaction Hamiltonian near resonance. Birman further demonstrated that the quadrupole-dipole Raman mechanism gives rise to new polarization and symmetry selection-rules that require novel third rank scattering tensors and that the scattered intensity explicitly depends on the wave vector of the incident field [164, 165]. Polarization-dependent Raman experiments at resonance of cuprous oxide have confirmed the theoretical predictions by Birman [166]. Further resonant Raman studies of Cu_2O may be found in references 160, 161, and 167 to 174 including the discussion of the possible alteration of the Raman activity and symmetry selection-rules through the intraband Fröhlich mechanism.

Figure 5.5 schematically illustrates the energy band diagram of cuprous oxide in

the vicinity of the Γ-point as well as the energies of the four fundamental absorption transitions, which are named according to the color of the corresponding electromagnetic radiation. Also shown are the energy positions of selected exciton states with respect to the energies of the excitation lasers used in the Raman experiments, depicted in figure 5.4. The energies of two excitation lasers, namely of wavelength 633 and 785 nm, are less than the lowest fundamental absorption transition of about 2.17 eV (4 K) in cuprous oxide and its excitonic transitions. Consequently, these lasers should not be in resonance with any electronic transition in Cu$_2$O at low temperatures. On the other hand, the energy of the 532 nm excitation laser is larger than the fundamental energy gap, located somewhere between the green and blue interband transitions, and therefore the corresponding scattered photons might be resonant with an electronic state of the green exciton series (outgoing resonance). With increasing temperature, the energy gap of Cu$_2$O decreases. It shifts about 100 meV from liquid helium (4 K) up to room temperature (300 K) to an estimated value of 2.096 eV [175]. Assuming for simplicity that all electronic states shift in the same manner and taking thermal broadening into account, the 532 and 633 nm excitation lasers may be in resonance with various electronic states of different natures at room temperature, e.g., electric-dipole allowed or forbidden transitions, as shown in figure 5.5(b). Defects may give further rise to new electronic states, which may be located energetically such that they coincide with the energies of the excitation lasers as well. Nevertheless, the conditions of resonance are not necessarily met for the experiments shown, in particular when using the 785 nm laser independent of the temperature or the 633 nm laser at 80 K. Therefore, the change of the Raman activity and symmetry selection-rules occurring in case of resonant Raman scattering may not or not only be responsible for the observation of normally Raman-forbidden phonons in Cu$_2$O.

It must be noted that not all specimens exhibit Raman-forbidden modes independent of the wavelength of the excitation laser used in experiment. For example, only the second-order scattering-processes 2E$_u$ and 2T$_{2u}$ have been observed in Raman spectra of ion-beam sputtered samples excited by the 785 nm laser, whereas Raman-forbidden modes are visible if the 532 or 633 nm lasers are used for excitation. No signals at all are found in Raman spectra of the MBE grown specimen excited by the 785 nm laser, in contrast to the broad features observed in natural bulk crystals. Apparently, there is a dependence on the excitation energy used and further experimental work is required to clarify the correlation between observed modes in Raman experiments and the wavelength of the excitation laser.

Relaxation of the wave-vector selection-rule

Comparing the calculated phonon DOS of cuprous oxide with the experimental Raman spectra, both depicted in figure 5.4(a), striking similarities appear with respect to their overall shape, e.g., both exhibit broad features and sharp peaks in the regions of the T$_{2u}$ and T$_{1u}$ lattice vibrations. These findings may
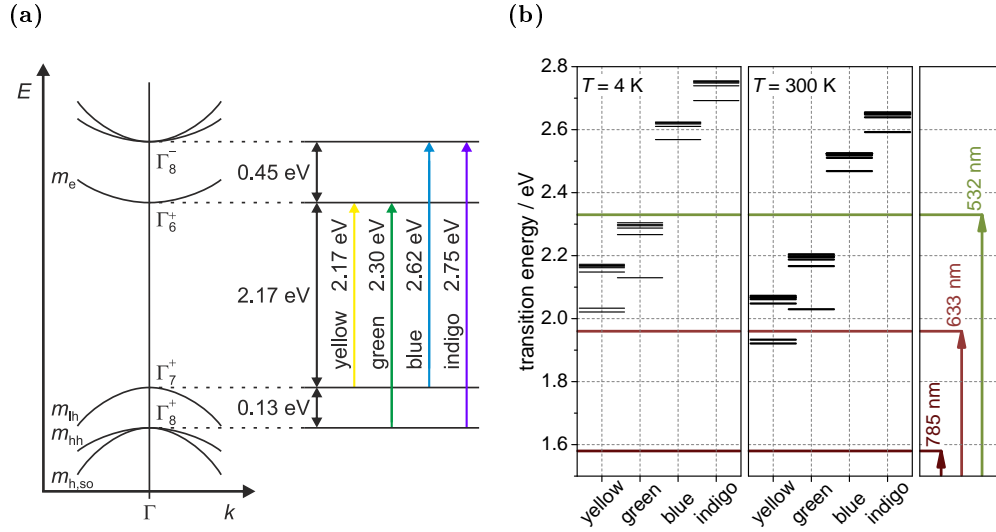
(a)

(b)

Figure 5.5: (a) Schematic illustration of the energy band diagram of cuprous oxide and of the four fundamental absorption transitions at the Γ-point (4 K) including the symmetry character of the bands [33]. (b) Exciton transition energies in cuprous oxide at 4 and 300 K with respect to the energies of three excitation lasers used in Raman experiments. The values at 4 K, obtained from reference 176, are shifted for simplicity by 100 meV to represent the transition energies at room temperature (300 K).

suggest that all modes in Cu₂O become Raman active due to the relaxation of the wave-vector selection-rule, as it was demonstrated at the end of chapter 1.3. However, scattering of phonons with arbitrary wave vectors ($\vec{q} \neq 0$) occurs only if the long-range order (translational symmetry) of the perfect lattice is lost, typical for amorphous and not for crystalline materials of good quality.

In conclusion, resonant Raman scattering mechanisms or scattering by phonons with arbitrary wave vectors may in principle explain the observation of all Raman-forbidden phonons in the spectra of Cu₂O, but neither are the conditions of resonance necessarily met at all times here, nor is it likely that the long-range order is strongly perturbed in all specimens studied. In particular, one may assume that the MBE grown thin film possesses a well defined crystal orientation according to an X-ray diffraction analysis, see chapter 5.4. It will be demonstrated in the next section that the symmetry reduction due to the presence of intrinsic defects may introduce Raman activity for all phonons, which may be a further cause for the unusual Raman spectra of Cu₂O observed in experiment.

5.3 Intrinsic defects in Cu_2O – breaking of Raman selection-rules

As mentioned in chapter 5.1, cuprous oxide is a natural p-type semiconductor whose conductivity is controlled by the cation deficiency (non-stoichiometry) [34]. Intrinsic point defects which may occur comprise copper and oxygen vacancies (V_{Cu}, V_O), antisite defects (Cu_O, O_{Cu}), interstitial defects in a tetrahedral configuration with four neighbors of the other species (Cu_i^{tet}, O_i^{tet}) and in an octahedral one with six neighbors of the other species (Cu_i^{oct}, O_i^{oct}), as well as a copper vacancy in the so-called split configuration (V_{Cu}^{split}), where a Cu atom adjacent to the vacancy moves into a position between the corresponding two Cu lattice sites. The cation deficiency depends on the amount of metal vacancies, oxygen interstitials, and oxygen antisites [34]. Theoretical studies argue that the two types of copper vacancies V_{Cu} and V_{Cu}^{split} are the likely causes for the natural p-type conductivity of Cu_2O as their formation energy is lower than that of other possible intrinsic acceptors such as the oxygen interstitials O_i^{oct} and O_i^{tet} [34, 145–150]. Thus, V_{Cu} and/or V_{Cu}^{split} are always present in this intrinsically p-type oxide.

The defects are located at specific sites of the unit cell of the Cu_2O crystal possessing a characteristic site symmetry, which is isomorphic to a subgroup of the point group to which the space group of the crystal belongs. A set of equivalent points within the unit cell possessing the same site symmetry is associated with a Wyckoff position. The multiplicity of a Wyckoff position denotes the number of equivalent points within the unit cell. The site symmetry of the defect is usually lower than that of the original point group belonging to the unperturbed crystal. As it was demonstrated in chapter 1.3, restricting the symmetry from that of the ideal crystal structure to the site symmetry of the defect may make the original irreducible representations of the lattice vibrations reducible, i.e., Raman-forbidden lattice vibrations may become Raman active and degeneracies may be lifted. A group theoretical analysis of the impact of substitutional defects on copper or oxygen sites has been performed by Reydellet *et al.* already in 1972 [4]. For V_O or Cu_O defects all experimentally observed lattice vibrations, except the former T_{2u} mode of the ideal crystal, become Raman active in scattering at the Γ-point. The lattice vibration of T_{2u} symmetry character is only Raman active if scattering at M- or X-points is allowed. The rather flat dispersion relation of the T_{2u} phonon branch and its nonzero phonon DOS at the M- or X-points, shown in figure 5.3, at first sight support the interpretation of defect activated scattering by zone edge phonons. However, the question remains why the corresponding breakdown of the wave-vector selection-rule should occur for this particular mode only or, even more severely, why should it be present in a crystalline material of good quality at all and this to an extent typical for an amorphous material. By extending and refining the analysis of Reydellet *et al.* it will be shown in the following that the additional assumption of a rigorous lifting of the wave-vector selection-rule is not necessary to describe the Raman spectra observed.

Table 5.3 summarizes the results of the analysis of the effect of intrinsic point defects in Cu_2O on the defect-induced Raman activity of the extended phonon modes at the Γ-point ($\vec{q} \approx 0$) of the ideal crystal. Bold printed representations indicate Raman-active modes. The irreducible representations given in the header of the table are those valid in O_h symmetry of the perfect crystal lattice. The columns below the original representation in O_h symmetry show its expansions in terms of the irreducible representations of the point groups representing the site symmetry of the various defects.

Point defects on copper sites (Wyckoff position b), i.e., V_{Cu} and O_{Cu}, as well as the octahedral interstitial defects Cu_i^{oct} and O_i^{oct} (Wyckoff position c) possess D_{3d} site symmetry and have the smallest impact on the Raman activity. The vibrational modes which are Raman forbidden in the ideal crystal remain Raman forbidden, whereas the representation T_{2g} of the Raman-active mode is expanded into two Raman active irreducible representations A_{1g} and E_g of D_{3d}. The point defects V_O and Cu_O related to the oxygen sites of the unit cell (Wyckoff position a) lift the Raman forbiddance for all phonon modes at the Γ-point with the exception of the former T_{2u} mode. Point defects on oxygen sites do not introduce mode splitting because of the still rather high T_d site symmetry. The presence of the interstitial defects Cu_i^{tet} and O_i^{tet} in the tetrahedral configuration (Wyckoff position d) introduce Raman activity for all Cu_2O extended phonon modes at the Γ-point. In addition, all originally degenerate modes split, i.e., the original E_u mode into A_1 and B_1 mode, and each original T mode into a sum of a twofold-degenerated E mode and a A_2 or B_2 mode. Except for the A_2 mode, all phonons are Raman active in D_{2d} symmetry. Similarly the presence of the V_{Cu}^{split} point defect introduces Raman activity for all Cu_2O extended phonon modes at the Γ-point and lifts their degeneracy, i.e., the original E_u mode splits into two A modes and each original T mode into a sum of B_1, B_2, and B_3 modes.

The group theoretical analysis implies that interstitial defects in the tetrahedral configuration and copper split vacancies are possible candidates to introduce Raman activity of all one-phonon modes of Cu_2O; however, it does not predict the magnitude of these effects. To estimate the magnitude of the crystal perturbation DFT calculations for supercell defect structures were conducted in the group of Prof. Dr. C. Heiliger [38, 156]. Figure 5.6 gives an estimate of the spatial extension and of the magnitude of the perturbation caused by an oxygen interstitial in the tetrahedral configuration (O_i^{tet}), a copper vacancy (V_{Cu}), and a copper split vacancy (V_{Cu}^{split}) by looking at the shift Δ of the positions of the atoms surrounding the defects upon relaxation with respect to the unperturbed structure. The shift Δ is obtained as the norm of the difference vector of each atom position between the relaxed perturbed and unperturbed structure. It is evident that the shifts of the positions of the atoms surrounding an O_i^{tet} or a V_{Cu}^{split} are considerably larger than the corresponding shifts of the atoms surrounding a V_{Cu} instead. Assuming that the envelope of the Δ-values is a straight line (dashed lines in the figure 5.6) and that its point of interception with the d_{defect}/a_{cubic}-axis is a rough measure of the spatial extension of the

| | point defect | | | | representations of vibrational modes of Cu$_2$O at the Γ-point in terms of irreducible representations of the site symmetry | | | | |
symbol	Wyckoff position	multi-plicity	site symmetry	crystal class	A_{2u}	E_u	T_{2g}	T_{1u}	T_{2u}
V_O, Cu_O	a	2	T_d	cubic	**A_1**	**E**	**T_2**	**T_2**	T_1
V_{Cu}, O_{Cu}	b	4	D_{3d}	trigonal	A_{2u}	E_u	**$A_{1g} \oplus E_g$**	$A_{2u} \oplus E_u$	$A_{1u} \oplus E_u$
Cu_i^{oct}, O_i^{oct}	c	4	D_{3d}	trigonal	A_{2u}	E_u	**$A_{1g} \oplus E_g$**	$A_{2u} \oplus E_u$	$A_{1u} \oplus E_u$
Cu_i^{tet}, O_i^{tet}	d	6	D_{2d}	tetragonal	**A_1**	**$A_1 \oplus B_1$**	**$B_2 \oplus E$**	**$B_2 \oplus E$**	$A_2 \oplus E$
V_{Cu}^{split}	f	12	D_2	orthorhombic	**A**	**2A**	**$B_1 \oplus B_2 \oplus B_3$**	**$B_1 \oplus B_2 \oplus B_3$**	**$B_1 \oplus B_2 \oplus B_3$**

Table 5.3: Characteristics of intrinsic defects occurring in cuprous oxide [4, 34, 60] and expansion of the irreducible representations of the phonon symmetry types in the O_h point group in terms of irreducible representations of the point groups representing the site symmetry of the intrinsic defects [41, 177]. Bold printed representations indicate Raman-active modes.
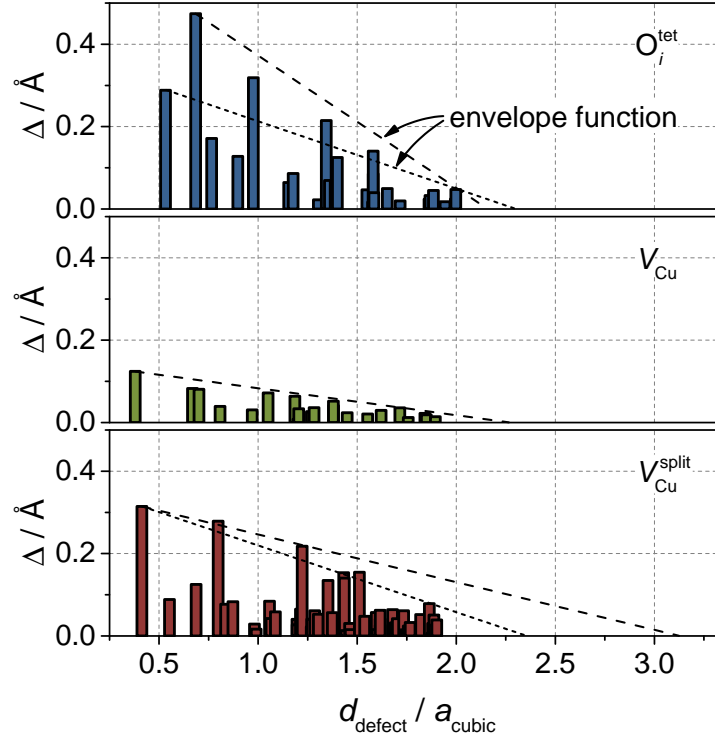
Figure 5.6: Shift Δ of atoms surrounding an oxygen interstitial defect in a tetrahedral configuration (O_i^{tet}), a copper vacancy (V_{Cu}), and a copper split vacancy (V_{Cu}^{split}) upon relaxation versus distance from the respective defect in units of the cubic lattice constant a_{cubic} (top to bottom graphs) [38, 156]. Dashed lines are envelope functions of the Δ values.

defect, i.e., it corresponds to the radius of the volume fraction affected by the defect site, one obtains for the V_{Cu}^{split} an extension between 2.3 and 3.1 a_{cubic}. On the contrary, the spatial extension of the oxygen interstitial or the copper vacancy seems to be of shorter range. The outcomes of the DFT calculations suggest that the V_{Cu}^{split}, which comprises several sites, induces a strong perturbation of the crystal structure of Cu$_2$O. In addition, the perturbation seems to be of longer range than that caused by simple point defects involving only one atom site.

The DFT calculations for supercell defect structures were carried out for a $4 \times 4 \times 4$ supercell (384 atoms) and an equilibrium lattice parameter a_{cubic} of 4.3033 Å, which yields a density of atoms in Cu$_2$O of about 7.5×10^{22} atoms/cm^3. If we assume that the volume fraction of the crystal perturbed by a V_{Cu}^{split} is a spherical volume with a radius of 3.1 a_{cubic}, it will contain about 749 atoms. Thus, the volume fractions perturbed by copper split vacancies in their centers make up the entire crystal volume at a critical defect density of about 1.0×10^{20} defects/cm^3. This number is about 10 times the typical density of V_{Cu}^{split} defects expected implying that 10 % of the crystal are strongly perturbed, which appears to be sufficient to reduce the ideal crystal symmetry

and thus yield additional signals in Raman spectra of cuprous oxide specimens.

5.4 Probing the symmetry characteristics of phonons in Cu_2O

The results of the previous sections showed that the infrared or Raman activity of phonons can be modified by an alteration of their symmetry character caused by a reduction of the ideal crystal symmetry or by a change of the Raman activity and symmetry selection-rules occurring in case of resonant Raman scattering. The new symmetry characteristics depend on the underlying process and therefore an analysis of the dependence of the scattered Raman intensity on the rotation of the sample or plane of polarization, as it was performed in chapter 3.3 for the lattice vibrations in wurtzite ZnO, might offer valuable information.

The subsequent discussion is restricted to a thin film specimen grown by molecular beam epitaxy (MBE) on a (100) oriented MgO substrate. The thickness of the epitaxial layer was estimated to be about 160 nm by optical spectroscopy [178]. An X-ray diffraction analysis of the Cu_2O specimen revealed a strong signal that can be assigned to the reflection of the (200) lattice plane of cubic Cu_2O and a second signal of negligible intensity that is attributed to the (220) lattice plane [178]. Both peaks are shifted to smaller 2Θ values than expected for bulk crystals indicating that the epitaxial layer is strained. From these findings one may assume that the thin film specimen possesses a well defined orientation with its surface being normal to the [100] direction (x axis) and, therefore, being suitable for polarization-dependent Raman experiments. To study the symmetry characteristics of the lattice vibrations, the Cu_2O specimen was rotated in distinct steps about the [100] direction (x axis) and at each position a polarized Raman spectrum was recorded in backscattering geometry at room temperature using a linearly polarized 532 nm laser for excitation. For simplicity, the intensities or amplitudes of the prominent features in the Raman spectra have been estimated by selecting the maximal data point of the corresponding signal and correcting it for a linear background chosen individually below each one with the naked eye.

Figure 5.7 depicts the intensities of the prominent features in the Raman spectra of the Cu_2O specimen as a function of the rotation angle ϕ about the x axis. The signal intensities never vanish completely; they vary between about 50 and 100 % in their maximal amplitude. With respect to the arbitrary chosen starting point, the intensity of the Raman-active phonon of T_{2g} symmetry character (at about $518\,cm^{-1}$) follows a $|\sin(2\phi)|^2$ and $|\cos(2\phi)|^2$ dependence on rotation for parallel and perpendicularly aligned incident and scattered polarization vectors, respectively. In comparison to the T_{2g} mode, the intensity dependence of the Raman-active second-order scattering-process $2E_u$ (at about $220\,cm^{-1}$) is phase shifted by $\pi/2$ (90°) being maximal when the T_{2g} mode is minimal and

97

vice versa in both scattering configurations. The same dependence on rotation is found for the Raman-forbidden lattice vibrations of A$_{2u}$ and T$_{1u}$ symmetry type (at about 311 and 633 cm^{-1}), i.e., one observes a $|\cos(2\phi)|^2$ and $|\sin(2\phi)|^2$ dependence for parallel and perpendicularly aligned incident and scattered polarization vectors, respectively. Since the observed signal intensities and their variations are small, it may be possible that the dependences on rotation are not caused by the phonon symmetry characteristics but are induced by an angle dependent background from the sample itself or the substrate and/or caused by the inaccuracy in rotating a sample about the same spot in experiment. Nonetheless, the findings shown in figure 5.7 will be discussed in the following with respect to the modifications of the phonon symmetry type as well as the Raman activity and symmetry selection-rules induced by (i) a relaxation of the wave-vector selection-rule, (ii) resonant Raman scattering, or (iii) the reduction of the ideal crystal symmetry caused by the presence of intrinsic point defects.

(i) Relaxation of the wave-vector selection-rule

All phonons may become Raman active if the wave-vector selection-rule of first-order Raman scattering ($\vec{q} \approx 0$) is lifted and scattering of phonons with arbitrary wave vectors is allowed. Lattice vibrations with different wave vectors (momenta) may now contribute to the same signal in the experimental Raman spectra, e.g., the dispersion relation of the T$_{2u}$ phonon branch in Cu$_2$O is rather flat and thus the scattered photon frequency is more or less independent of the phonon wave vector, see figure 5.3. At each point throughout the Brillouin zone the phonons possess specific symmetry characters that may differ from those at the Γ-point. Therefore, it is not practicable anymore to predict the symmetry characteristics of a Raman signal in experiment if the wave-vector selection-rule is relaxed. One may speculate that on average all symmetries occur such that the scattered intensity is independent of the polarization configuration in contradiction to the experimental findings depicted in figure 5.7.

(ii) Resonant Raman scattering – the quadrupole-dipole Raman mechanism

When the exciting laser frequency is in resonance with the $1S$ exciton state of the lowest absorption transition (yellow exciton series) in Cu$_2$O, all normally Raman-forbidden phonons become Raman active as a consequence of the electric-quadrupole (Γ_{25}^+) electric-dipole (Γ_{15}^-) Raman mechanism [163]. The latter mechanism yields new Raman activity and symmetry selection-rules. First-order scattering by this mechanism depends explicitly on the wave vector of the incident photon $\vec{k}_i$, in contrast to the Raman scattering-processes discussed so far. One obtains for the scattered intensity by a phonon of type k characterized
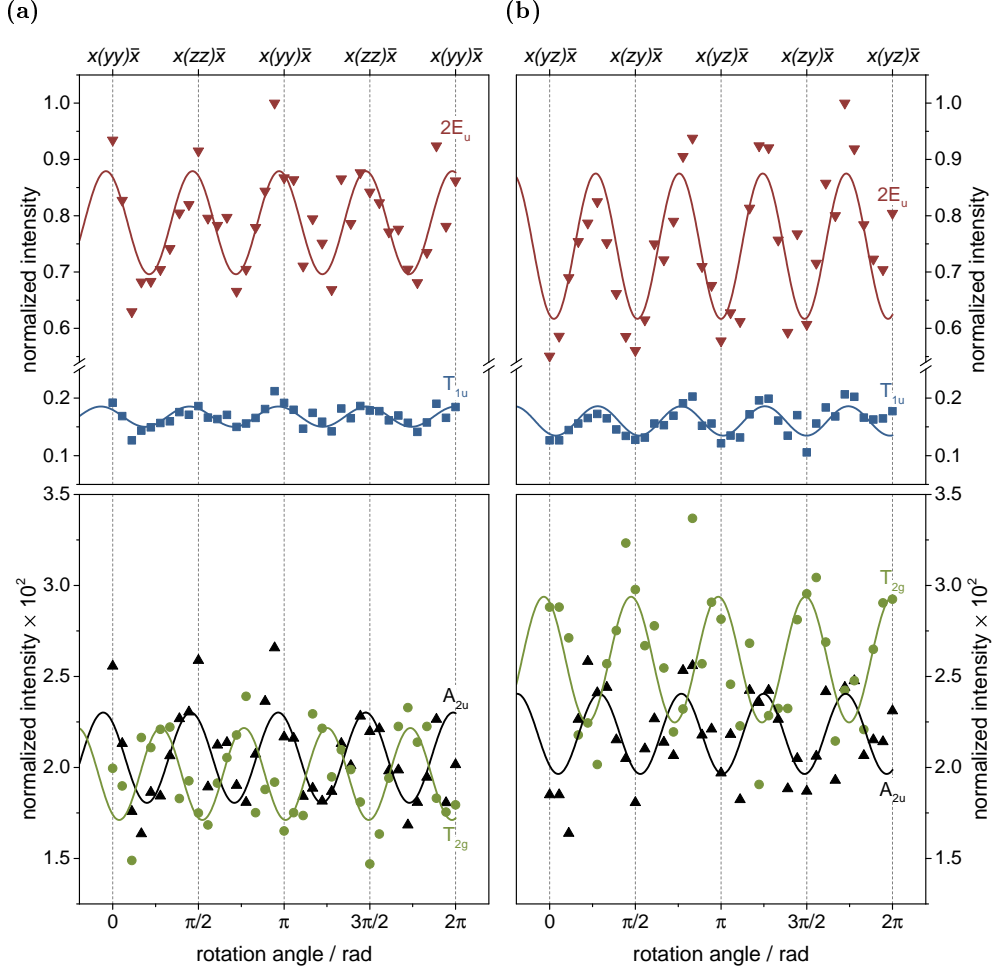
Figure 5.7: Normalized intensity of the prominent Raman signals of a MBE grown Cu$_2$O specimen versus sample rotation about the x axis for (a) parallel and (b) perpendicularly aligned incident and scattered polarization vectors. Signals are normalized to the maximum intensity of the Raman-active second-order scattering-process 2E$_\mathrm{u}$. Solid lines are fits to the data points. The scattering configurations denoted in the Porto notation are given with respect to the calculations for the dependence of the scattered intensity on rotation of the T$_\mathrm{2g}$ mode for an ideal crystal structure.

by σ different tensors [165]:

$$I^k \propto \sum_{\sigma} \left| \sum_{\alpha\beta\gamma} e_{s,\alpha} \cdot \mathcal{P}_{\alpha\beta\gamma}(k\sigma) \cdot e_{i,\beta} \cdot k_{i,\gamma} \right|^2 , \qquad (5.4)$$

where $\vec{e}_i$ and $\vec{e}_s$ are unit vectors representing the polarization of the incident and scattered radiation, respectively, and $\mathcal{P}(k\sigma)$ is the scattering tensor for multipole-dipole scattering. The indices α, β, and γ run over all space coordinates x, y, and z.

Table 5.4 lists the intensity dependence on rotation of all normally Raman-forbidden phonons in Cu$_2$O in case of electric-quadrupole (Γ_{25}^+) electric-dipole (Γ_{15}^-) resonant Raman scattering regarding the backscattering configuration of the experiments discussed, i.e., the incident photon wave vector being directed along the x axis and the polarization vectors of the incident and scattered radiation lying in the yz-plane in reference to the coordinate system depicted in figure 5.1(c). To obtain the intensity dependence on rotation, the polarization vectors were represented in polar coordinates, similar to those in equations (3.4) to (3.6), with ϕ being the rotation angle between $\vec{e}_i$ and the y axis. The required multipole-dipole scattering tensors were taken from the article by Birman [165]. The intensity dependence on the rotation about the x axis of the Raman-active T$_{2g}$ mode is given in table 5.4 as well. It was calculated using the approximation for the scattered intensity in equation (1.12), which is independent of the photon wave vector, and the Raman tensors listed in (5.3). The calculated dependences do not correctly represent the experimental findings for the normally Raman-forbidden phonons. This outcome is consistent with the assumption that the 532 nm laser is not directly in resonance with an electronic state at room temperature, at least not with an electric-dipole forbidden transition resulting in quadrupole-dipole Raman scattering, as it is illustrated in figure 5.5. Consequences of other resonance mechanisms in sense of modifications of the Raman activity and symmetry selection-rules remain an open question for further theoretical analyses.

(iii) Symmetry reduction induced by the presence of intrinsic point defects

The group theoretical analysis in the previous chapter 5.3 demonstrated that restricting the symmetry from that of the ideal crystal structure to the site symmetry of an intrinsic point defect in Cu$_2$O may alter the symmetry character and Raman activities of lattice vibrations. Assuming that each defect affects a certain volume possessing the properties of the local site symmetry and that these volume fractions add up to a considerable part of the entire crystal, the defect-induced changes in symmetry character and Raman activity should be reflected in the experimental Raman spectra. In particular, this should apply to the copper split vacancies in Cu$_2$O regarding the outcomes of the DFT calculations for supercell defect structures.

To calculate the intensity dependence on rotation of the defect activated modes, one has to consider the representation of the Raman tensors in the point group

scattering mechanism	symmetry	A_{2u}	E_u	T_{2g}	$T_{1u}(LO)$	$T_{1u}(TO)$	T_{2u}
parallel							
ideal crystal	O_h	-	-	$|\sin(2\phi)|^2$	-	-	-
resonant		$|\sin(2\phi)|^2$	$|\sin(2\phi)|^2$	-	constant	0	$|\cos(2\phi)|^2$
defect induced							
V_O, Cu_O	T_d	constant	constant	$|\sin(2\phi)|^2$	$|\sin(2\phi)|^2$	-	-
V_{Cu}, O_{Cu}	D_{3d}	-	-	unknown	-	-	-
Cu_i^{oct}, O_i^{oct}	D_{3d}	-	-	unknown	-	-	-
Cu_i^{tet}, O_i^{tet}	D_{2d}	$|\cos(2\phi)|^2$	$|\cos(2\phi)|^2$	$|\sin(2\phi)|^2$	$|\sin(2\phi)|^2$	-	$|\sin(2\phi)|^2$
V_{Cu}^{split}	D_2	$|\cos(2\phi)|^2$	$|\cos(2\phi)|^2$	$|\sin(2\phi)|^2$	$|\cos(2\phi)|^2$	-	$|\cos(2\phi)|^2$
experiment		$|\cos(2\phi)|^2$	-	$|\sin(2\phi)|^2$	$|\cos(2\phi)|^2$	-	-
perpendicular							
ideal crystal	O_h	-	-	$|\cos(2\phi)|^2$	-	-	-
resonant		$|\cos(2\phi)|^2$	$|\cos(2\phi)|^2$	-	0	0	$|\sin(2\phi)|^2$
defect induced							
V_O, Cu_O	T_d	0	0	$|\cos(2\phi)|^2$	$|\cos(2\phi)|^2$	-	-
V_{Cu}, O_{Cu}	D_{3d}	-	-	unknown	-	-	-
Cu_i^{oct}, O_i^{oct}	D_{3d}	-	-	unknown	-	-	-
Cu_i^{tet}, O_i^{tet}	D_{2d}	$|\sin(2\phi)|^2$	$|\sin(2\phi)|^2$	$|\cos(2\phi)|^2$	$|\cos(2\phi)|^2$	-	$|\cos(2\phi)|^2$
V_{Cu}^{split}	D_2	$|\sin(2\phi)|^2$	$|\sin(2\phi)|^2$	$|\cos(2\phi)|^2$	$|\sin(2\phi)|^2$	-	$|\sin(2\phi)|^2$
experiment		$|\sin(2\phi)|^2$	-	$|\cos(2\phi)|^2$	$|\sin(2\phi)|^2$	-	-

Table 5.4: Theoretical approximation for the dependence of the scattered intensity on sample rotation about the x axis of the cubic Cu_2O structure based on different scattering mechanisms, i.e., Raman scattering of an ideal crystal structure, electric-quadrupole (Γ_{25}^+) electric-dipole (Γ_{15}^-) resonant Raman scattering, and defect-induced Raman scattering in comparison to the experimental findings. The dependences listed are estimated for parallel and perpendicularly oriented incident and scattered polarization vectors.
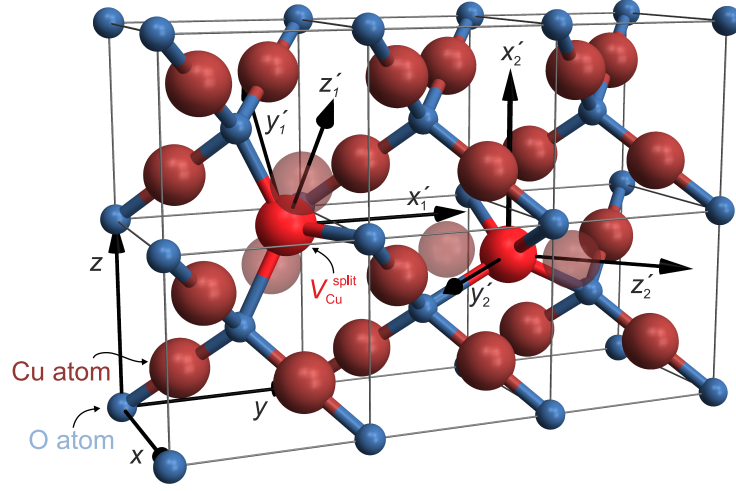
Figure 5.8: Schematic illustration of six primitive unit cells of Cu$_2$O with two copper split vacancies (light red atoms). The $V_{\text{Cu}}^{\text{split}}$ defects occupy different lattice sites that belong to the same Wyckoff position f. The local coordinate systems $(x_1' y_1' z_1')$ and $(x_2' y_2' z_2')$ are given with respect to the coordinate frame describing the ideal cubic Cu$_2$O structure (xyz). Red transparent atoms denote the original lattice sites of the copper atoms in the unperturbed ideal crystal structure.

of the site symmetry to which the defect belongs. Since Raman tensors are defined with respect to three orthogonal coordinate axes oriented in relation to characteristic symmetry elements of each crystal class, it is necessary to transform the rotation axes $\vec{r}$, which is directed along the x axis, as well as the polarization vectors $\vec{e}_\text{i}$ and $\vec{e}_\text{s}$, which lie in the yz-plane of the coordinate system (xyz) describing the ideal cubic Cu$_2$O structure, into the basic axes x', y', and z' of the local coordinate system specific for each point group or rather crystal class. Conventions for the choice of axes are given in the book by Nye [106]. As an example, figure 5.8 schematically illustrates two local coordinate systems $(x_1' y_1' z_1')$ and $(x_2' y_2' z_2')$ corresponding to the two copper split vacancies depicted with respect to the coordinate frame describing the ideal cubic Cu$_2$O structure (xyz). One obtains for the scattered intensities of an individual defect-activated mode k:

$$I^k \propto \left| [\boldsymbol{R}_{\boldsymbol{C}\vec{r}}(\phi)\boldsymbol{C}\vec{e}_\text{s}]^T \cdot \boldsymbol{\mathcal{R}}^k \cdot [\boldsymbol{R}_{\boldsymbol{C}\vec{r}}(\phi)\boldsymbol{C}\vec{e}_\text{i}] \right|^2 \tag{5.5}$$

$$\propto \left| [\boldsymbol{R}_{\vec{r}\,'}(\phi)\vec{e}_\text{s}\,']^T \cdot \boldsymbol{\mathcal{R}}^k \cdot [\boldsymbol{R}_{\vec{r}\,'}(\phi)\vec{e}_\text{i}\,'] \right|^2 , \tag{5.6}$$

where $\boldsymbol{\mathcal{R}}^k$ is the Raman tensor of mode k in the point group of the site symmetry, $\boldsymbol{C}$ the corresponding coordinate system transformation matrix, and $\boldsymbol{R}_{\vec{r}\,'}(\phi)$ a matrix describing the rotation about a vector $\vec{r}\,'$ by an angle ϕ. Primed variables indicate vectors given with respect to the basic axes of the local coordinate system $(x'y'z')$.

Table 5.4 summarizes the results of such calculations for each defect, assuming,

for simplicity, that the defects are evenly distributed on the equivalent sites of the corresponding Wyckoff positions. If the definition for the basis axes differs for multiple sites belonging to the same Wyckoff position, averaging of the intensities over the different orientations is required. The intensity dependence of the modes observed in experiment cannot be described correctly by defect-induced Raman activity caused by substitutional or interstitial defects. Only the copper split vacancy yields the correct angle dependence for all one-phonon modes analyzed if appropriate tensor elements are chosen and all outcomes are phase shifted by $\pi/2$ (90°). The original Raman-forbidden modes of T$_{1u}$ and T$_{2u}$ symmetry character can be represented by a sum of the averaged intensities of all three B modes, whereas at the same time the T$_{2g}$ phonon is given correctly with respect to the experimental findings by a sum of B$_1$ and B$_3$ modes implying that the B$_2$ tensor elements are zero. In this fashion, the angle dependence of the Raman signal corresponding to the T$_{2g}$ mode of the ideal crystal can be preserved in the presence of the $V_{\text{Cu}}^{\text{split}}$ point defect.

The angle dependence of the 2E$_u$ two-phonon signal can be estimated considering the expansion of the direct product E$_u \otimes$ E$_u$ = A$_{1g} \oplus$ A$_{2g} \oplus$ E$_g$ for the ideal Cu$_2$O crystal (O_h symmetry). The expansion corresponds to the representation 4A in D_2 symmetry, i.e., in the site symmetry of the copper split vacancy. Hence, the 2E$_u$ signal should exhibit the same angle dependence as the A$_{2u}$ one-phonon signal in the experiment. This is the case as shown in figure 5.7. The behavior of the 2E$_u$ signal thus is in agreement with the interpretation that the Raman activity of Cu$_2$O phonon modes is determined by the $V_{\text{Cu}}^{\text{split}}$ defects.

Shortcomings of the proposed model for the theoretical dependence on rotation are: (a) Not all determined trigonometric functions yield a nonzero minimum amplitude, which is however observed in experiment. This may be achieved by using antisymmetric Raman tensors. (b) It was not possible to define a local coordinate system for defects in D_{3d} symmetry. Thus, the dependence of the scattered intensity on rotation induced by defects on copper sites or interstitial defects in an octahedral configuration could not be determined. (c) The problem may be overdetermined since it was not necessary to account for an imperfect alignment of the polarizer and the half-wave plate ($\lambda/2$) in the setup for the case of perpendicularly oriented incident and scattered polarization vectors. However, the experimental results in chapters 3 and 4 demonstrate that such a correction is required. To improve the model these questions need to be addressed. In addition, the dependence of the scattered intensity on rotation of longitudinal and transversal optical phonons should be determined individually in a similar manner as it was done for resonant Raman scattering, see table 5.4. It is also necessary to review the dependences for the phonons of E symmetry type in T_d symmetry, since the Raman tensors given in reference 56 may not be correct.

Concluding remarks

Assuming that the intensity dependences on rotation are caused by the phonon symmetry characteristics and not by an angle dependent background or by inaccuracies in performing the experiments, the findings upon sample rotation support the idea that the Raman activity for all phonons that are Raman forbidden in the case of an ideal crystal structure is induced by the symmetry reduction due to the presence of intrinsic defects. It was further demonstrated in the preceding discussions that copper split vacancies induce a strong perturbation of the crystal structure of Cu_2O and that typical concentrations expected for copper vacancies appear to be sufficient to modify the extended phonon modes in Cu_2O. These findings allow one to conclude that the unusual Raman spectra of crystalline Cu_2O observed in experiment may be caused by the presence of copper split vacancies. No evidence was found for the relaxation of the wave-vector selection-rule; however, resonant Raman scattering mechanisms cannot entirely be ruled out to alter the Raman activity and symmetry selection-rules since the analyzed Raman spectra are dependent on the excitation frequency. Further insight could be achieved by performing Raman experiments of high quality Cu_2O crystals upon sample or plane of polarization rotation at low temperatures, in particular, polarization-dependent off-resonance Raman scattering experiments.[6]

---

[6]Note: Ivanda *et al.* observed anomalies in Raman spectra and X-ray diffractograms of a natural Cu_2O crystal at low temperatures and related these to instabilities in the Cu_2O structure [179]. Their findings should be taken into consideration when performing experiments at low temperatures.

Overall conclusions

Deviations from the ideal crystal structure, i.e., intrinsic or extrinsic defects, modify the dynamics of a crystalline lattice among many other material properties. As a consequence, additional modes may occur in Raman spectra, Raman-forbidden modes may become Raman active, and the shape as well as the position in the frequency of the Raman signals may change. The impacts of perturbations of the ideal crystal structure on Raman spectra are addressed within the framework of this thesis.

Crystalline ZnO samples were investigated using Raman spectroscopy. It is found that all experimental results are consistent with the laws of conservation as well as the Raman activity and the symmetry selection-rules established for an ideal crystal structure. With this in mind, the samples studied should be free of defects and have an ideal hexagonal crystal lattice. In reality, there are no perfect crystals as entropy always leads to the formation of defects [6]. Furthermore, it is well known that nominally undoped ZnO is often intrinsically n-type conducting due to intrinsic and/or, more likely, due to extrinsic defects [7–10]. Therefore, Raman spectroscopy is not sensitive to such kinds of defects at the concentration level present in the ZnO samples studied and in the frequency range considered here in experiment.

The situation is different when ZnO is intentionally doped with nitrogen. Raman spectra of nitrogen doped ZnO exhibit five additional modes independent of the growth technique applied. Various attempts to explain the appearance of the nitrogen-related modes have been reviewed [11–19]. A promising approach is the assignment of the N-related modes to silent ZnO phonons induced by the breakdown of the translational symmetry of the lattice [19]. The Raman active ZnO phonons and the N-related modes were analyzed with respect to the amount of nitrogen incorporated in ZnO as well as their behavior upon hydrostatic pressure applied and sample rotation. The findings reveal discrepancies for the silent B modes between the outcome of *ab initio* calculations and the nitrogen-related modes observed in experiments. In addition, their symmetry characteristics cannot be represented in a conclusive picture by silent B modes of wurtzite ZnO if the assumption is valid that the perturbation introduced by the defect N_O is large enough to manipulate the Raman activity and the symmetry character of the extended lattice modes. Thus, the assignment of the additional signals to silent B modes of wurtzite ZnO becomes disputable. Consistent with all experimental findings, the formation of clusters containing N atoms/ions, in particular, of Zn_3N_2-like clusters that are formed when the solubility limit of N on O sites is exceeded, are proposed as the origin of the additional signals. Further experiments are required to clarify the existence of

such clusters, identify their shape, and, if the hypothesis is valid, their influence on other ZnO properties. In addition, theoretical modeling may give insight into whether Zn_3N_2-like clusters are energetically favored and how their orientation depends on the growth conditions.

The outcomes for the lattice vibration of E_2^{high} symmetry character in N doped ZnO upon rotation could not adequately be explained by its symmetry type. To ascertain the reason further, experiments are required in which both E_2 symmetry type modes are analyzed simultaneously.

Raman spectra of crystalline Cu_2O are often dominated by Raman-forbidden lattice vibrations rather than by the single Raman-active phonon predicted by group theory for the ideal crystal structure [4]. A group theoretical analysis of the symmetry reduction due to the presence of defects demonstrated that the copper split vacancy, a point defect particular to Cu_2O, introduces Raman activity for all phonons that are Raman forbidden. The symmetry characteristics of the lattice vibrations observed in Raman spectra corroborate this assumption. These findings are surprising: Raman spectra of most crystalline materials are consistent with the laws of conservation as well as the Raman activity and the symmetry selection-rules established for an ideal crystal structure, despite the considerable amount of defects present in crystalline materials as shown for pure ZnO. The special role of the split vacancy may be due to the strong perturbation introduced by it compared to simple point defects, which is indicated by DFT calculations for supercell defect structures. However, resonant Raman scattering mechanisms cannot entirely be ruled out to alter the Raman activity and symmetry selection-rules such that all phonons become Raman active, since the analyzed Raman spectra are dependent on the excitation frequency. Further insight could be achieved by performing Raman experiments of high quality Cu_2O crystals upon sample or plane of polarization rotation at low temperatures, especially polarization-dependent off-resonance Raman scattering experiments.

The theoretical discussions and experimental investigations within the present thesis demonstrate that Raman scattering is influenced in many different ways by defects in the material under study. A thoughtful analysis of the corresponding Raman spectra may give insight into occurring defects and their properties. In particular, Raman experiments upon sample or plane of polarization rotation of extended lattice vibrations and defect-related modes may reveal their symmetry character and accordingly information about their origin. A number of general questions remain that have to be addressed by experiment and theory, such as: When are the deviations of the ideal crystal structure induced by defects large enough to be detectable in experimental Raman spectra? Will there be a discrete or continuous transition between the two regimes? Which effect will occur under which conditions, e.g., will local vibrations due to impurities or Raman-forbidden phonons due to symmetry reduction induced by defects be present in experimental Raman spectra? How are the host phonons of the unperturbed system influenced by defects? All these questions are topics for further research.

Bibliography

[1] R. L. William Hayes, *Scattering of light by crystals*, John Wiley & Sons (1978).

[2] H. Kuzmany, *Solid-State Spectroscopy An Introduction*, 2nd edn., Springer-Verlag, Berlin (2009).

[3] R. Shuker and R. W. Gammon, "Raman-Scattering Selection-Rule Breaking and the Density of States in Amorphous Materials", Phys. Rev. Lett. **25** (4), 222–225 (1970).

[4] J. Reydellet, M. Balkanski, and D. Trivich, "Light Scattering and Infrared Absorption in Cuprous Oxide", Phys. Status Solidi B **52** (1), 175–185 (1972).

[5] A. S. Barker and A. J. Sievers, "Optical studies of the vibrational properties of disordered solids", Rev. Mod. Phys. **47** (S2), S1–S179 (1975).

[6] F. Kröger, *The Chemistry of Imperfect Crystals*, North-Holland Publishing Company, Amsterdam (1964).

[7] Ü. Özgür, Y. I. Alivov, C. Liu, A. Teke, M. A. Reshchikov, *et al.*, "A comprehensive review of ZnO materials and devices", J. Appl. Phys. **98** (4), 041301 (2005).

[8] M. D. McCluskey and S. J. Jokela, "Defects in ZnO", J. Appl. Phys. **106** (7), 071101 (2009).

[9] C. F. Klinshirn, B. K. Meyer, A. Waag, A. Hoffmann, and J. Geurts, *Zinc Oxide From Fundamental Properties Towards Noval Applications*, Springer Series in Materials Science 120, Springer-Verlag, Berlin (2010).

[10] C. W. Litton, D. C. Reynolds, and T. C. Collins (editors), *Zinc Oxide Materials for Electronic and Opoelectronic Device Applications*, Wiley Series in Materials for Electronic & Optoelectronic Applications, John Wiley & Sons (2011).

[11] A. Kaschner, U. Haboeck, Martin Strassburg, Matthias Strassburg, G. Kaczmarczyk, *et al.*, "Nitrogen-related local vibrational modes in ZnO:N", Appl. Phys. Lett. **80** (11), 1909–1911 (2002).

[12] X. Wang, S. Yang, J. Wang, M. Li, X. Jiang, *et al.*, "Nitrogen doped ZnO film grown by the plasma-assisted metal-organic chemical vapor deposition", J. Cryst. Grwoth **226** (1), 123–129 (2001).

[13] C. Bundesmann, N. Ashkenov, M. Schubert, D. Spemann, T. Butz, *et al.*, "Raman scattering in ZnO thin films doped with Fe, Sb, Al, Ga, and Li", Appl. Phys. Lett **83** (10), 1974–1976 (2003).

[14] F. Reuss, C. Kirchner, T. Gruber, R. Kling, S. Maschek, *et al.*, "Optical investigations on the annealing behavior of gallium- and nitrogen-implanted ZnO", J. Appl. Phys. **95** (7), 3385–3390 (2004).

[15] J. B. Wang, H. M. Zhong, Z. F. Li, and W. Lu, "Raman study of N^+-implanted ZnO", Appl. Phys. Lett. **88** (10), 101913 (2006).

[16] J. Yu, H. Xing, Q. Zhao, H. Mao, Y. Shen, *et al.*, "The origin of additional modes in Raman spectra of N^+-implanted ZnO", Solid State Commun. **138** (10-11), 502–504 (2006).

[17] L. Artús, R. Cuscó, E. Alarcón-Lladó, G. González-Díaz, I. Mártil, *et al.*, "Isotopic study of the nitrogen-related modes in N^+-implanted ZnO", Appl. Phys. Lett. **90** (18), 181911 (2007).

[18] F. Friedrich, M. A. Gluba, and N. H. Nickel, "Identification of nitrogen and zinc related vibrational modes in ZnO", Appl. Phys. Lett. **95** (14), 141903 (2009).

[19] F. J. Manjón, B. Marí, J. Serrano, and A. H. Romero, "Silent Raman modes in zinc oxide and related nitrides", J. Appl. Phys. **97** (5), 053516 (2005).

[20] S. T. Pantelides, "The electronic structure of impurities and other point defects in semiconductors", Rev. Mod. Phys. **50**, 797–858 (1978).

[21] H. J. Queisser and E. E. Haller, "Defects in Semiconductors: Some Fatal, Some Vital", Science **281** (5379), 945–950 (1998).

[22] F. Tuomisto and I. Makkonen, "Defect identification in semiconductors with positron annihilation: Experiment and theory", Rev. Mod. Phys. **85**, 1583–1631 (2013).

[23] C. Freysoldt, B. Grabowski, T. Hickel, J. Neugebauer, G. Kresse, *et al.*, "First-principles calculations for point defects in solids", Rev. Mod. Phys. **86**, 253–305 (2014).

[24] P. Y. Yu and M. Cardona, *Fundamentals of Semiconductors Physics and Materials Properties*, 4th edn., Springer-Verlag, Berlin (2010).

[25] M. Stavola (editor), *Identification of Defects in Semiconductors*, Semiconductors and Semimetals vol. 51A, Academic Press, San Diego (1998).

[26] M. Stavola (editor), *Identification of Defects in Semiconductors*, Semiconductors and Semimetals vol. 51B, Academic Press, San Diego (1999).

[27] C. Kittel, *Einführung in die Festkörperphysik*, 15th edn., Oldenbourg Verlag, München (2013).

[28] M. S. Dresselhaus, G. Dresselhaus, and A. Jorio, *Group theory: application to the physics of condensed matter*, Springer-Verlag, Berlin (2008).

[29] M. D. McCluskey, "Local vibrational modes of impurities in semiconductors", J. Appl. Phys. **87** (8), 3593–3617 (2000).

[30] L. Svob, C. Thiandoume, A. Lusson, M. Bouanani, Y. Marfaing, *et al.*, "p-type doping with N and Li acceptors of ZnS grown by metalorganic vapor phase epitaxy", Appl. Phys. Lett. **76** (13), 1695–1697 (2000).

[31] J. Qiu, J. M. DePuydt, H. Cheng, and M. A. Haase, "Heavily doped p-ZnSe:N grown by molecular beam epitaxy", Appl. Phys. Lett. **59** (23), 2992–2994 (1991).

[32] A. Kobayashi, O. F. Sankey, and J. D. Dow, "Deep energy levels of defects in the wurtzite semiconductors AIN, CdS, CdSe, ZnS, and ZnO", Phys. Rev. B **28** (2), 946–956 (1983).

[33] B. K. Meyer, A. Polity, D. Reppin, M. Becker, P. Hering, *et al.*, "Binary copper oxide semiconductors: From materials towards devices", Phys. Status Solidi (b) **249** (8), 1487–1509 (2012).

[34] H. Raebiger, S. Lany, and A. Zunger, "Origins of the p-type nature and cation deficiency in Cu_2O and related materials", Phys. Rev. B **76** (4), 045209 (2007).

[35] B. K. Meyer, A. Polity, D. Reppin, M. Becker, P. Hering, *et al.*, "Chapter Six - The Physics of Copper Oxide (Cu_2O)", in B. G. Svensson, S. J. Pearton, and C. Jagadish (editors), "Oxide Semiconductors", Semiconductors and Semimetals vol. 88, pp. 201–226, Academic Press, Burlington (2013).

[36] T. Sander, S. Eisermann, B. K. Meyer, and P. J. Klar, "Raman tensor elements of wurtzite ZnO", Phys. Rev. B **85** (16), 165208 (2012).

[37] T. Sander, C. T. Reindl, and P. J. Klar, "Breaking of Raman selection rules in Cu_2O by intrinsic point defects", MRS Proceedings **1633**, 81–86 (2014).

[38] T. Sander, C. T. Reindl, M. Giar, B. Eifert, M. Heinemann, *et al.*, "Correlation of intrinsic point defects and the Raman modes of cuprous oxide", Phys. Rev. B **90**, 045203 (2014).

[39] D. A. Long, *Raman Spectroscopy*, McGraw-Hill International Book Company, New York (1977).

[40] W. Hayes and R. Loudon, *Scattering of light by crystals*, John Wiley & Sons, New York (1978).

[41] E. B. Wilson, J. C. Decius, and P. C. Cross, *Molecular vibrations: The Theory of Infrared and Raman Vibrational Spectra*, Dover Publications, New York (1980), unabrigded and corrected republication.

[42] M. Cardona, G. Güntherodt, R. K. Chang, M. B. Long, and H. Vogt, *Light Scattering in Solids II Basic Concepts and Instrumentation*, Topics in Applied Physics vol. 50, Springer-Verlag, Berlin (1982).

[43] F. A. Cotton, *Chemical Applications of Group Theory*, A Wiley-Interscience publication, 3rd edn., John Wiley & Sons, New York (1990).

[44] A. Authier (editor), *International Tables for Cristallography Volume D: Physical Properties of Crystals*, Kluwer Academic Publishers, Dordrecht (2003).

[45] R. S. Mulliken, "Report on Notation for the Spectra of Polyatomic Molecules", J. Chem. Phys. **23** (11), 1997–2011 (1955).

[46] R. S. Mulliken, "Erratum : Report on Notation for the Spectra of Polyatomic Molecules", J. Chem. Phys. **24**, 1118 (1956).

[47] D. L. Rousseau, R. P. Bauman, and S. P. S. Porto, "Normal mode determination in crystals", J. Raman Spectrosc. **10** (1), 253–290 (1981).

[48] R. S. Krishnan and R. K. Shankar, "Raman effect: History of the discovery", J. Raman Spectrosc. **10** (1), 1–8 (1981).

[49] C. V. Raman, "A new radiation", Indian Assoc. Cultiv. Sci. **2**, 387–398 (1928).

[50] C. V. Raman and K. S. Krishnan, "A New Type of Secondary Radiation", Nature London **121**, 501–502 (1928).

[51] C. V. Raman, "A Change of Wave-length in Light Scattering", Nature **121**, 619 (1928).

[52] C. V. Raman and K. S. Krishnan, "The Optical Analogue of the Compton Effect", Nature **121**, 711 (1928).

[53] Nobel Prize in Physics (1930), http://www.nobelprize.org/nobel_prizes/physics/laureates/1930/ (12.06.2015).

[54] A. Smekal, "Zur Quantentheorie der Dispersion", Naturwissenschaften **11** (43), 873–875 (1923).

[55] G. Placzek, *Rayleigh-Streuung und Raman-Effekt*, Akademische Verlagsgesellschaft, Leipzig (1934).

[56] R. Loudon, "The Raman effect in crystals", Adv. Phys. **13** (52), 423–482 (1964).

[57] B. K. Vainshtein, V. M. Fridkin, and V. L. Indenbom, *Structure of Crystals*, Modern Crystallography 2, 3rd edn., Springer-Verlag, Berlin (2000).

[58] T. C. Damen, S. P. S. Porto, and B. Tell, "Raman Effect in Zinc Oxide", Phys. Rev. **142** (2), 570–574 (1966).

[59] C. A. Arguello, D. L. Rousseau, and S. P. S. Porto, "First-Order Raman Effect in Wurtzite-Type Crystals", Phys. Rev. **181** (3), 1351–1363 (1969).

[60] T. Hahn (editor), *International Tables for Cristallography Vol. A Space-Group Symmetry*, 5th edn., Springer-Verlag, Dordrecht (2005).

[61] G. F. Koster, J. O. Dimmock, R. G. Wheeler, and H. Statz, *Properties of the thirty-two point groups*, The Massachusetts Institute of Technology Press, Cambridge, Mass. (1963).

[62] M. Cardona, A. Pinczuk, E. Burstein, R. M. Martin, L. M. Falicov, *et al.*, *Light Scattering in Solids*, Topics in Applied Physics vol. 8, Springer-Verlag, Berlin (1975).

[63] J. E. Smith, M. H. Brodsky, B. L. Crowder, M. I. Nathan, and A. Pinczuk, "Raman Spectra of Amorphous Si and Related Tetrahedrally Bonded Semiconductors", Phys. Rev. Lett. **26**, 642–646 (1971).

[64] H. Richter, Z. Wang, and L. Ley, "The one phonon Raman spectrum in microcrystalline silicon", Solid State Commun. **39** (5), 625–629 (1981).

[65] I. Campbell and P. Fauchet, "The effects of microcrystal size and shape on the one phonon Raman spectra of crystalline semiconductors", Solid State Commun. **58** (10), 739–741 (1986).

[66] H. K. Mao, P. M. Bell, J. W. Shaner, and D. J. Steinberg, "Specific volume measurements of Cu, Mo, Pd, and Ag and calibration of the ruby R_1 fluorescence pressure gauge from 0.06 to 1 Mbar", J. Appl. Phys. **49** (6), 3276–3283 (1978).

[67] A. D. Chijioke, W. J. Nellis, A. Soldatov, and I. F. Silvera, "The ruby pressure standard to 150 GPa", J. Appl. Phys. **98** (11), 114905 (2005).

[68] CrysTec GmbH, Berlin, Germany, http://www.crystec.de/crystec-e.html (06.06.2015).

[69] Tokyo Denpa Co., Ltd. (TEW), Tokyo, Japan, withdrawal from ZnO crystal production in 2013, http://www.tew.co.jp/en/ (06.06.2015).

[70] W. M. Haynes (editor), *CRC Handbook of Chemistry and Physics*, 94th edn., CRC Press, Boca Raton (2013).

[71] V. Srikant and D. R. Clarke, "On the optical band gap of zinc oxide", J. Appl. Phys. **83** (10), 5447–5451 (1998).

[72] J. Serrano, F. J. Manjón, A. H. Romero, A. Ivanov, M. Cardona, *et al.*, "Phonon dispersion relations of zinc oxide: Inelastic neutron scattering and *ab initio* calculations", Phys. Rev. B **81** (17), 174304 (2010).

[73] J. Serrano, A. H. Romero, F. J. Manjón, R. Lauck, M. Cardona, *et al.*, "Pressure dependence of the lattice dynamics of ZnO: An ab initio approach", Phys. Rev. B **69** (9), 094306 (2004).

[74] J. Serrano, F. J. Manjón, A. H. Romero, A. Ivanov, R. Lauck, *et al.*, "The phonon dispersion of wurtzite-ZnO revisited", Phys. Status Solidi B **244** (5), 1478–1482 (2007).

[75] J. Wróbel, K. J. Kurzydłowski, K. Hummer, G. Kresse, and J. Piechota, "Calculations of ZnO properties using the Heyd-Scuseria-Ernzerhof screened hybrid density functional", Phys. Rev. B **80**, 155124 (2009).

[76] R. H. Callender, S. S. Sussman, M. Selders, and R. K. Chang, "Dispersion of Raman Cross Section in CdS and ZnO over a Wide Energy Range", Phys. Rev. B **7** (8), 3788–3798 (1973).

[77] R. Cuscó, E. Alarcón-Lladó, J. Ibáñez, L. Artús, J. Jiménez, *et al.*, "Temperature dependence of Raman scattering in ZnO", Phys. Rev. B **75**, 165202 (2007).

[78] H. Siegle, G. Kaczmarczyk, L. Filippidis, A. P. Litvinchuk, A. Hoffmann, *et al.*, "Zone-boundary phonons in hexagonal and cubic GaN", Phys. Rev. B **55** (11), 7000–7004 (1997).

[79] J. Serrano, F. J. Manjón, A. H. Romero, F. Widulle, R. Lauck, *et al.*, "Dispersive Phonon Linewidths: The E_2 Phonons of ZnO", Phys. Rev. Lett. **90** (5), 055510 (2003).

[80] N. Ashkenov, B. N. Mbenkum, C. Bundesmann, V. Riede, M. Lorenz, *et al.*, "Infrared dielectric functions and phonon modes of high-quality ZnO films", J. Appl. Phys. **93** (1), 126–133 (2003).

[81] T. Strach, J. Brunen, B. Lederle, J. Zegenhagen, and M. Cardona, "Determination of the phase difference between the Raman tensor elements of the A_{1g}-like phonons in $SmBa_2Cu_3O_{7-\delta}$", Phys. Rev. B **57** (2), 1292–1297 (1998).

[82] N. H. Nickel and K. Fleischer, "Hydrogen Local Vibrational Modes in Zinc Oxide", Phys. Rev. Lett. **90**, 197402 (2003).

[83] K. Minegishi, Y. Koiwai, Y. Kikuchi, K. Yano, M. Kasuga, *et al.*, "Growth of p-type Zinc Oxide Films by Chemical Vapor Deposition", Jpn. J. Appl. Phys. 2 **36** (11A), L1453–L1455 (1997).

[84] J. E. Stehr, D. M. Hofmann, and B. K. Meyer, "Electron paramagnetic resonance and photo-electron paramagnetic resonance investigation on the recharging of the substitutional nitrogen acceptor in ZnO", J. Appl. Phys. **112** (10), 103511 (2012).

[85] U. Haboeck, A. Hoffmann, C. Thomsen, A. Zeuner, and B. K. Meyer, "High-energy vibrational modes in nitrogen-doped ZnO", Phys. Status Solidi B **242** (3), R21–R23 (2005).

[86] S. Eisermann, A. Kronenberger, M. Dietrich, S. Petznick, A. Laufer, *et al.*, "Hydrogen and nitrogen incorporation in ZnO thin films grown by radio-frequency (RF) sputtering", Thin Solid Films **518** (4), 1099–1102 (2009).

[87] A. Zeuner, H. Alves, D. M. Hofmann, B. K. Meyer, A. Hoffmann, *et al.*, "Optical Properties of the Nitrogen Acceptor in Epitaxial ZnO", Phys. Status Solidi B **234** (3), R7–R9 (2002).

[88] D. Taïnoff, M. Al-Khalfioui, C. Deparis, B. Vinter, M. Teisseire, *et al.*, "Residual and nitrogen doping of homoepitaxial nonpolar m-plane ZnO films grown by molecular beam epitaxy", Appl. Phys. Lett. **98** (13), 131915 (2011).

[89] Alfa Aesar GmbH & Co KG, Karlsruhe, Germany, http://www.alfa.com/ de/catalog/88212 (06.06.2015).

[90] T. Englert, G. Abstreiter, and J. Pontcharra, "Determination of existing stress in silicon films on sapphire substrate using Raman spectroscopy", Solid State Electron. **23** (1), 31–33 (1980).

[91] C. Kisielowski, J. Krüger, S. Ruvimov, T. Suski, J. W. Ager, *et al.*, "Strain-related phenomena in GaN thin films", Phys. Rev. B **54**, 17745–17753 (1996).

[92] M. Schumm, *ZnO-based semiconductors studied by Raman spectroscopy: semimagnetic alloying, doping, and nanostructures*, Ph.D. thesis, Julius-Maximilians-Universität Würzburg (2008).

[93] G. Du, Y. Ma, Y. Zhang, and T. Yang, "Preparation of intrinsic and N-doped p-type ZnO thin films by metalorganic vapor phase epitaxy", Appl. Phys. Lett. **87** (21), 213103 (2005).

[94] F. Friedrich and N. H. Nickel, "Resonant Raman scattering in hydrogen and nitrogen doped ZnO", Appl. Phys. Lett. **91** (11), 111903 (2007).

[95] Prof. Dr. C. Heiliger, Justus-Liebig-Universität Giessen, private communication (2014).

[96] S. Limpijumnong, X. Li, S.-H. Wei, and S. B. Zhang, "Substitutional diatomic molecules NO, NC, CO, N_2, and O_2: Their vibrational frequencies and effects on p doping of ZnO", Appl. Phys. Lett. **86** (21), 211910 (2005).

[97] N. H. Nickel, F. Friedrich, J. F. Rommeluere, and P. Galtier, "Vibrational spectroscopy of undoped and nitrogen-doped ZnO grown by metalorganic chemical vapor deposition", Appl. Phys. Lett. **87** (21), 211905 (2005).

[98] S. J. Jokela and M. D. McCluskey, "Unambiguous identification of nitrogen-hydrogen complexes in ZnO", Phys. Rev. B **76** (19), 193201 (2007).

[99] S. J. Jokela and M. D. McCluskey, "Structure and stability of N–H complexes in single-crystal ZnO", J. Appl. Phys. **107** (11), 113536 (2010).

[100] M. Schumm, M. Koerdel, S. Müller, C. Ronning, E. Dynowska, *et al.*, "Secondary phase segregation in heavily transition metal implanted ZnO", J. Appl. Phys. **105** (8), 083525 (2009).

[101] H. F. Liu and S. J. Chua, "Doping behavior of phosphorus in ZnO thin films: Effects of doping concentration and postgrowth thermal annealing", Appl. Phys. Lett. **96** (9), 091902 (2010).

[102] H. Harima, "Raman studies on spintronics materials based on wide bandgap semiconductors", J. Phys. Condens. Matter **16** (48), S5653–S5660 (2004).

[103] K. Samanta, P. Bhattacharya, and R. S. Katiyar, "Raman scattering studies of p-type Sb-doped ZnO thin films", J. Appl. Phys. **108** (11), 113501 (2010).

[104] M. A. Gluba, N. H. Nickel, and N. Karpensky, "Interstitial zinc clusters in zinc oxide", Phys. Rev. B **88**, 245201 (2013).

[105] J. S. Reparaz, L. R. Muniz, M. R. Wagner, A. R. Goñi, M. I. Alonso, *et al.*, "Reduction of the transverse effective charge of optical phonons in ZnO under pressure", Appl. Phys. Lett. **96** (23), 231906 (2010).

[106] J. F. Nye, *Physical Properties of Crystals*, Oxford University Press, London (1957).

[107] S. J. Jokela and M. D. McCluskey, "Structure and stability of $O-H$ donors in ZnO from high-pressure and infrared spectroscopy", Phys. Rev. B **72**, 113201 (2005).

[108] J. Furthmüller, F. Hachenberg, A. Schleife, D. Rogers, F. H. Teherani, *et al.*, "Clustering of N impurities in ZnO", Appl. Phys. Lett. **100** (2), 022107 (2012).

[109] Prof. Dr. J. Janek, Justus-Liebig-Universität Giessen, private communication (2014).

[110] R. Juza, A. Neuber, and H. Hahn, "Zur Kenntnis des Zinknitrides Metallamide und Metallnitride. IV. Mitteilung", Z. Anorg. Allg. Chem. **239** (3), 273–281 (1938).

[111] R. Juza and H. Hahn, "Über die Kristallstrukturen von Zn_3N_2, Cd_3N_2 und Ge_3N_4. Metallamide und Metallnitride. IX. Mitteilung", Z. Anorg. Allg. Chem. **244** (2), 125–132 (1940).

[112] D. E. Partin, D. J. Williams, and M. O'Keeffe, "The Crystal Structures of Mg_3N_2 and Zn_3N_2", J. Solid State Chem. **132** (1), 56–59 (1997).

[113] G. Paniconi, Z. Stoeva, R. I. Smith, P. C. Dippo, B. L. Gallagher, *et al.*, "Synthesis, stoichiometry and thermal stability of Zn_3N_2 powders prepared by ammonolysis reactions", J. Solid State Chem. **181** (1), 158–165 (2008).

[114] N. Jiang, J. L. Roehl, S. V. Khare, D. G. Georgiev, and A. H. Jayatissa, "An ab initio computational study of pure Zn_3N_2 and its native point defects and dopants Cu, Ag and Au", Thin Solid Films **564**, 331–338 (2014).

[115] E. Kroumova, M. I. Aroyo, J. M. Perez-Mato, A. Kirov, C. Capillas, *et al.*, "Bilbao Crystallographic Server : Useful Databases and Tools for Phase-Transition Studies", Phase Transitions **76** (1-2), 155–170 (2003).

[116] Z.-X. Zhang, X.-J. Pan, L.-X. Liu, Z.-W. Ma, H.-T. Zhao, *et al.*, "Green photoluminescence from Zn_3N_2:Tb films prepared by magnetron sputtering", J. Appl. Phys. **105** (1), 016101 (2009).

[117] G. Z. Xing, D. D. Wang, B. Yao, L. F. N. Ah Qune, T. Yang, *et al.*, "Structural and electrical characteristics of high quality (100) orientated-Zn_3N_2 thin films grown by radio-frequency magnetron sputtering", J. Appl. Phys. **108** (8), 083710 (2010).

[118] N. Jiang, D. G. Georgiev, T. Wen, and A. H. Jayatissa, "Reactive radio frequency sputtering deposition and characterization of zinc nitride and oxynitride thin films", Thin Solid Films **520** (6), 1698–1704 (2012).

[119] J. Khoshman, N. Peica, C. Thomsen, J. Maultzsch, B. Bastek, *et al.*, "Growth and surface characterization of magnetron sputtered zinc nitride thin films", Thin Solid Films **520** (24), 7230–7235 (2012).

[120] P.-C. Wei, S.-C. Tong, C.-M. Tseng, C.-C. Chang, C.-H. Hsu, *et al.*, "Structural, compositional, and photoluminescence characterization of thermal chemical vapor deposition-grown Zn_3N_2 microtips", J. Appl. Phys. **116** (14), 143507 (2014).

[121] A. Zeuner, H. Alves, J. Sann, W. Kriegseis, C. Neumann, *et al.*, "Nitrogen doping in bulk and epitaxial ZnO", Phys. Status Solidi C **1** (4), 731–734 (2004).

[122] L. Wang and N. C. Giles, "Determination of the ionization energy of nitrogen acceptors in zinc oxide using photoluminescence spectroscopy", Appl. Phys. Lett. **84** (16), 3049–3051 (2004).

[123] N. Hanèche, A. Lusson, C. Sartel, A. Marzouki, V. Sallet, *et al.*, "Optical characterization of nitrogen- and antimony-doped ZnO thin layers grown by MOVPE", Phys. Status Solidi B **247** (7), 1671–1674 (2010).

[124] S. Lautenschläger, S. Eisermann, G. Haas, E. A. Zolnowski, M. N. Hofmann, *et al.*, "Optical signatures of nitrogen acceptors in ZnO", Phys. Rev. B **85** (23), 235204 (2012).

[125] S. Limpijumnong, L. Gordon, M. Miao, A. Janotti, and C. G. V. de Walle, "Alternative sources of p-type conduction in acceptor-doped ZnO", Appl. Phys. Lett. **97** (7), 072112 (2010).

[126] J. Pierson, A. Thobor-Keck, and A. Billard, "Cuprite, paramelaconite and tenorite films deposited by reactive magnetron sputtering", Appl. Surf. Sci. **210** (3-4), 359–367 (2003).

[127] J. Neumann, T. Zhong, and Y. Chang, "The Cu-O (Copper-Oxygen) system", Bulletin of Alloy Phase Diagrams **5** (2), 136–140 (1984).

[128] L. Schramm, G. Behr, W. Löser, and K. Wetzig, "Thermodynamic reassessment of the Cu-O phase diagram", J. Phase Equilib. Diff. **26** (6), 605–612 (2005).

[129] M. Heinemann, B. Eifert, and C. Heiliger, "Band structure and phase stability of the copper oxides Cu_2O, CuO, and Cu_4O_3", Phys. Rev. B **87**, 115111 (2013).

[130] D. E. Mencer, M. A. Hossain, R. Schennach, T. Grady, H. McWhinney, *et al.*, "On the surface analysis of copper oxides: the difficulty in detecting Cu_3O_2", Vacuum **77** (1), 27–35 (2004).

[131] D. L. Cocke, R. Schennach, M. A. Hossain, D. E. Mencer, H. McWhinney, *et al.*, "The low-temperature thermal oxidation of copper, Cu_3O_2, and its influence on past and future studies", Vacuum **79** (1-2), 71–83 (2005).

[132] S. Åsbrink and L.-J. Norrby, "A refinement of the crystal structure of copper(II) oxide with a discussion of some exceptional e.s.d.'s", Acta Crystallogr. B **26** (1), 8–15 (1970).

[133] C. Frondel, "Paramelaconite: A tetragonal oxide of copper", Am. Mineal. **26**, 657–72 (1941).

[134] M. O'Keeffe and J.-O. Bovin, "The crystal structure of paramelaconite, Cu_4O_3", Am. Mineal. **63**, 180–185 (1978).

[135] R. J. Elliott, "Symmetry of Excitons in Cu_2O", Phys. Rev. **124** (2), 340–345 (1961).

[136] K. Huang, "The long wave modes of the Cu_2O lattice", Z. Phys. **171** (1), 213–225 (1963).

[137] M. Balkanski, M. A. Nusimovici, and J. Reydellet, "First order Raman spectrum of Cu_2O", Solid State Commun. **7** (11), 815–818 (1969).

[138] C. Carabatos, "Lattice Vibrations of Cu_2O at the Long Wave Limit", Phys. Status Solidi B **37** (2), 773–779 (1970).

[139] C. Carabatos and B. Prevot, "Rigid ion model lattice dynamics of cuprite (Cu_2O)", Phys. Status Solidi B **44** (2), 701–712 (1971).

[140] E. Gross, "Optical spectrum of excitons in the crystal lattice", Il Nuovo Cimento Series 10 **3** (4), 672–701 (1956).

[141] V. T. Agekyan, "Spectroscopic properties of semiconductor crystals with direct forbidden energy gap", Phys. Status Solidi A **43** (1), 11–42 (1977).

[142] C. Uihlein, D. Fröhlich, and R. Kenklies, "Investigation of exciton fine structure in Cu_2O", Phys. Rev. B **23** (6), 2731–2740 (1981).

[143] R. J. Elliott, "Intensity of Optical Absorption by Excitons", Phys. Rev. **108**, 1384–1389 (1957).

[144] Cuprite, http://www.mindat.org/min-1172.html (18.03.2015).

[145] A. F. Wright and J. S. Nelson, "Theory of the copper vacancy in cuprous oxide", J. Appl. Phys. **92** (10), 5849–5851 (2002).

[146] M. Nolan and S. D. Elliott, "The p-type conduction mechanism in Cu_2O: a first principles study", Phys. Chem. Chem. Phys. **8**, 5350–5358 (2006).

[147] A. Soon, X.-Y. Cui, B. Delley, S.-H. Wei, and C. Stampfl, "Native defect-induced multifarious magnetism in nonstoichiometric cuprous oxide: First-principles study of bulk and surface properties of $Cu_{2-\delta}O$", Phys. Rev. B **79** (3), 035205 (2009).

[148] D. O. Scanlon, B. J. Morgan, G. W. Watson, and A. Walsh, "Acceptor Levels in p-Type Cu_2O: Rationalizing Theory and Experiment", Phys. Rev. Lett. **103** (9), 096405 (2009).

[149] D. O. Scanlon, B. J. Morgan, and G. W. Watson, "Modeling the polaronic nature of p-type defects in Cu_2O: The failure of GGA and GGA+U", J. Chem. Phys. **131** (12), 124703 (2009).

[150] D. O. Scanlon and G. W. Watson, "Undoped n-Type Cu_2O: Fact or Fiction?", J. Phys. Chem. Lett. **1** (17), 2582–2585 (2010).

[151] T. Suzuki, "X-Ray Study on the Binding Properties of Cu_2O and Ag_2O Crystals", J. Phys. Soc. Jpn. **15** (11), 2018–2024 (1960).

[152] K. Reimann and K. Syassen, "Raman scattering and photoluminescence in Cu_2O under hydrostatic pressure", Phys. Rev. B **39** (15), 11113 (1989).

[153] L. Debbichi, M. C. Marco de Lucas, J. F. Pierson, and P. Krüger, "Vibrational Properties of CuO and Cu_4O_3 from First-Principles Calculations, and Raman and Infrared Spectroscopy", J. Phys. Chem. C **116** (18), 10232–10237 (2012).

[154] J. Chrzanowski and J. C. Irwin, "Raman scattering from cupric oxide", Solid State Commun. **70** (1), 11–14 (1989).

[155] H. F. Goldstein, D. Kim, P. Y. Yu, L. C. Bourne, J.-P. Chaminade, *et al.*, "Raman study of CuO single crystals", Phys. Rev. B **41** (10), 7192–7194 (1990).

[156] M. Giar and Prof. Dr. C. Heiliger, Justus-Liebig-Universität Giessen, private communication (2015).

[157] A. Compaan and H. Z. Cummins, "Raman Scattering, Luminescence, and Exciton-Phonon Coupling in Cu_2O", Phys. Rev. B **6** (12), 4753–4757 (1972).

[158] Y. Petroff, P. Y. Yu, and Y. R. Shen, "Luminescence of Cu_2O-Excitonic Molecules, or Not?", Phys. Rev. Lett. **29** (23), 1558–1562 (1972).

[159] P. Dawson, M. M. Hargreave, and G. R. Wilkinson, "The dielectric and lattice vibrational spectrum of cuprous oxide", J. Phys. Chem. Solids **34** (12), 2201–2208 (1973).

[160] P. F. Williams and S. P. S. Porto, "Symmetry-Forbidden Resonant Raman Scattering in Cu_2O", Phys. Rev. B **8** (4), 1782–1785 (1973).

[161] A. Compaan, "Surface damage effects on allowed and forbidden phonon Raman scattering in cuprous oxide", Solid State Commun. **16** (3), 293–296 (1975).

[162] D. Powell, A. Compaan, J. R. Macdonald, and R. A. Forman, "Raman-scattering study of ion-implantation-produced damage in Cu_2O", Phys. Rev. B **12** (1), 20–25 (1975).

[163] A. Compaan and H. Z. Cummins, "Resonant Quadrupole-Dipole Raman Scattering at the $1S$ Yellow Exciton in Cu_2O", Phys. Rev. Lett. **31** (1), 41–44 (1973).

[164] J. L. Birman, "Theory of multipole-dipole resonance Raman scattering by phonons", Solid State Commun. **13** (8), 1189–1193 (1973).

[165] J. L. Birman, "Scattering tensors for "forbidden" resonance Raman scattering in cubic crystals", Phys. Rev. B **9**, 4518–4528 (1974).

[166] A. Z. Genack, H. Z. Cummins, M. A. Washington, and A. Compaan, "Quadrupole-dipole Raman scattering at the $1S$ yellow exciton in Cu_2O", Phys. Rev. B **12**, 2478–2487 (1975).

[167] P. Y. Yu, Y. R. Shen, Y. Petroff, and L. M. Falicov, "Resonance Raman Scattering at the Forbidden Yellow Exciton in Cu_2O", Phys. Rev. Lett. **30** (7), 283–286 (1973).

[168] P. Yu, Y. Shen, and Y. Petroff, "Resonance Raman scattering in Cu_2O at the blue and indigo excitons", Solid State Commun. **12** (10), 973–975 (1973).

[169] P. Y. Yu and Y. R. Shen, "Multiple Resonance Effects on Raman Scattering at the Yellow-Exciton Series of Cu_2O", Phys. Rev. Lett. **32** (7), 373–376 (1974).

[170] P. Y. Yu and Y. R. Shen, "Study of Dispersive Raman Modes in Cu_2O by Resonant Raman Scattering", Phys. Rev. Lett. **32**, 939–942 (1974).

[171] C.-H. Wu and J. L. Birman, "Theory of resonant Raman enhancement of a forbidden phonon in Cu_2O", Solid State Commun. **14** (6), 465–467 (1974).

[172] M. A. Washington, A. Z. Genack, H. Z. Cummins, R. H. Bruce, A. Compaan, *et al.*, "Spectroscopy of excited yellow exciton states in Cu_2O by forbidden resonant Raman scattering", Phys. Rev. B **15**, 2145–2153 (1977).

[173] P. Y. Yu and Y. R. Shen, "Resonance Raman studies in Cu_2O. II. The yellow and green excitonic series", Phys. Rev. B **17**, 4017–4030 (1978).

[174] J. Weiner and P. Yu, "Time-resolved hot luminescence and resonant Raman scattering: Cu_2O revisited", Solid State Commun. **50** (6), 493–496 (1984).

[175] D. W. Snoke, A. J. Shields, and M. Cardona, "Phonon-absorption recombination luminescence of room-temperature excitons in Cu_2O", Phys. Rev. B **45**, 11693 (1992).

[176] F. Biccari, *Defects and Doping in Cu_2O*, Ph.D. thesis, Sapienza Università di Roma (2009).

[177] M. I. Aroyo, A. Kirov, C. Capillas, J. M. Perez-Mato, and H. Wondratschek, "Bilbao Crystallographic Server. II. Representations of crystallographic point groups and space groups", Acta Crystallogr. A **62** (2), 115–128 (2006).

[178] M. Kracht and Prof. Dr. M. Eickhoff, Justus-Liebig-Universität Giessen, private communication (2015).

[179] M. Ivanda, D. Waasmaier, A. Endriss, J. Ihringer, A. Kirfel, *et al.*, "Low-temperature anomalies of cuprite observed by Raman spectroscopy and x-ray powder diffraction", J. Raman Spectrosc. **28** (7), 487–493 (1997).

List of publications

(1) R. K. Thöt, <u>T. Sander</u>, P. J. Klar, and B. K. Meyer, "Photocurrent measurements of $Mg_xZn_{1-x}O$ epitaxial layers of different x", MRS Proceedings **1201**, 1201-H10-33 (2009).

(2) <u>T. Sander</u>, J. Teubert, P. J. Klar, A. Lindsay, and E. P. O'Reilly, "Effect of localized boron impurities on the line shape of the fundamental band gap transition in photomodulated reflectance spectra of (B,Ga,In)As", Phys. Rev. B **83** (23), 235213 (2011).

(3) <u>T. Sander</u>, S. Eisermann, B. K. Meyer, and P. J. Klar, "Raman tensor elements of wurtzite ZnO", Phys. Rev. B **85** (16), 165208 (2012).

(4) B. K. Meyer, A. Polity, D. Reppin, M. Becker, P. Hering, P. J. Klar, <u>Th. Sander</u>, C. Reindl, J. Benz, M. Eickhoff, C. Heiliger, M. Heinemann, J. Bläsing, A. Krost, S. Shokovets, C. Müller, and C. Ronning, "Binary copper oxide semiconductors: From materials towards devices", Phys. Status Solidi (b) **249** (8), 1487–1509 (2012).

(5) M. Güngerich, <u>T. Sander</u>, C. Heiliger, M. Czerner, and P. J. Klar, "Local N environment in the dilute nitrides Ga(N,P), Ga(N,As), and Ga(N,Sb)", Phys. Status Solidi B **250** (4), 755–759 (2013).

(6) <u>T. Sander</u>, M. S. Rinn, and P. J. Klar, "Photoluminescence and Raman spectroscopy of Cd(S,Se) under hydrostatic pressure", Phys. Status Solidi B **250** (4), 688–692 (2013).

(7) B. K. Meyer, A. Polity, D. Reppin, M. Becker, P. Hering, B. Kramm, P. J. Klar, <u>Th. Sander</u>, C. Reindl, C. Heiliger, M. Heinemann, C. Müller, and C. Ronning, "Chapter Six - The Physics of Copper Oxide (Cu_2O)", in B. G. Svensson, S. J. Pearton, and C. Jagadish (editors), Oxide Semiconductors, Semiconductors and Semimetals vol. 88, 201–226, Academic Press, Burlington (2013).

(8) <u>T. Sander</u>, C. T. Reindl, and P. J. Klar, "Breaking of Raman selection rules in Cu_2O by intrinsic point defects", MRS Proceedings **1633**, 81–86 (2014).

(9) <u>T. Sander</u>, C. T. Reindl, M. Giar, B. Eifert, M. Heinemann, C. Heiliger, and P. J. Klar, "Correlation of intrinsic point defects and the Raman modes of cuprous oxide", Phys. Rev. B **90** (4), 045203 (2014).

(10) H. Liu, X. Zhang, T. Zhai, <u>T. Sander</u>, L. Chen, and P.J. Klar, "Centimeter-scale-homogeneous SERS substrates with seven-order global enhancement through thermally controlled plasmonic nanostructures", Nanoscale **6**, 5099 (2014).

Acknowledgments

Selbstständigkeitserklärung

Hiermit versichere ich, die vorgelegte Dissertation selbstständig und ohne unerlaubte fremde Hilfe und nur mit den Hilfen angefertigt zu haben, die ich in der Dissertation angegeben habe. Alle Textstellen, die wörtlich oder sinngemäß aus veröffentlichten Schriften entnommen sind, und alle Angaben die auf mündlichen Auskünften beruhen, sind als solche kenntlich gemacht. Bei den von mir durchgeführten und in der Dissertation erwähnten Untersuchungen habe ich die Grundsätze guter wissenschaftlicher Praxis, wie sie in der „Satzung der Justus-Liebig-Universität zur Sicherung guter wissenschaftlicher Praxis" niedergelegt sind, eingehalten.

Ort, Datum	Thomas Sander